THE HONG KONG
POLYTECHNIC UNIVERSITY
香港理工大學
Pao Yue-kong Library
包玉剛圖書館

Copyright Undertaking

This thesis is protected by copyright, with all rights reserved.

By reading and using the thesis, the reader understands and agrees to the following terms:

1. The reader will abide by the rules and legal ordinances governing copyright regarding the use of the thesis.
2. The reader will use the thesis for the purpose of research or private study only and not for distribution or further reproduction or any other purpose.
3. The reader agrees to indemnify and hold the University harmless from and against any loss, damage, cost, liability or expenses arising from copyright infringement or unauthorized usage.

IMPORTANT

If you have reasons to believe that any materials in this thesis are deemed not suitable to be distributed in this form, or a copyright owner having difficulty with the material being included in our database, please contact lbsys@polyu.edu.hk providing details. The Library will look into your claim and consider taking remedial action upon receipt of the written requests.

Pao Yue-kong Library, The Hong Kong Polytechnic University, Hung Hom, Kowloon, Hong Kong

http://www.lib.polyu.edu.hk

FOCUSING AND MANIPULATION OF DIFFSUED LIGHT WITH WAVEFRONT ENGINEERING: TECHNIQUES AND APPLICATIONS

ZHIPENG YU

PhD

The Hong Kong Polytechnic University

2021

The Hong Kong Polytechnic University

Department of Biomedical Engineering

Focusing and Manipulation of Diffused Light with Wavefront Engineering: Techniques and Applications

ZHIPENG YU

A thesis submitted in partial fulfillment of the requirements for the degree of Doctor of Philosophy

March 2021

CERTIFICATE OF ORIGINALITY

I hereby declare that this thesis is my own work and that, to the best of my knowledge and belief, it reproduces no material previously published or written, nor material that has been accepted for the award of any other degree or diploma, except where due acknowledgement has been made in the text.

_____ (Signed)

YU ZHIPENG
_____(Name of student)

ABSTRACT

Optical techniques have been playing an important role in modern biomedicine. Their applications, however, have been constrained to superficial layers of biological tissue due to strong scattering of light in tissue. Manipulating and focusing light deep within or through biological tissue and tissue-like complex media has been sought after for long yet considered challenging. One promising strategy is via optical wavefront engineering, where scattering-induced phase distortions are time reversed or pre-compensated so that photons travelling along different optical paths interfere constructively at the targeted position. In the past decade, various implementations of wavefront engineering, such as digital optical phase conjugation (DOPC) and wavefront shaping (WFS), have been developed to tackle different situations. In this thesis, these two approaches were used for turbidity suppression, and their functionalities were explored from intuitive to abstract for biomedicine and optical computing because of the modulation flexibility.

To start with, a plain yet reliable DOPC platform with an embedded four-phase non-iterative approach was presented that can rapidly compensate for the wavefront modulator's surface curvature. The phase conjugation is implemented with a non-phase-shifting in-line holography method in the absence of an electro-optic modulator (EOM). The platform was optimized to obtain robust and superior performance as measured by optimization speed and peak-to-background ratio (PBR). Based on this platform, two essential applications of DOPC were proposed. The first one is time-

reversed magnetically controlled perturbation (TRMCP) optical focusing inside scattering media. Sharp optical focus within scattering media through time-reversing the scattered light perturbed by magnetic microspheres was obtained, where magnetically controlled optical absorbing microspheres were used as the internal guidestar for diffused light. As the object is magnetically controlled, dynamic optical focusing can be achieved in a relatively large field-of-view with a high precision. In addition, the magnetic microspheres, which can be packaged with organic membranes, can potentially serve as drug carriers. The second application is related to image transmission. It is object edge enhancement through scattering media, which is enabled by adjusting the intensity ratio between the sample and reference beams in the DOPC system. The capability is demonstrated experimentally, and furtherly the performance, as measured by the edge enhancement index (EI) and enhancement-to-noise ratio (ENR), can be controlled easily through tuning the beam ratio. EI and ENR can be reinforced by ~8.5 and ~263 folds, respectively in current system. This is the first demonstration that edges of a spatial pattern can be extracted through strong scattering medium, which can potentially broaden the comprehension and development of image transmission in a complex environment such as inside/through a biological tissue.

At last, to further broaden the scope of wavefront engineering, a diffusive optical logic (DOL) assisted by wavefront shaping to achieve reconfigurable and multifunctional logic operations on one platform was proposed: light was firstly encoded by a digital micromirror device displayed with a precalculated wavefront and then the encoded light

was diffused and decoded by a scattering medium to form logical states. As a proof of concept, five basic logic functions (AND, OR, NOT, NAND, NOR) through experiment were demonstrated, with a ground glass as the scattering medium. This is the first demonstration that a scattering medium in combination with wavefront shaping can be used as optical logic gates. As the transmission matrix of strong scattering media has huge ranks and provides enormous degrees of freedom, the concept of DOL shows great potential in optical computing with many advantages including simple fabrication process, scalability, and reconfigurability.

In summary, this thesis aims to extend the functionality and scope of wavefront engineering against optical scattering in complex media. After the general introduction of the field in Chapter 1, four topics are organized with increasing complexity of wavefront manipulation and information transmission, from optical focusing, image edge enhancement, to multifunctional diffusive optical logic gates. In the first two cases (optical focusing and image edge enhancement), wavefront modulator, as a whole, contributes to one output channel and the all output channels, respectively, where the wavefront modulation processes are overall intuitive. In the last case (diffusive optical logic gates), the wavefront modulator is divided into many control units which are tailored independently. It requires more advanced manipulation procedures, and different control units contribute to diverse output channels at the output plane. Although a lot need to be further developed, these explorations provide promising solutions to a wide range of optical applications that desire highly confined and intense

optical delivery in deep biological tissue and advanced optical computation in a complex environment

PUBLICATIONS ARISING FROM THE THESIS

Peer-reviewed Articles

1. [**Zhipeng Yu**, Yuchen Song], Tianting Zhong, Huanhao Li, Wei Zheng, and Puxiang Lai#, "Diffusive Optical Logic (DOL): Achieving multifunctional and reconfigurable optical logic operations with wavefront shaping" (*under review*).

2. Qi Zhao, Chiman. Woo, Huanhao Li, Tianting Zhong, **Zhipeng Yu**#, and Puxiang Lai#, "A parameter-free optimization algorithm for wavefront shaping" (*under review*).

3. [Huanhao Li, **Zhipeng Yu**, Yunqi Luo], Tianting Zhong, Yuanjin Zheng#, and Puxiang Lai#, "Learning-based bit-depth enhancement for optical speckles" (under review).

4. [Huanhao Li, **Zhipeng Yu**, Yunqi Luo], Shengfu Cheng, Lihong V. Wang, Yuanjin Zheng#, and Puxiang Lai#, "Learning-based image super resolution for sub-Nyquist sampled optical speckles" (under review).

5. [Huanhao Li, Chi Man Woo], Tianting Zhong, **Zhipeng Yu**, Yunqi Luo, Yuanjin Zheng, Xin Yang, Hui Hui#, and Puxiang Lai#, "Adaptive optical focusing through perturbed scattering media with dynamic mutation algorithm", *Photonics Research* 9(2), 202-212 (2021).

6. [Zihao Li, **Zhipeng Yu**, Hui Hui], Huanhao Li, Tianting Zhong, Honglin. Liu, and Puxiang Lai#, "Edge enhancement through scattering media enabled by optical wavefront shaping", Photonics Research 8(6), 954 (2020).

7. [Tianting Zhong, **Zhipeng Yu**], Huanhao Li, Zihao Li, Huanhao Li, and Puxiang. Lai[#], "Active wavefront shaping for controlling and improving multimode fiber sensor", *Journal of Innovative Optical Health Sciences*, 12(4), 1942007 (2019).

8. **Zhipeng Yu**, Meiyun Xia, Huanhao Li, Tianting Zhong, Fangyuan Zhao, Hao Deng, Zihao Li, Deyu Li, Daifa Wang, and Puxiang. Lai[#], "Implementation of digital optical phase conjugation with embedded calibration and phase rectification", *Scientific Reports* 9, 1537 (2019).

9. Huanhao Li, Fei Cao, Yingying. Zhou, **Zhipeng Yu,** and Puxiang Lai[#], "Interferometry-free noncontact photoacoustic detection method based on speckle correlation change", *Optics Letters* 44(22), 5481-5484 (2019).

10. **Zhipeng Yu**, Jiangtao Huangfu, Fangyuan Zhao, Meiyun. Xia, Xi Wu, Xufeng Niu, Deyu Li, Puxiang Lai[#], and Daifa Wang[#], "Time-reversed magnetically controlled perturbation (TRMCP) optical focusing in scattering media", *Scientific Reports* 8, 2927 (2018).

11. Jung Hoon Park, **Zhipeng Yu**, Kyeo Reh Lee, Puxiang Lai, and YongKeun Park[#], "Perspective: Wavefront shaping techniques for controlling multiple light scattering in biological tissues: toward *in vivo* applications", *APL Photonics* 3(10), 100901 (2018).

Conference Presentation

1. **Zhipeng Yu**, Zihao Li, Yuchen Song, Hui Hui, Puxiang Lai "An optical phase

conjugation-based tunable edge enhancer through scattering media" Photonics Asia 2020, Advanced Optical Imaging Technologies, China (Oral).

2. **Zhipeng Yu,** Puxiang Lai, "Optical focusing and imaging through scattering media with digital optical phase conjugation (DOPC)". The 10th International Conference on Information Optics and Photonics (CIOP2018), Beijing, China, 2018 (Oral).

ACKNOWLEDGEMENT

It is unbelievable that my pursuing the doctoral degree is almost coming to the destination. It seems that I started this journey just yesterday. First of all, I would like to express my hearty thanks to Prof. Puxiang Lai who is my chief supervisor. He provided a lot of support to my research and cooperation opportunities with other labs for me to learn different knowledge and techniques. Under his guidance and supervision, I learned how to keep an optimistic mind, keep walking after facing obstacles for many times, conduct independent research, be a future educator, and be open-minded in new things. All these will be my treasure in the following days and years.

I would also like to express my gratitude towards all members in Biophotonics Lab. They made every day here enjoyable and the lab a great place for research. I always had nice talks with Huanhao and Tianting, and I could always make progress on research through their feedback in the last years. Yingying always shared her research experiences and funny things of other labs. Yuchen Song and Jing Yao helped me do many efforts in engineering work and optical system building. Zihao Li, Chiman Woo, and Qi Zhao could devote themselves to conduct experiment to verify my ideas during the period of cooperation. Xiazi Huang, Fei Cao, and Shengfu Cheng gave me a lot of support in my research.

I would also like to thank collaborators (Prof. Daifa Wang at Beihang University, Prof. Qiuqiang Zhan at South China Normal University, and Prof. Wei Zheng in Shenzhen

Institutes of Advanced Technology of Chinese Academy of Sciences) in other universities/institutes. I learned a lot through talking and working with them. I need to thank other teachers/professors and staffs in BME of The Hong Kong Polytechnic University as well for their support to make my research and daily life more smoothly. The University has provided me a great platform to conduct the research and grow from different aspects in the past years.

Finally, I must take this chance to give my sincerest gratitude to my parents, Changming Yu and Qunzhen Zou. They are always supporting me unconditionally just like I was in the primary school and the high school. Same thankfulness goes to my wife and my son. In the past years, my wife, Qiuyue Mao, took on most family obligations so that I could focus on my study. My one-year-old son, Yi Yu, gives me an amazing experience to learn to shoulder more responsibility.

TABLE OF CONTENTS

LIST OF TABLES

LIST OF FIGURES

LIST OF ABBREVIATIONS

Abbreviation	Expatiation
BA	bat algorithm
CCD	charge coupled device
CI	complex interferogram
CPP	compensation phase pattern
DMD	digital micromirror device
DOL	diffusive optical logic
DOPC	digital optical phase conjugation
EI	enhancement index
ENR	enhancement-to-noise ratio
EOM	electro-optic modulator
FPGA	field programmable gate array
FWHM	full width at half maximum
GA	gentic algorithm
LCoS	liquid-crystal-on-silicon
M.E.	modulation efficiency
MD	modulation depth
MEMS	micro-electro-mechanical system
MMF	multimode fiber
MFP	mean free path
NIR	near infrared
OCT	optical coherence tomography
OPC	optical phase conjugation

PA	photoacoustic
BR	peak-to-background ratio
PCM	phase conjugation mirror
PLLA	polylactic acid
PSO	particle swarm optimization
ROI	region of interest
SA	simulated annealing
sCMOS	scientific CMOS
SLM	spatial light modulator
SMF	single-mode fiber
SPC	spiral phase contrast
STED	stimulated emission depletion
TM	transmission matrix
TMFP	transport mean free path
TRAP	time-reversed adapted-perturbation
TRMCP	time-reversed magnetically controlled perturbation
TROVE	time reversal of variance-encoded
TRUE	time-reversed ultrasonically encoded
WFS	wavefront shaping

Chapter 1: Introduction

1.1 Light Scattering

Over the past few decades, optical methods have been playing an important role in biomedical imaging and treatement[1,2]. Light enables people to see microorganisms and cells clearly with diffraction-limited sub-micron resolution, which has greatly promoted the advancement in various fields and deepened people's cognition about microcosmos. In the past 30 years, a many of optical imaging techniques, such as confocal microscopy[3-5], two-photon microscopy[6-9], stimulated emission depletion (STED) microscopy[10-14], optical coherence tomography (OCT)[15-20], and light sheet microscopy[21-24], have sprung up like mushrooms after rain. These techniques have become powerful tools underpinning the progress of scientific research and brought human cognition to a new level. Although these achievements are heart-stirring, the limitation should not be neglected: none of these high-resolution modalities can see through or within thick biological tissue. This is because light is multiply scattered due to the inhomogeneities of refractive index in tissue, and information encoded by the medium and the target is scrambled.

Significant progress has been made in overcoming this challenge in the past three decades. For example, a laser beam of a wavelength of 1700 nm has been used to excite three-photon fluorescence emission that elevates the imaging depth up to 1 mm within

an intact mouse brain based [25-28]. Adaptive optics approaches, inspired by recent developments in astronomical technology, have also been exploited to compensate for low order optical aberrations in tissue[29-37]. None of these approaches, however, can go beyond the diffusion limit, which is ~1 mm beneath human skin, where the majority of photons have been overwhelmingly scattered and become useless for ballistic imaging.

The situation is very similar for optical manipulation within or through thick scattering media. Conventional schemes, by using objective lens for example, can only focus visible light to shallow depths of a few hundred micrometers[1,38,39]. With the increase of propagation distance, the number of ballistic photons decays exponentially and becomes obsolete beyond the diffusion limit. However, unless being absorbed, these scattered photons do not disappear; they become diffusive and travel along random optical paths, forming speckle patterns if the coherence length of light is sufficiently long[38,40].

There exist three scattering regimes, depending on the relative size of the scattering particle to the wavelength of light[41]. In the first case, the scatterer is much larger than the wavelength of light, and geometric optics is sufficient to depict the scatterer-light interaction. In the second case, termed as Rayleigh scattering, the scattering particle is much smaller than the wavelength of light. In the third case, termed as Mie scattering, the optical wavelength is comparable to or of the same magnitude of the particle size. Both Rayleigh and Mie scatterings occur in biological tissues, yet Mie scattering is

usually dominant. Rayleigh scattering can be induced by the membrane structures and subcellular components such as macromolecules, while Mie scattering can be attributed to lysosomes, vesicles, mitochondria, *etc*[42] inside biological tissue.

The intensity distribution of Rayleigh scattering events is inversely proportional to λ^4, indicating the preferential scattering of shorter wavelengths in the Rayleigh regime[43,44]. Mie scattering can be described by the Mie solution to the Maxwell's equations, in which a plane monochromatic wave is incident on an isotropic scatterer[43]. Some parameters can be used to quantify the process of light scattering in complex media. Scattering coefficient μ_s (mm^{-1}) describes a fractional decrease of light intensity per unit distance due to the scattering and mean free path (MFP) l_s (mm) is the reciprocal of scattering coefficient. The decay of ballistic and quasi-ballistic light intensity (I_b) when penetrating through a thin scattering medium can be derived by Beer's law:

$$I_b = I_o \exp(-\mu_s l), \tag{1.1}$$

where I_o is the incident light intensity, and l is the thickness of the scattering medium[43]. Note that photons are isotropically scattered in the Rayleigh system, while in the Mie category they are mainly forward scattered. Thus, the scattering medium exhibits anisotropic patterns of scattering, which can be characterized by an anisotropy coefficient ***g*** expressed by:

$$g=\langle \cos\theta \rangle, \tag{1.2}$$

where θ is the scattering angle between the incident and scattered light paths. The

value of g ranges from 0 to 1 based on the above equation, and a larger value represents a higher degree of forward scattering. Incorporating the factor of anisotropy of the scattering events, reduced scattering coefficient $\mu_s^{'}$ (mm^{-1}) and transport mean free path (TMFP) $l_s^{'}$ (mm) are often used, which are expressed by:

$$\mu_s^{'} = \mu_s(1-g) \tag{1.3}$$

$$l_s^{'} = 1/\mu_s^{'} = l/(1-g) \tag{1.4}$$

TMFP is an important parameters to define ballistic (including quasi-ballistic) and diffusive regimes. Within one TMFP, it is described as ballistic (quasi-ballistic) regime, where photons are scattered by one or several times but still retain the memory of the orientation and information of incident light; beyond one TMFP is the diffusive (quasi-diffusive) regime, where photons have been excessively scattered so that the incident information is completely scrambled and cannot be untangled directly.

It should be noted that the optical properties of biological tissues are typically wavelength dependent. For example, reduced scattering coefficient reduces overall with optical wavelength. That is why near infrared (NIR) light, especially NIR-II region light, may penetrate up to over 1 mm, but visible and UV light is confined within several hundred microns underneath tissue surface. Thus, the imaging depth of multi-photon microscopy can be larger than 1mm[25,27], but confocal microscopy cannot[45].

1.2 Methods to overcome light scattering

Noninvasive optical focusing at depths in tissue has long been sought yet considered challenging due to the complexity of the multiple scattering[46], which is jointly influenced by the scattering medium and the incident photons. In the 1980s, researchers discovered that the ostensibly random scattering events and the resultant speckles are actually deterministic within the speckle decorrelation window[47,48]. Since then, some wavefront engineering approaches have been developed to pre-compensate or reverse the scattering-induced phase distortions, which correspond to wavefront shaping (WFS) [49-54] and optical phase conjugation (OPC)[55-57], respectively. As a result, diffused light travelling along different optical paths may interfere constructively again at the target position, forming an optical focus out of the seemingly random speckle background.

1.2.1 Wavefront shaping

The basic principle of wavefront shaping is to spatially modulate the wavefront of incident light in a way so that the scattering-induced phase distortions in the scattering medium can be pre-compensated. This technique was first introduced in 2007 by I.M. Vellekoop *et al.*[58]. They used a liquid-crystal-on-silicon (LCoS) spatial light modulator (SLM) as the phase modulator, with up to 3,228 independently controlled pixels to manipulate the phase of each individual input mode. A charge coupled device (CCD) camera was placed to monitor the light intensity at a target position behind a scattering medium. In order to maximize the intensity of a chosen area (output mode) recorded by the camera, the phase of each input mode (SLM pixel) was tuned from 0 to 2π. The

optimization process of the input phase was governed by a genetic algorithm (GA), in which the instantaneous light intensity read from these specific camera pixels served as feedback. The value that yielded the highest feedback was assigned as the optimum phase for that specific SLM pixel and each pixel went through such an iterative process. After phase optimization, a sharp optical focus behind the scattering medium can be obtained (Fig. 1.1a). As control, if phase modulation was not employed, a fully developed speckle pattern is observed (Fig. 1.1b), which also indicates sufficient optical diffusion due to the scattering medium. Further analysis of a fully developed speckle can be referred to Ref. [38].

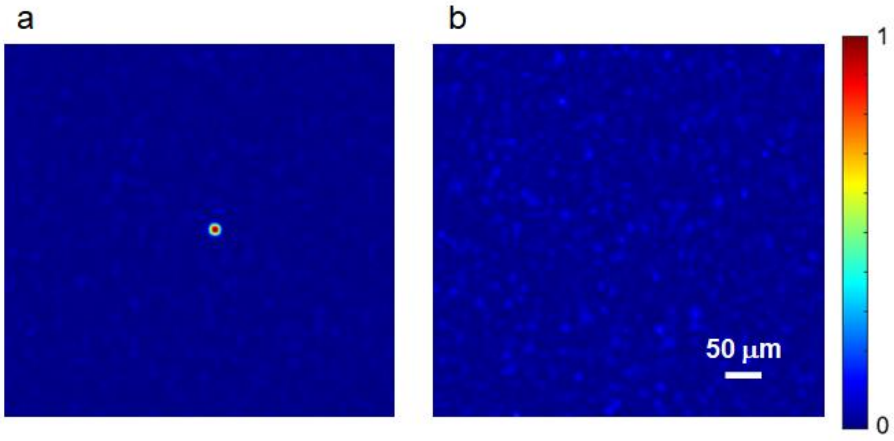

Fig. 1.1 (a) Optical focal pattern of the region with an optimized incident wavefront compensation by iterative wavefront shaping; (b) A typical optical speckle pattern behind a ground glass diffuser without wavefront shaping. The results were obtained by reproducing the process of the pioneer work by I.M. Vellekoop et al. [58] in the lab.

This iterative method is quite straightforward and can be applicable in many scenarios, where the system is treated as a black box. But it will be useless when researchers want to decipher the relationship between the output and input; such relationship is encoded with essential properties of the scattering medium, such as the optical transmission

eigenchannels inside the medium[59]. It is, therefore, necessary to view the black box from another perspective. As known, the transmission of photons in scattering media is deterministic at the macro level within the speckle decorrelation window, and the output light field has a certain relationship with the input. If this relationship is deciphered in advance, the resultant output light pattern can be shaped into a desired one by displaying an engineered wavefront at the incident plane. Popoff *et al.* proposed to employ a scattering transmission matrix (TM) to demonstrate such relationship[60]. They chose a Hadamard basis as the input displayed on a phase-only SLM and combined a common-path interferometry with a four-phase shift method to measure the TM of an opaque thick deposit of ZnO. The measured TM can be utilized to focus light into any desired region at the output plane. The relationship between the input field (E_{in}) and the output field (U_{out}) can be written as:

$$U_{out} = TE_{in} = \begin{bmatrix} t_{1,1} & \cdots & t_{1,n} & \cdots & t_{1,N} \\ \vdots & & \vdots & & \vdots \\ t_{k,1} & \cdots & t_{k,n} & \cdots & t_{k,N} \\ \vdots & & \vdots & & \vdots \\ t_{K,1} & \cdots & t_{K,n} & \cdots & t_{K,N} \end{bmatrix} \begin{bmatrix} e_1 \\ \vdots \\ e_n \\ \vdots \\ e_N \end{bmatrix} = \begin{bmatrix} u_1 \\ \vdots \\ u_k \\ \vdots \\ u_K \end{bmatrix}, \tag{1.5}$$

where $\boldsymbol{T}$ represents the transmission matrix of the scattering medium. Thus, every output mode is the superposition of all input modes weighted by the values on the corresponding row vector of TM:

$$u_k = \sum_{n=1}^{N} t_{k,n} \cdot e_n \,. \tag{1.6}$$

As a scattering TM is sufficiently informative to depict the multiple scattering in a complex medium, the inverse matrix of the TM can be used to calculate the required input pattern displayed on the SLM so as to obtain a desired output field.

In recent years, wavefront shaping techniques, including both iterative- and TM-based approaches, have underpinned many exciting advancements. Most endeavors have been centering around improving the focal intensity enhancement ratio, accelerating the optimization process, or exploring noninvasive guidestars to produce feedback signals.

Higher focal intensity within or through turbid media can create new possibilities for high-resolution imaging and efficient delivery of energy at depths. Although the intensity enhancement ratio at the region of interest (ROI) before and after the optimization may vary from case to case, it is overall proportional to $\alpha \cdot N$, where N is the number of independently controlled elements on the SLM, and α is a constant depending on the type of wavefront modulator and the efficiency of the algorithm as well as the system. Therefore, to achieve a higher enhancement ratio, larger N and α are required. For example, Yu *et al.* obtained an optical focus with an enhancement ratio greater than 100,000 using a one-megapixel digital micromirror device (DMD), a type of binary amplitude modulator, in a 73-minute optimization[61]. In the last decade, many swarm intelligence algorithms have also been introduced to replace GA to improve the focusing efficiency, such as simulated annealing algorithm (SA)[62], particle swarm optimization (PSO)[63], and bat algorithm (BA)[64],

To enable wavefront shaping in a real scene (with dynamic medium or environment), the optimization process should be shorter than the decorrelation time window of the

system. For wavefront shaping, the required optimization time is directly proportional to the used number of control modes on the modulator. To improve the speed, a faster wavefront shaper is preferred. In the early days, researchers used LCoS-SLM as the modulator, which took several minutes to several hours[49,58] to obtain a focus due to the very limited frame rate of the SLM. Later, Blochet *et al.* introduced a micro-electro-mechanical system-based (MEMS) SLM, a fast photodetector, and field programmable gate array electronics to shorten the optimization cycle to several hundred milliseconds[65]. Caravaca-Aguirre *et al.* employed a DMD with updating rate of 23 kHz to further shorten the optimization process down to 37 ms, with which a real-time resilient focusing through a bending multimode fiber can be achieved[66]. More recently, Tzang *et al.* used a microelectromechanical grating light valve, an one-dimensional (1D) SLM with updating rate of 350 kHz, to obtain a focus through dynamic scattering media within 2.4 ms[67].

To focus light inside or through a scattering medium by wavefront shaping, a guidestar must be created to produce a feedback signal that is proportional to the *in situ* optical flux. Fluorescence beads[57,68], a CCD camera[58], and a photodiode[61,69] were first used as guidestars or devices to gauge the strength of scattered photons. These methods can either be used to focus light outside the scattering medium or to focus light inside the scattering medium in an invasive manner, limiting further applications of wavefront shaping. Recently, photoacoustic (PA) imaging has been introduced to overcome the diffusion-induced resolution barrier in deep tissue [43,46,70-72]. This technique is based on

PA effect [73-75] , in which ultrasonic waves, called photoacoustic waves, are generated due to optical absorption. Since the ultrasonic waves are scattered almost 1000 times less than light in tissue, they can be used to reconstruct an image of the absorbing ROI with acoustic resolution[50,53,60,69,76-79]. As PA signal can be generated by either ballistic or diffusive excitation light, it allows for a penetration depth far exceeding the optical diffusion limit. The photoacoustic signal can, in principle, serve as an internal guidestar inside the scattering media for wavefront shaping. Kong *et. al* firstly used a deformable mirror to maximize the photoacoustic signal through optically diffusive media by using photoacoustic-guided interferometric focusing[80]. Chaigne *et. al* developed a photoacoustic transmission matrix based wavefront shaping with an ultrasound array to achieve two-dimensional photoacoustic imaging over a large field of view without scanning[53,81]. Conkey *et. al* achieved super-resolution photoacoustic imaging through a scattering wall by combining the spatially non-uniform sensitivity of the ultrasound transducer to the detection of generated photoacoustic waves with an evolutionary competition among optical modes[82]. Lai *et al.* proposed to use nonlinear photoacoustic signals based on Grueneisen relaxation effect as feedback to obtain an optical focus of 5–7 μm in diameter with an peak intensity enhancement ratio of ~6,000[49].

1.2.2 Optical phase conjugation

The other popular method to overcome scattering is via optical phase conjugation. The concept of OPC was first introduced in the 1970s based on stimulated Brillouin scattering, three-wave mixing, and four-wave mixing[83-90], with all experiments

conducted in free space or a weak scattering environment. The implementation of OPC for compensating strong scattering pf biological tissues was first demonstrated in 2008 by using a 0.075% Fe-doped $LiNbO_3$ crystal[55]. The procedure was divided into two steps: phase recording and phase reading. During the stage of phase recording, a sample optical beam transmitted through a piece of 0.69-mm-thick chicken breast tissue and then interfered with a reference optical beam. The resultant hologram was written into the photorefractive crystal. During the stage of phase reading, a third optical beam, a conjugated copy of the reference beam, was projected onto the crystal, which generates a fourth beam that is conjugated to the sample beam. At last, the conjugated sample beam propagated back through the tissue and reconstructed the original light field before scattering.

In these processed, the photorefractive crystal actually functions as a phase conjugate mirror (PCM). To explain the principle of OPC, the basic properties of PCM will be introduced in this section. At the same time, the transmission characteristics of conventional mirror will be discussed for comparison. It is assumed that the reflectivity of the conventional mirror and the PCM are both 100% for the sake of simplification. In free space, an optical beam projected obliquely onto a conventional mirror is reflected and transmits along a direction following Snell's law, as shown in Fig. 1.2a. That is,

$$\begin{aligned} E_{in} &= A\exp\left[i\left(k_v \cdot r_v + k_p \cdot r_p \right) \right] \\ E_{out} &= A\exp\left[i\left(-k_v \cdot r_v + k_p \cdot r_p \right) \right], \end{aligned} \tag{1.7}$$

where k_v and k_p are the components of optical wave vector vertical and parallel to the mirror plane, respectively. Note that only the vertical component of the wave vector is reversed by the conventional mirror. In contrast, when an optical beam is projected onto a PCM obliquely, it will be reflected and transmit back along the original path, and the reflected light is conjugated to the original beam, as shown in Fig. 1.2b. That is,

$$\begin{aligned} E_{in} &= A\exp\left[i\left(k_v \cdot r_v + k_p \cdot r_p \right) \right] \\ E_{out} &= A\exp\left[i\left(-k_v \cdot r_v - k_p \cdot r_p \right) \right] = (E_{in})^* \end{aligned}, \tag{1.8}$$

where * represents complex conjugate. All components of the wave vector of light are reversed. In other words, the wave vector of light changes its sign when the light is reflected by a phase conjugation mirror. It seems that the light is time-reversed by the phase conjugation mirror and this is why phase conjugation is also known as “time reversal”.

The time reversal process with the presence of scattering is illustrated in Fig. 1.2c, where light carrying the information of a butterfly pattern (E_1) transmits through a scattering medium and becomes E_2 (an opaque bottle in the figure represents the scattering medium). As a result, a distorted butterfly pattern is observed (only the phase variation of the light is taken into consideration).

$$\begin{aligned} E_1 &= \sum_{j=1}^{N} \exp\left[i\left(\mathbf{k} \cdot \mathbf{r} \right) \right] \\ E_2 &= \sum_{j=1}^{N} \{ \exp\left[i\left(\mathbf{k} \cdot \mathbf{r} \right) \right] + \phi_j \} \end{aligned}, \tag{1.9}$$

where ϕ_j is the phase distortion induced by the bottle, and $\boldsymbol{k}$ is the wave vector (only the light vertical to the mirror plane is considered, as oblique light will be blocked due

to the limited acceptance angle of the system). If the scattered light is reflected by a conventional mirror put behind the medium, it becomes E_3 and travels back through the medium again. As a result, E_4 is obtained and a doubly distorted butterfly pattern is observed.

$$\begin{aligned} E_3 &= \sum_{j=1}^{N} \{\exp\left[i\left(-\mathbf{k}\cdot\mathbf{r}\right)\right] + \phi_j\} \\ E_4 &= \sum_{j=1}^{N} \{\exp\left[i\left(-\mathbf{k}\cdot\mathbf{r}\right)\right] + 2\phi_j\} \end{aligned} . \tag{1.10}$$

In contrast, the situation is very different if a phase conjugation mirror is used. The scattered light is also reflected by the phase conjugation mirror and becomes $E_3^{'}$, which is projected back through the scattering medium and becomes $E_4^{'}$. As seen, the scattered-induced phase distortions are compensated. As a result, a fully recovered butterfly pattern can be observed.

$$\begin{aligned} E_3^{'} &= \sum_{j=1}^{N} \{\exp\left[i\left(-\mathbf{k}\cdot\mathbf{r}\right)\right] - \phi_j\} \\ E_4^{'} &= \sum_{j=1}^{N} \exp\left[i\left(-\mathbf{k}\cdot\mathbf{r}\right)\right] = (E_1)^* \end{aligned} . \tag{1.11}$$

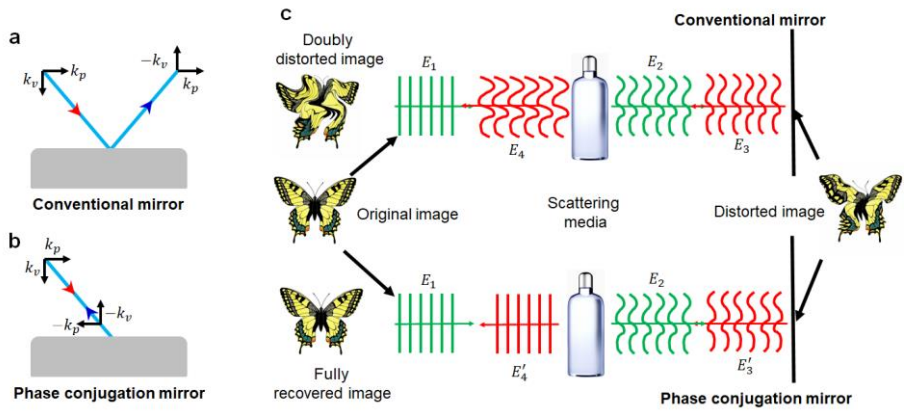

Fig. 1.2 Comparison between a phase conjugate mirror and a conventional mirror. a-b: Two dimensional representations of wavevectors reflecting off a conventional mirror and a phase conjugate mirror, respectively. c: In the presence of scattering, a conventional mirror and a

phase conjugate mirror are used to reflect scattered light, respectively.

A transmission matrix model can further explain the working principle of OPC from a different aspect. In the phase recording stage, the incident light field, denoted as U_{in}, yields a resultant field out from the scattering medium, defined as U_s. Their relationship can be expressed by

$$U_s = TU_{in}, \tag{1.12}$$

where T is the transmission matrix of the scattering medium. In the phase reading stage, the light field at the PCM plane is modulated to U_s^* (* represents complex conjugate), and the light back to the original plane (U_{out}) can be expressed by[91]

$$U_{out} = T^t U_s^* = (T^\dagger T U_{in}) \approx U_{in}^*, \tag{1.13}$$

where $\boldsymbol{t}$ represents transposition, and † represents complex conjugate transpose. Approximately, $T^\dagger T \approx I$ ($\boldsymbol{I}$ is the identity matrix), assuming the system is time invariant during the whole process including both phase recording and reading. As seen, the output light field conjugates to the original incident light field.

Such an OPC system using photorefractive material as the phase conjugation mirror is often referred as analog OPC. This analog OPC only contains two steps (phase recording and reading) without an iterative process, so its optimization speed can be very fast[92]. Also, both phase recording and reading are accomplished inside the crystal and hence the system is rather strgaightforward[55,93]. The scheme, however, sees a drawback as it lacks the freedom to manipulate the recorded hologram information and hence the phase conjugated light[94]. Moreover, analog OPC usually suffers from limited

attainable optical energy for the phase conjugated light because the hologram recorded temporarily in the crystal is erased during the reading stage[55,95].

To address these drawbacks, in 2012 researchers proposed a digital optical phase conjugation (DOPC) system for turbidity suppression in biological tissues[56,96]. Different from the analog version, DOPC system employs a well-aligned digital camera-SLM module as the phase conjugation mirror[56,57,97,98]. Reading out the hologram generates a phase conjugated copy of the original signal beam, which travels, albeit tortuously, back to the scattering medium and converges to the point of origin. Compared with analog OPC, DOPC shows great advantages in terms of the following two aspects. First, hologram recording and reading are separated into two independent steps, which are accomplished by the camera and SLM, respectively. Therefore, the conjugated version of the incoming wavefront, which is displayed on the SLM, can be arbitrarily modified for further purpose. Second, the power of the phase conjugated light, which is converted from the reference beam by the phase conjugation mirror, has no upper limit except for the damage threshold of the SLM.

In the past few years, efforts on DOPC have been focused on improving the optimization speed and developing effective guidestars as the internal feedback. Without iterative process, DOPC shows great advantages over WFS in terms of speed. However, the speed of DOPC is still under optimized. The slow refresh rate of LCoS-SLM (with updating speed up to 60 Hz) and the computer data transfer have made it

difficult for DOPC to achieve a playback latency shorter than ~200 ms. Wang *et al.* used a 23k Hz DMD and field programmable gate array (FPGA) to shorten the latency to 5.3 ms[99]. Liu *et al.* used a ferroelectric liquid crystal-based SLM to focus light through a 3-mm-thick moving chicken tissue sample with a 3.0 ms latency, and focused light inside a moving tissue with a 6.0 ms latency[100]. Moreover, in these two works, a single-shot measurement of the scattering wavefront (the reference beam should be measured in advance for comparison) was demonstrated to improve the speed by twice compared with the schemes using 4-phase shift. More recently, Cheng *et al.* reported a single-shot on-axis hologram method for obtaining optical focus inside scattering media without measuring the reference beam in advance, which successfully improves the speed by another two folds[101].

Focusing light inside a scattering medium is also critical for extending DOPC to biomedical applications. Embedded probes, such as fluorescent beads[56,57,102] and nanoparticles [103], can serve as guidestars. But the procedure of embedding these probes is invasive and the resultant focal positions are fixed and inflexible. Ultrasound waves, as discussed earlier, are scattered ~1000 times weaker than light is inside biological tissue. As a result, ultrasound waves can penetrate much deeper (up to several or tens of centimeters) than light in tissue. Moreover, diffused light can be spectrally encoded by ultrasound based on acousto-optic effect[104]. Therefore, ultrasonic mediation can serve as an encouraging noninvasive internal guidestar inside scattering media. Taking advantage of these characters, researchers have explored a series of ultrasound-assisted

DOPC techniques, such as time-reversed ultrasonically encoded (TRUE) optical focusing[92,93,96,105], time reversal of variance-encoded (TROVE) optical focusing[94]. More recently, moving absorbers[91,106] and microbubble collapsing induced optical perturbations[107] have also been introduced as internal guidestars. Benefiting from the effective internal guidestar, researchers proposed to combine TRUE optical focusing with optogenetics to modulate the neural activity inside an 800 μm-thick mouse brain slice[108].

1.3 Selection of different spatial light modulators in this thesis

There are two types of modulators, LCoS-SLM and DMD, used in this thesis. The differences between them are demonstrated in three aspects below. Firstly, As talked in the above section, the intensity enhancement ratio at the region of interest (ROI) is $\alpha \cdot N$. α is about 0.78 for a LCoS-SLM but only around 0.16 for a DMD[109]. In addition, as DMD is a binary intensity modulator and a LCoS-SLM is an 8-bit phase modulator, the wavefront modulation accuracy using a LCoS-SLM is much higher than with a DMD. At last, DMD works at a very fast update speed up to 23 kHz, while the update speed of LCoS-SLM is usually 60 Hz[52].

Some other factors also influence the choice. For example, DMD can be used to replace LCoS-SLM in DOPC to improve the speed for in vivo biomedical applications[99], but the system complexity is much higher as the incident light and the reflected light transmit at different angles using a DMD, which causes challenges to the conjugation

between the modulator and the digital camera. In addition, neither DMD nor LCoS-SLM is cheap (about tens of thousands of US dollars)[52], which also influences the selection.

Taking all the factors into consideration, in Chapters 2, 3, and 4, the focus efficiency and the wavefront modulation accuracy have priority, but in Chapter 5, the focusing optimization speed is more concerned. So, a LCoS-SLM is used in Chapters 2, 3, and 4, while a DMD is used in Chapter 5.

1.4 Outline of this thesis

My PhD research mainly focuses on developing functionalities and scopes of wavefront engineering for biomedicine and optical computing. The thesis is arranged by the wavefront manipulation complexity from optical focusing, image edge enhancement, to multifunctional diffusive optical logic gates. In Chapter 1, a general introduction of scattering and concepts of wavefront engineering are reviewed, together with the development of wavefront engineering in the last decade. In Chapter 2, an embedded calibration and phase rectification method is developed to improve the performance of DOPC for optical focusing inside/through scattering media. In Chapter 3, a new approach Time-reversed magnetically controlled perturbation (TRMCP) is proposed, where magnetically manipulated optical absorbing microspheres serve as internal guidestars for DOPC to achieve optical focusing inside scattering media. In Chapter 4, a tunable object edge enhancer through turbid media is introduced by simply adjusting

the intensity ratio between the reference beam and sample beam in DOPC. In Chapter 5, a diffusive optical logic (DOL) scheme assisted by transmission matrix-based wavefront shaping is developed to achieve multiple logic functions (AND, OR, NOT, NAND, NOR) through a ground glass on one platform. In Chapter 6, the major achievements were summarized together with the limitations of wavefront engineering for in-depth exploration in biomedicine, and the development of wavefront engineering beyond biomedicine was discussed.

Chapter 2: Implementation of digital optical phase conjugation with embedded calibration and phase rectification towards high-quality optical focusing through scattering media

This chapter is reproduced with some adaptations from the manuscript "Zhipeng Yu, Meiyun Xia, Huanhao Li, Tianting Zhong, Fangyuan Zhao, Hao Deng, Zihao Li, Deyu Li, Daifa Wang, and Puxiang Lai, "Implementation of digital optical phase conjugation with embedded calibration and phase rectification", Scientific reports 9 (1), 1537 (2019)". The contributions of authors are as follows: P. Lai and Z. Yu conceived the idea. Z. Yu, D. Wang, and P. Lai designed the system. Z. Yu, M. Xia, F. Zhao, Z. Li and D. Li ran the experiments. Z. Yu, H. Li, T. Zhong and P. Lai prepared the manuscript. All authors were involved in the analysis of the results and manuscript revision.

In this chapter, a plain yet reliable digital optical phase conjugation (one type of wavefront engineering) setup was presented with an embedded four-phase, non-iterative approach that can rapidly compensate for the wavefront modulator's surface curvature, together with a non-phase-shifting in-line holography method in the absence of an electro-optic modulator (EOM). In experiment, with the proposed setup the peak-to-background ratio (PBR) of optical focusing through a standard ground glass in experiment can be improved from 460 up to 23,000, while the full width at half

maximum (FWHM) of the focal spot can be reduced from 50 μm down to 10 μm. The focusing efficiency, as measured by the value of PBR, reaches nearly 56.5% of the theoretical value.

2.1 Introduction

As discussed in Chapter 1, DOPC was recently proposed by using a digital camera-SLM aligned module for hologram recording and reading [56,96,97,110-113]. In DOPC, the hologram recording and reading are physically separated—the former at the camera and the latter at the SLM—and can be arbitrarily controlled independently. The power of the phase conjugated light increases proportionally to the power of the reference light, and theoretically there is no boundary except for the damage threshold of the SLM. Furthermore, such a system allows for further manipulation of the optical wavefront prior to playback, and the response time of digital devices (cameras and SLM) can be tuned (limited by the minimum response time of the device). So, the experiment time can be adjusted arbitrarily for different purposes. These flexibilities have facilitated combination of DOPC with various modulating mechanisms, and have inspired a series of approaches that are able to achieve reliable optical focusing inside or through scattering media, such as time-reversed ultrasonically encoded optical focusing[96,108], time reversal of variance-encoded optical focusing[94], time-reversed adapted-perturbation [91] and time reversal by analysis of changing wavefronts from kinetic targets optical focusing[106].

The utility and extension of DOPC systems, however, have been practically throttled largely due to two critical requirements in system design and operation[114]. First, achieving accurate pixel-to-pixel match between the digital camera and the SLM is complicated and experience demanding; the camera and the SLM should be conjugated exactly with each other, and the mismatch must be limited within one pixel[91] in six dimensions, i.e., the three displacement axes ($\Delta x, \Delta y, \Delta z$) and the three angle axes ($\Delta\beta_x, \Delta\beta_y, \Delta\beta_z$)[114]. In addition, the flatness of SLM surface poses substantial influence to the focusing performance, such as the peak-to-background ratio (PBR) and FWHM of the focal spot[114]. These factors need to be tuned carefully in order to achieving robust performance, for which iterative calibration methods[114,115] have been proposed by Jang *et al.* and Azimipour *et al*., respectively. The implementation of these two methods, however, is time consuming (several minutes or even longer) as hundreds or even thousands of iterations are needed, and this calibration time length increases proportionally to the number of independently calibrated element on the SLM. Moreover, during the experiment when the system or the environment alters (e.g., strong air flow or accidental bumping to the optical table), the effect of the sought curvature compensation, and hence the focusing performance, may reduce considerably. In this case, an extended recalibration is inevitable, which interrupts or further slows down the experiment. On the other hand, to record the phase wavefront of the sample beam, an in-line or off-axis phase-shifting holography are needed[91,116]. In the in-line setting, an electro-optic modulator (EOM) is used to execute a four-phase digital holographic method to retrieve phase[91]. Note that using the EOM requires an accurate

pure phase modulation without amplitude modulation in the context, posing an extra burden to the optical system which has already been quite complicated for many researchers. In the off-axis setting, the distance between the digital camera and the SLM needs to be quite large in order to spatially separate the original and conjugated beams. The off-axis angle limitation brings extra complexity to the alignment, and the extended optical path length increases the system instability. In addition, some high frequency information may be lost due to the low utilization levels of the spatial bandwidth[117,118].

To address the aforementioned limitations, a plain yet reliable DOPC setup with an embedded four-phase, non-iterative approach that can rapidly compensate for the wavefront modulator's surface curvature was presented. Due to the lack of an EOM at hand, a non-phase-shifting in-line holography method is developed for effective phase retrieval, which further simplifies the system design and reduces the cost. Experimentally, optical focusing with a PBR of up to 23,000 has been obtained through a standard ground glass diffuser, with a FWHM focal spot of 10 μm. The focusing efficiency, as measured by the PBR, reaches nearly 56.5% of the theoretical value.

2.2 Methods

2.2.1 Optical setup

The experimental setup is shown in Fig. 2.1. A 532 nm continuous laser (EXLSR-532-200-CDRH, Spectra Physics) is used as the light source. Its coherence length is measured to be 300 m. The laser output is split into two beams, a sample beam and a

multipurpose beam (as the calibration beam, reference beam, and playback/reading beam) by a beam splitter (BS_1). A scientific CMOS camera (Camera 1, pco.edge 5.5, PCO) is used to image the diffused sample light exiting the scattering medium. A SLM (PLUTO-VIS-056, HOLOEYE) is positioned to conjugate to Camera 1 and phase modulate the playback beam. In additional to the abovementioned components, a single-mode fiber (SMF) and lens L_1 are used to shape the reference beam to be planar (25.4 mm in diameter), lens L_2 is used to collect light exiting the scattering medium and adjust the speckle grain size in Camera 1, and lens L_3 is positioned in front of Camera 1 to image the surface of the SLM or Mirror M_1. Four fast shutters ($FS_{1\text{-}4}$) are used to control the on and off of different optical beams. Another camera (Camera 2) is used to observe the time-reversed playback beam. The polarization of the reference beam is adjusted by one polarizer (P_1) to match the polarization of the SLM. The polarization of the sample beam is adjusted by another polarizer (P_2) to get maximal interference intensity between the sample beam and the reference beam.

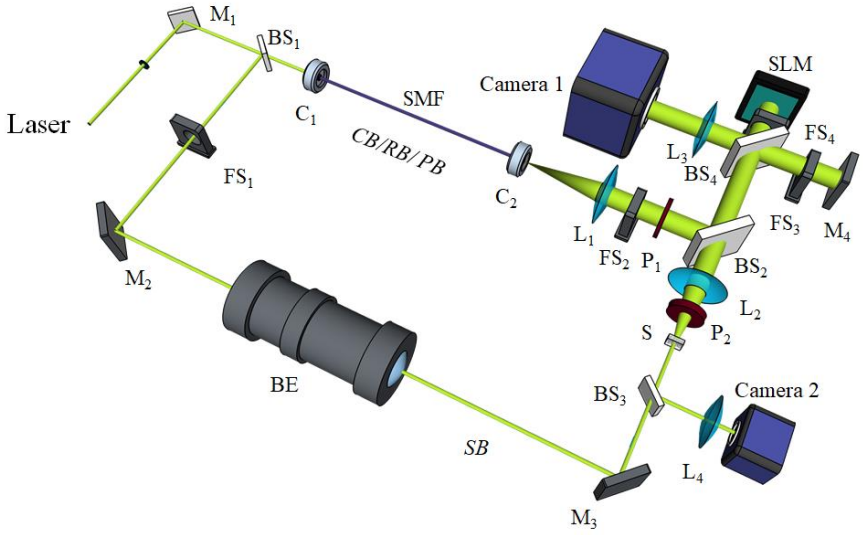

Fig. 2.1 Schematic of the DOPC system. CB/RB/PB/SB: calibration/reference /playback/sample beam; BE: beam expander; BS_1, BS_2: cube beam splitter; BS_2, BS_4: plate beam splitter; C_1, C_2: fiber port connector; Camera 1: scientific CMOS camera; Camera 2: CMOS camera; FS_1-FS_4: fast shutter; HWP: half-wave plate; L_1, L_2, L_4: Plano-convex lens; L_3: camera lens; $M_{1\text{-}4}$: mirror; PBS: polarized beam splitter; $P_{1,\,2}$: polarizer; S: scattering medium; SLM: spatial light modulator; SMF: single mode fiber.

2.2.2 SLM curvature compensation

In experiment, a complete DOPC operation is divided into three stages (Fig. 2.2): the embedded calibration stage, the phase recording stage, and the playback (also termed as “phase reading”) stage, which are described in detail below.

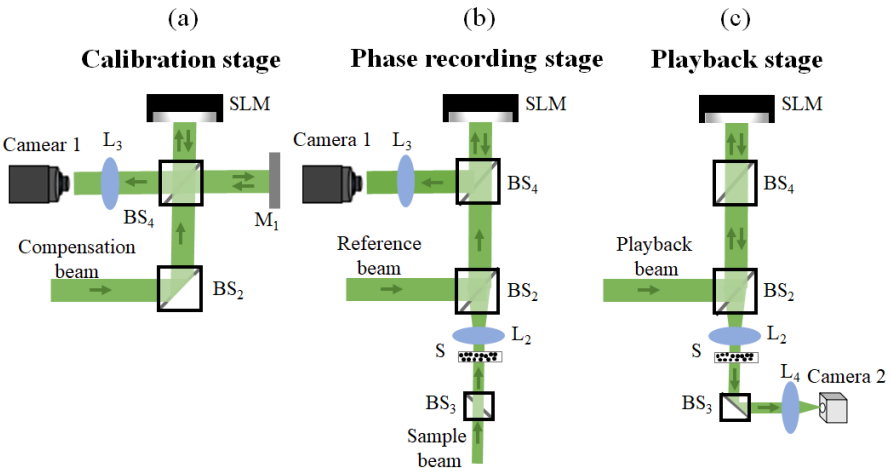

Fig. 2.2 Illustration of the calibration stage (a), the phase recording stage (b), and the playback stage (c).

As in Ref. [91], Camera 1 and the SLM are first aligned carefully to achieve a pixel-to-pixel mismatch of less than one pixel (Fig. 2.2a). After that, calibration of the reference beam imperfection and the SLM surface curvature are carried out, for which no extra optical paths are required. The SLM and a mirror (M_1) are adjusted to be completely perpendicular to the calibration beam by using a retroreflector. The calibration beam is thus reflected by the SLM and M_1, respectively, and the reflected beams interfere in Camera 1, with interference pattern recorded by the camera. Then the SLM is displayed with four uniform patterns with phase angle at 0, π/2, π, and 3π/2, respectively. The corresponding interferograms are recorded and denoted as I_k (k=1, 2, 3, 4), respectively (Fig. 2.3a-d). The four interferograms can compose a complex interferogram (CI)[91]. The CI and the system compensation phase pattern (CPP) that has taken into account the reference beam imperfection and the SLM curvature can be expressed by

$$CI = (I_1 - I_3) + i(I_2 - I_4) \tag{2.1}$$

$$CPP = \arg[\mathrm{Im}(CI) / \mathrm{Re}(CI)], \tag{2.2}$$

where *arg* [ ] denotes taking the argument. The *CPP* can be obtained from the equations 2.1 and 2.2 and is shown in Fig. 2.3e. In experiment, this compensation pattern is implanted into the DOPC system, i.e., being added to the SLM pattern obtained from regular phase retrieval procedure.

The phase retrieval procedure spans the phase recording stage and the playback stage, as shown in Fig. 2.2b and c. In the phase recording stage, the sample beam is expanded and illuminates the front surface of the scattering medium. Distorted sample light exiting the medium is collected and relayed Camera 1, where it interferes with the reference beam. The interfering patterns are transferred to the computer to compute the optical field, whose phase conjugation is then transferred to the SLM. In the playback stage, the sample beam is blocked, and the playback beam illuminates the SLM, generating a phase conjugated copy of the original sample beam, which travels back to the scattering medium and converges to the position of incidence at the front surface of the first scattering sample.

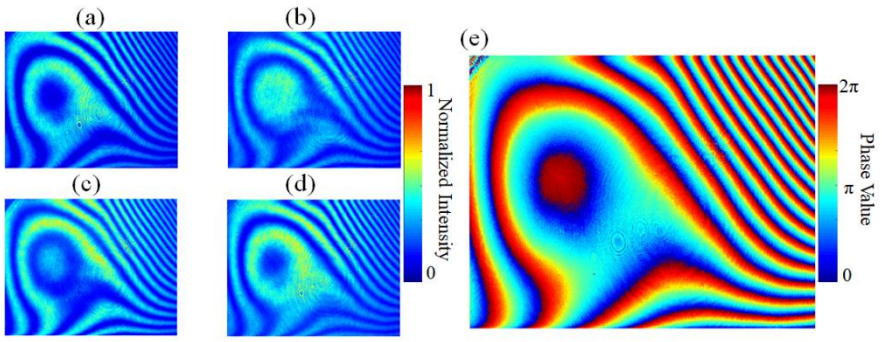

Fig. 2.3 Four interferograms are recorded, when the SLM is displayed with four uniform patterns with phase angles at (a) 0, (b) π/2, (c) π, and (d) 3π/2, respectively. (e) The computed system compensation phase pattern corresponding to the four interferograms.

2.2.3 Phase retrieval with the phase rectification method

In the proposed non-phase-shifting in-line holography DOPC, the sample beam, the reference beam, as well as their interferogram are one-by-one recorded by Camera 1 as $\boldsymbol{I_s}$, $\boldsymbol{I_r}$, and $\boldsymbol{I_{int}}$, respectively. They are related by

$$I_{int} = I_r + I_s + 2\sqrt{I_r I_s}\cos(\theta), \tag{2.3}$$

where $\boldsymbol{\theta}$ is the phase difference between the reference beam and the sample beam. What should be noticed is that, according to equation 2.3, the phase information cannot be retrieved. The light field U can thus be expressed by $U = a + i \cdot b$ (a and b are real matrixes). Full-wave rectification of $\boldsymbol{U}$ is executed, as shown in Fig. 2.4a, producing a new light field $\boldsymbol{U'}$:

$$U' = a + i * |b|. \tag{2.4}$$

The performance of such a phase rectification-based DOPC is illustrated in Fig. 2.4a. As shown, OB and OC are the angle bisectors of the third and fourth quadrant, respectively, which equally divide the third and fourth quadrant into four sections, marked as Region I, II, III and IV. Assuming an original wave vector $OA = |a|\exp(i\alpha)$, where $|a|$ is the amplitude of the vector and $\pi < \alpha < 2\pi$ is the phase of the vector. After being rectified, the vector becomes $OA^* = |a|\exp(i(2\pi - \alpha))$. Projecting vector OA^* onto OA, the value of the corresponding component is $P = |a|\cos(2\pi - 2\alpha)$. If OA is Regions I or IV, **P** is greater than 0, and the rectificated vector poses a negative effect to the performance of DOPC; but if **OA** is in Regions II or III, **P** is less than 0, and the rectification affects the performance of DOPC positively.

Within or through a thick scattering medium where light is multiply-scattered, the phase profiles of the resultant optical field (i.e. speckle patterns) are randomly distributed, suggesting that the overall contributions of the positive and negative scenario cancel out. As a result, only the non-rectificated components function contributively to the PBR of DOPC. As known, with a full-phase modulation approach, the PBR of DOPC can be expressed by $PBR \approx \pi N / 4$ where N is the number of the controlled modes[58,91,99]. With the phase rectification-based DOPC proposed here, about half of the controlled modes have counteracted among themselves. Therefore, the theoretical PBR of this method is

$$PBR \approx \pi N / 8 . \tag{2.5}$$

Based on equations (2.1)-(2.4), the obtainable PBR is numerically calculated for full phase, phase rectification, and binary modulations[113], respectively, and is shown in Fig. 2.4b. One can see the ratios between the PBR and the controlled number are 0.73, 0.31, and 0.20, respectively. Moreover, this simulated ratio for phase rectification-based DOPC is fairly consistent with the theoretical value predicted from equations (2.5).

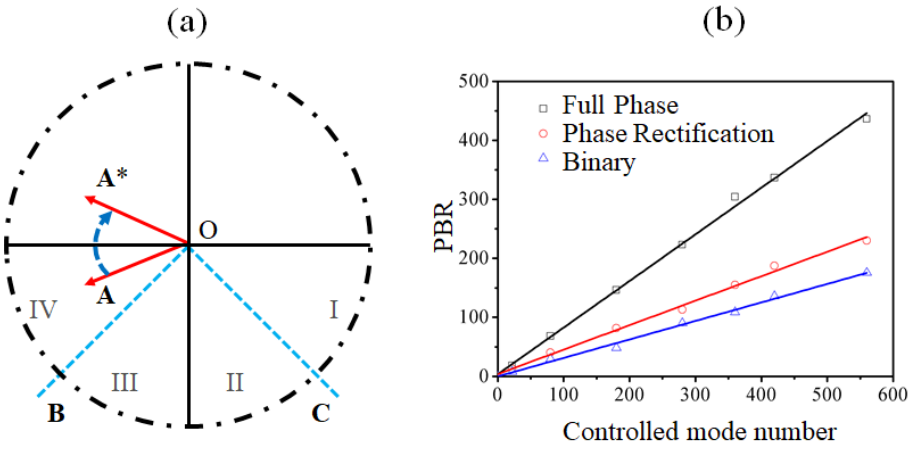

Fig. 2.4 (a) Illustration of the phase rectification-based DOPC using wave vector

decomposition; (b) The relationship between the theoretical PBR in DOPC and the controlled SLM pixel number using the full phase, phase rectification, and binary modulations, respectively.

2.3 Results and Discussion

Experiments were performed to validate the proposed DOPC setup. A ground glass (DG10-600, Thorlabs) was used as the scattering medium. When an optimized phase pattern was obtained and loaded on the SLM, an optical focus appeared as shown in Figs. 2.5b and c. Especially, with the proposed calibration and phase rectification, the PBR of the optical focus can go up to ~23,000 (Fig. 2.5c), and the focal spot is about 10 μm (FWHM) along both X and Y axes. Considering that the speckle size makes up about 20 pixels of the SLM and the number of independent control units on the SLM are 1920×1080, the theoretical PBR is about 40,700. In contrast, no focus can be observed when a random phase map was displayed on the SLM (Fig. 2.5a). Without the proposed SLM calibration, a spatially uneven optical focus achieved yet with a PBR of only ~460 and a FWHM dimension of 50 μm. Therefore, the method can improve the DOPC performance by 50 and 5 times regarding the PBR and the focal spot size, respectively. Moreover, the experimentally achieved PBR of 23,000 has reached ~56.5% of the theoretical one, which, to be best of our knowledge, approaches to the highest focusing efficiency (66% in Ref. [114]) for all DOPC experiments reported thus far.

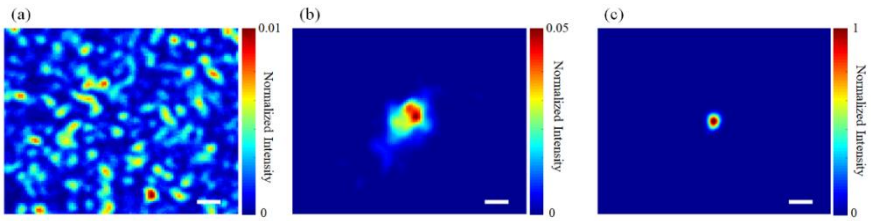

Fig. 2.5 (a) The optical field recorded by Camera 2 when the SLM is displayed a random phase pattern, showing a random speckle pattern. (b) When the SLM was loaded with the optimized phase pattern before calibration, an optical focus was formed with a PBR of ~460. (c) When the SLM was loaded with the optimized phase pattern after calibration, the PBR of the optical focus can be up to ~23000. The scale bars represent 50 μm. The color bars in (a) and (b) are normalized to the peak intensity in (c).

In order to test the ability of the system for optical focus inside scattering media, a set of time-reversed adapted-perturbation (TRAP) optical focusing experiment with a schematic setup similar to Ref.[91] was carried out. A small chip (silicon semiconductor chip coated by gold; 100×150 μm^2) was tightly sandwiched between two microscope slides, forming an optical target attached to a translation platform. Two scattering layers were mounted before and after this optical target along the optical axis, serving as a scattering medium with a movable optical target inside. In experiment, the chip was first positioned outside the field of view, but later translated into the view, inducing perturbation to the optical fields recorded out of the scattering medium. With the TRAP procedure, a phase pattern that counteracts the turbidity of the scattering medium could be computed. When the phase pattern was displayed on the SLM during the playback process, diffused light could be refocused onto the chip, as seen in Fig. 2.6b, where the chip was clearly imaged with a PBR of 875. In comparison, when the SLM was

displayed with a random pattern, a seemingly random speckle image, as shown in Fig. 2.6a, was obtained as light was multiply scattered within the scattering medium.

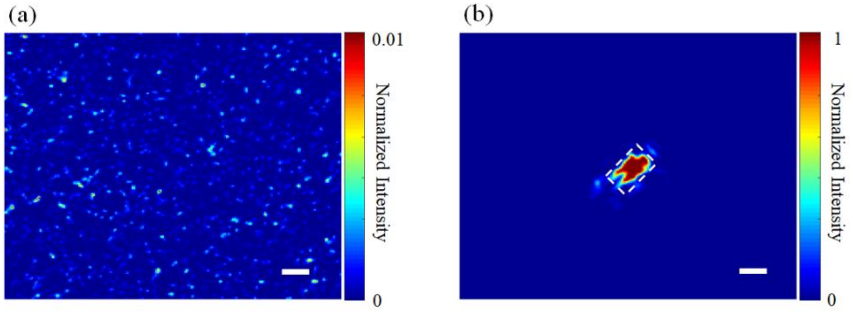

Fig. 2.6 (a) The image of a metal chip recorded by Camera 2 when a random pattern was displayed on the SLM; (b) The image of the same metal chip when TRAP optimization was performed. The dashed frame in (b) contours the position and the shape of the metal chip. The scale bars represent 100 μm.

The calibration of the curvature of the SLM is a critical step towards reliable and high quality digital optical phase conjugation. Therefore, two studies in the field have thus far dedicated to this topic. In the former [26], researchers used a Hadamard-pattern based iteration method to compensate for the curvature of the SLM and an extra auto-alignment method to fine tune the alignment between the SLM and the camera; a maximum PBR of 120,000 and a maximum efficiency of 66% were obtained. In the latter study[27], researchers used an orthonormal rectangular polynomials iteration method for SLM curvature compensation; a maximum PBR of 121,000 and a PBR improvement by a factor of 20 were obtained. No doubt both of the above-mentioned approaches can calibrate the curvature of the SLM effectively, especially when the number of independently controlled super-pixels for iteration on the SLM are large enough to represent as many major surface defects as possible. Noted that, however,

time consumed for iteration is directly proportional to the number of iteration (or the controlled units), while one single iteration takes about 1 second, mainly throttled by the slow refreshing rate of the SLM device. Therefore, one has to balance the calibration efficiency and the time consumption. It can be more demanding if the misalignment of the system or the disturbance to the system takes place during the experiment, which diminishes or even paralyzes the effect of the already-sought compensation. In this scenario, a new round of iterative compensation procedure is required. Therefore, in this section, a plain DOPC setup is introduced that allows for rapid, reliable and high-fidelity optical phase conjugation, enabling effective optical focusing through or within scattering media. The four-phase calibration method, albeit seemingly unappealing, is actually quite practical and convenient to be implemented, and it has not yet been reported in the context of digital optical phase conjugation. In experiment, the calibration process, taking up only ~0.8 seconds, is embedded into the three-stage DOPC procedure. By doing so, the system misalignment or disturbance emerging or evolving in experiment can be inherently calibrated and compensated, ensuring a more robust performance over time. Moreover, benefiting from the non-iterative operation, the proposed method can achieve a full-pixel (1920×1080) compensation for the SLM curvature. This advantage allows for higher PBR improvement ratio when the SLM curvature and reference beam imperfection is calibrated: the ratio is 50 times as seen in Fig.2.6, while it is only 2-5[26] and 20[27] times, respectively, in former studies. On the other hand, due to the lack of an EOM at hand, in this work, a phase rectification method, instead of the popularly used EOM-based full phase method, was used to retrieve the

signal beam hologram information. As known, EOM is widely used for phase shifting in many scenarios, especially in the in-line DOPC system. It is necessary to clarify that the aim of the proposed phase rectification method is not to challenge this situation, but rather a substitute approach when an EOM is inaccessible.

2.4 Conclusion

In this chapter, a plain self-embedded four-phase approach is developed to calibrate and compensate for the SLM surface curvature rapidly and effectively. A non-phase-shifting in-line holography approach is used to retrieve the phase information of the signal beam, generating effective optical focusing through or into scattering media. In experiment, the DOPC performance has been improved by 50 and 5 times, respectively, regarding the PBR and the spot size of the optical focus. Moreover, the focusing efficiency, as measured by the ratio between the experimental PBR to the theoretical one, is ~56.5%. The proposed setup provides a plain yet high-fidelity DOPC platform to enable effective optical focusing of diffused light. If further engineered, especially if the focusing time of the three-stage procedure can be reduced from the current several seconds down to the order of ms, it can potentially advance DOPC towards wide applications.

Chapter 3: Digital optical phase conjugation with magnetically controlled perturbation as internal guidestar for optical focusing inside scattering media

This chapter is reproduced with some adaptations from the manuscript "Zhipeng Yu, Jiangtao Huangfu, Fangyuan Zhao, Meiyun Xia, Xi Wu, Xufeng Niu, Deyu Li, Puxiang Lai, and D. Wang, "Time-reversed magnetically controlled perturbation (TRMCP) optical focusing inside scattering media", Scientific Reports 8, 2927 (2018)." D. Wang, J. Huangfu, and P. Lai conceived the idea. Z. Yu, D. Wang, J. Huangfu, and P. Lai designed the system. Z. Yu, F. Zhao, M. Xia, X. Wu, D. Li, and X. Niu ran the experiments. Z. Yu, D. Wang, and P. Lai prepared the manuscript. D. Wang and P. Lai co-supervised the project. All authors were involved in the analysis of the results and manuscript revision.

In Chapter 2, a plain yet high-fidelity DOPC platform is developed with embedded SLM curvature calibration and phase rectification. From there, DOPC's applications from two aspects (optical focusing inside scattering media and image edge enhancement through scattering media) will be demonstrated in this and next chapters. In this chapter, a magnetically controlled optical absorbing microsphere as the internal guidestar for the DOPC platform is proposed to obtain sharp optical focusing within scattering media through time-reversing the scattered light perturbed by the magnetic

microsphere. Since the object is magnetically controlled, dynamic optical focusing is allowed with a relatively large field-of-view by scanning the magnetic field externally. Moreover, the magnetic microsphere can be packaged with an organic membrane, using biological or chemical means to serve as a carrier. Therefore, the technique may find particular applications for enhanced targeted drug delivery, and imaging and photoablation of angiogenic vessels in tumors.

3.1 Introduction

In Chapter 1, various recent developments of DOPC on exploring internal guidestars to enable optical focusing inside a scattering medium were discussed, such as time-reversed ultrasonically encoded [92,93,96,105], time reversal of variance-encoded light[94], moving absorbers[91,106] and microbubble collapsing induced optical perturbations[107]. While promising, the existing internal guidestars are limited and not yet suitable for broad applications. For example, the efficiency of ultrasonic modulation is usually low[92,93,96,105], the ultrasonic guidestar-based approaches require physical contact (e.g. with water) for acoustic coupling and reduced loss at high acoustic frequencies, and the adaptive perturbation-based methods lack specific recognition or control[91,106]. To tackle the aforementioned limitations, in this chapter a new approach called time-reversed magnetically controlled perturbation (TRMCP) optical focusing is proposed, using magnetically controlled optical absorbing microspheres as internal guidestar for digital DOPC. It is shown that optical focusing within scattering media can be achieved by time-reversing the scattered light perturbed by the magnetic microsphere. Since the

object is accurately positioned and controlled by a magnetron device, dynamic optical focusing is allowed with a relatively large field-of-view by scanning the magnetic field externally. Such focusing may potentially benefit a wide range of biomedical applications in vessel-like aquatic environment, such as blood vessels and lymph vessels.

3.2 Methods

3.2.1 Experimental setup

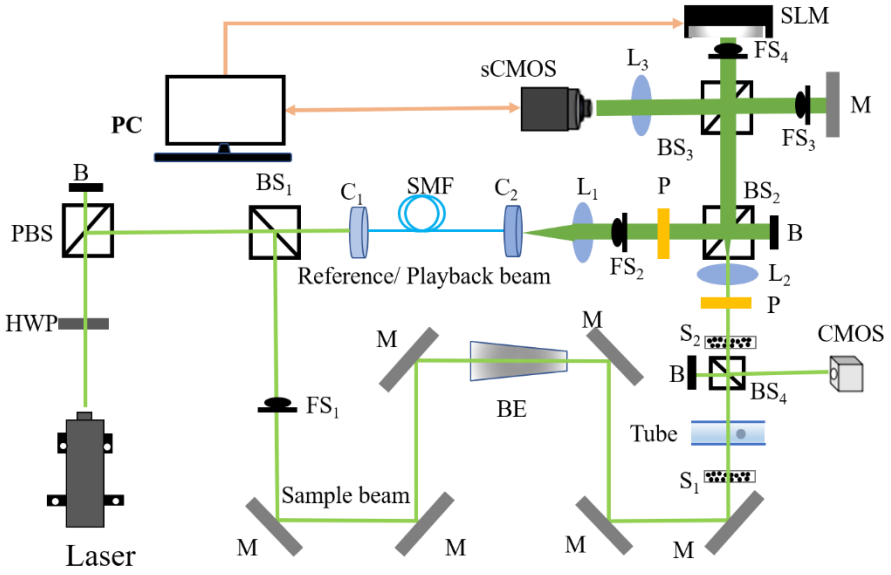

Fig. 3.1 Schematic of the system. B: beam dump; BE: beam expander; BS_1, BS_2: cube beam splitter; BS_3, BS_4: plate beam splitter; C_1, C_2: fiber port connector; HWP: half-wave plate; L_1, L_2: Plano-convex lens; L_3: camera lens; M: mirror; FS_1-FS_4: fast shutter; PBS: polarized beam splitter; P: polarizer; S_1, S_2: scattering layers; sCMOS: scientific CMOS camera; CMOS: CMOS camera; SMF: single mode fiber. The system is modified from the DOPC platform in Chapter 2.

The experimental setup of TRMCP is showed in Fig. 3.1(a), which is modified from the DOPC platform in Chapter 2. A 532nm continuous laser (EXLSR-532-200-CDRH, SPECTRA PHYSICS) is used as the light source, and its coherence length is 300 m. The laser output is split into two arms, a sample beam and a reference/playback beam, by a beam splitter (BS_1). In the hologram recording stage, the sample beam is expanded and illuminates the front surface of a scattering medium composed of two diffusive Scotch tapes (3M, ~60 μm thick) separated by 5.5 cm. Distorted sample light exiting the medium is collected and relayed to a scientific CMOS camera (sCMOS, pco.edge 5.5, PCO), where it interferes with the reference beam. The interfering patterns are transferred to the computer to compute the optical field, whose conjugation is then transferred to the SLM (PLUTO-VIS-056, HOLOEYE). In the hologram readout stage, the sample beam is blocked, and a playback beam illuminates the SLM, generating a phase conjugated copy of the original sample beam, which travels back to the scattering medium and converges to the position of incidence at the front surface of the first scattering layer (S_1), assuming there is no internal guidestar between the scattering layers. In additional to abovementioned components, a single-mode fiber (SMF) and lens L_1 are used to shape the reference beam (planar, 25.4 mm in diameter), lens L_2 is used to collect light exiting the scattering medium and adjust the speckle grain size in $sCMOS_1$, and lens L_3 is positioned in front of $sCMOS_1$ to image the surface of SLM or Mirror M. Four fast shutters ($FS_{1\text{-}4}$) are used to control the on and off of different optical beams. Between the two layers of diffusive tapes, a capillary tube is used to mimic a vessel. By changing the position of the magnetic microspheres within the capillary tube

under the magnetic field (described in next section), distribution of scattered light is tuned and recorded. Another camera (CMOS camera) positioned conjugated to the magnetic microsphere plane is used to observe the time-reversed sample beam. Lastly, it should be noted that with the 5.5 cm distance between the two Scotch tapes in the setup, few ballistic photons are collected and sent to the sCMOS camera for hologram recording[106].

3.2.2 Magnetic control system

A magnetic system is built to accurately control the positioning and movement of the magnetic microsphere within the tube, as shown in Fig. 3.2. A custom-designed electromagnet is mounted on a 2-D translation stage, and a sharp needle is adhered onto the upper surface of the magnet to generate a narrow magnetic field. The diameter of the needle tip is 0.05 mm, with a taper angle of 3.0 degree and a length of 29 mm. In experiment, a square capillary (inner cross-section 0.3×0.3 mm^2, wall thickness 0.1 mm) is used to mimic a vessel and placed 0.1 mm above the tip of needle. With this setup, a magnetic microsphere inside the tube can be attracted to the peak magnetic intensity position. Consequently, by scanning the translation stage along the X direction, accurate positioning, moving, as well as monitoring of the magnetic microsphere inside the tube is achieved. To avoid light being blocked by the magnetic needle, the magnetic needle is moved out of the field of view along the Z direction, when the light field information is under acquisition. It should be noted that during this moving out process, the magnetic field is varied, which may cause some microsphere perturbation (up to ~100

μm for the used ~200 μm diameter sized microsphere). To avoid this effect, during the needle moving in/out procedures, the electrical current through the electromagnet coil is shut off. As the needle and the electromagnet core are made of soft magnetic material, silicon steel, the remnant magnetism is negligible in current-free condition.

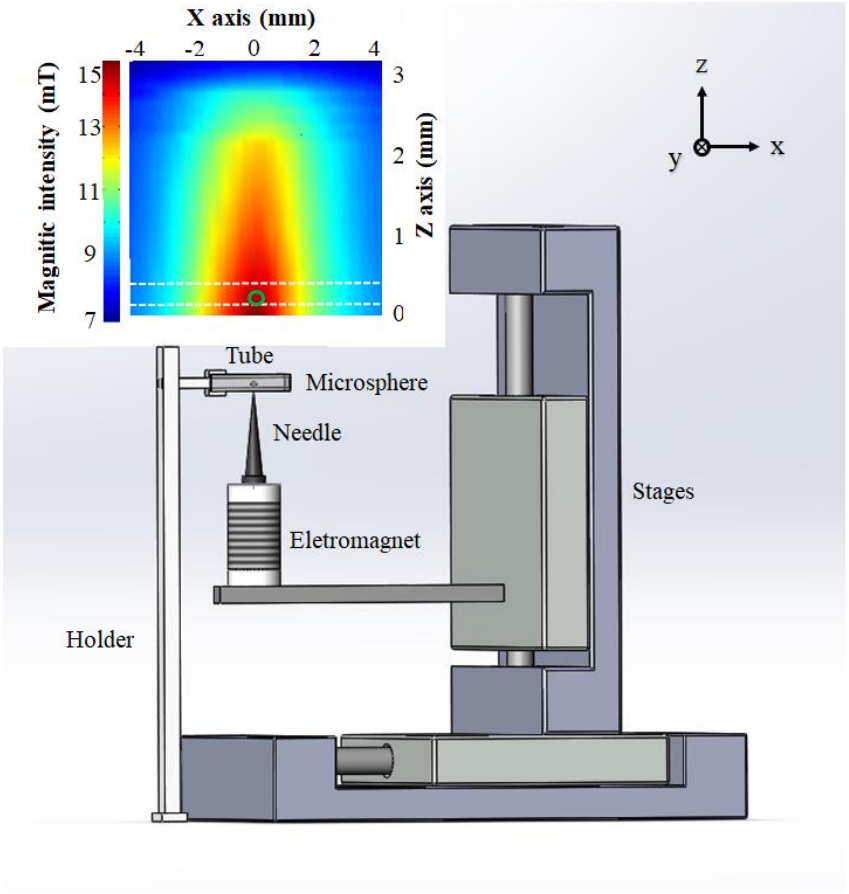

Fig. 3.2 Illustration of the magnetic control system. Inset: magnetic intensity distribution in the XZ plane above the needle.

Herein, a gauss meter (CH-3600, CH-HALL, China) is used to measure the magnetic intensity distribution in a vertical plane above the needle. The probe diameter of the gauss meter is 1 mm. As shown in Fig. 3.2, the magnetic intensity profile in the microsphere position seems not so sharp. It is largely caused by the relatively large size of the probe. The accuracy of repeated positioning of the magnetic control system is

also quantified. A microsphere with a diameter of 200 μm is controlled to move between two positions (with an inter-distance of 200 μm) for 10 times along the X direction. As a result, the positions produce a standard deviation of 9 μm and a maximum deviation of 19 μm. Thus, the open-loop positioning of the magnetic control system is sufficiently accurate, with a position standard deviation of within 5% of the object size.

3.2.3 Principle of TRMCP optical focusing

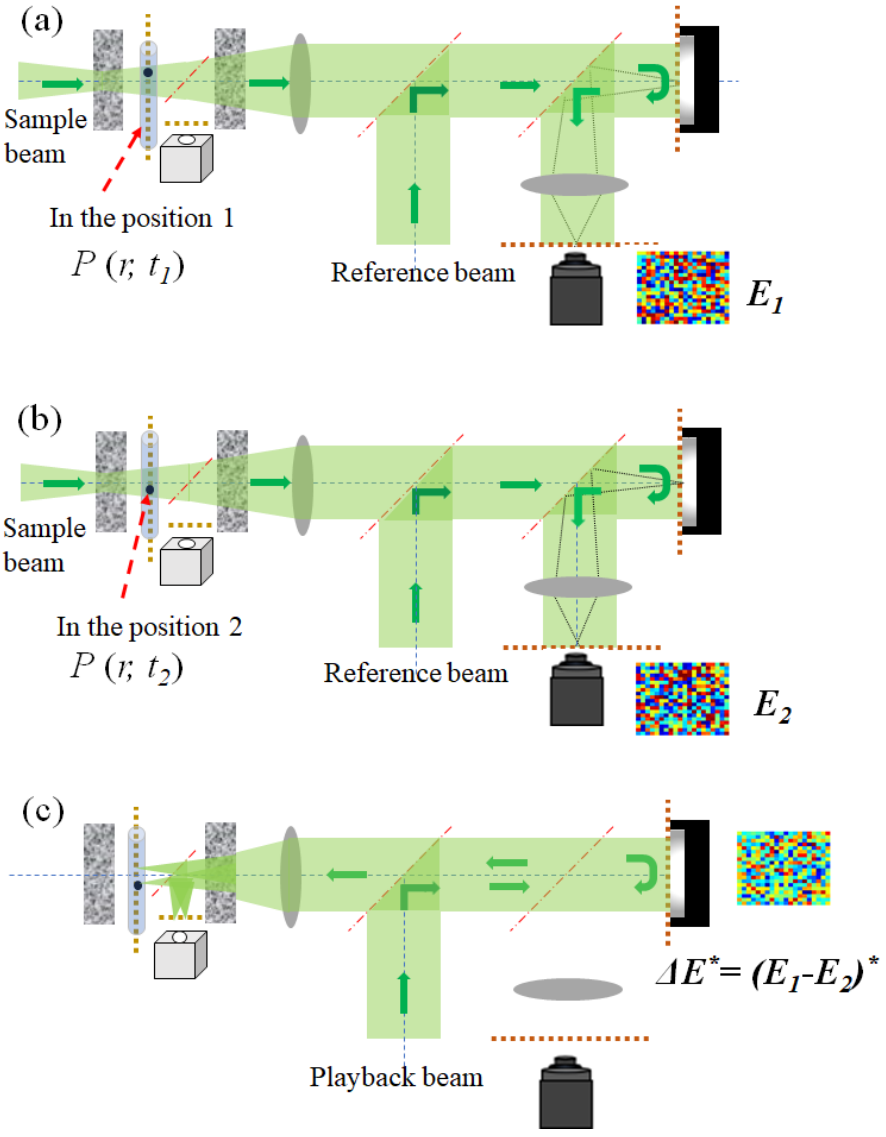

Fig. 3.3 Illustration of the two-stage TRMCP focusing procedure. (a-b) Hologram recording

stage: sample and reference beams interfere, with a camera to record the interference patterns when the magnetically controlled microsphere is at Location 1 and 2, respectively. The Light field difference *ΔE* is computed and stored. (C) Hologram playback stage: the playback beam (identical to the reference beam) is modulated by the SLM with a phase pattern *ΔE (the conjugate of *ΔE*), generating a phase conjugation copy of *ΔU*. The new light travels back to the scattering medium, albeit tortuously, and converges to the point of origin—the magnetically controlled moving microsphere.**

The focusing procedure is divided into two stages, i.e., phase recording and playback, respectively. In the phase recording stage, the magnetic microsphere (target absorption $P(r, t_i)$, i=1, 2) is first positioned at Location 1 (Fig. 3.3a). The resultant light fields are U_1 and E_1 at the microsphere plane and the camera plane, respectively. They are associated through the transmission matrix (T_1) of the system between the microsphere plane and the camera plane, thus $E_1 = T_1 \cdot U_1$. When the magnetic microsphere is moved to Location 2 (Fig. 3.3b), the light fields become U_2 and E_2, respectively, which are associated with $E_2 = T_2 \cdot U_2$. Assuming the system is linear and is sufficiently stable within the focusing procedure $T_1 = T_2 = T$, and the differences of two sets of light field $\Delta U = U_1 - U_2$ and $\Delta E = E_1 - E_2$ caused by the magnetic microsphere perturbation can be expressed by $\Delta E = T \cdot \Delta U$. In the playback stage (Fig. 3.3c), a phase pattern ΔE^* that is conjugated to ΔE is displayed on the SLM. The reference beam now serves as a playback beam that is modulated and reflected by the SLM surface. Due to the nature of phase conjugation, the reflection travels back to the scattering sample, although tortuously, and reaches the magnetic plane, resulting in an optical field of U_3

expressed by

$$U_3 = T^+(\Delta E)^* = T^+(T \cdot \Delta U)^* = (T^\dagger T \Delta U)^* \approx (\Delta U)^*, \quad (3.1)$$

where * denotes a complex conjugate. + and † denotes a transpose and a conjugate transpose. Approximately, $T^\dagger T = I$ (I is the identity matrix) assuming the system is time invariant during the process. As seen from the equation, U_3 is the conjugate to the light field difference at the microsphere plane, and hence converges to Positions 1 and 2. That is, the time-reversed light converges onto the magnetically guided moving microsphere.

3.2.4 Characterization of the DOPC system

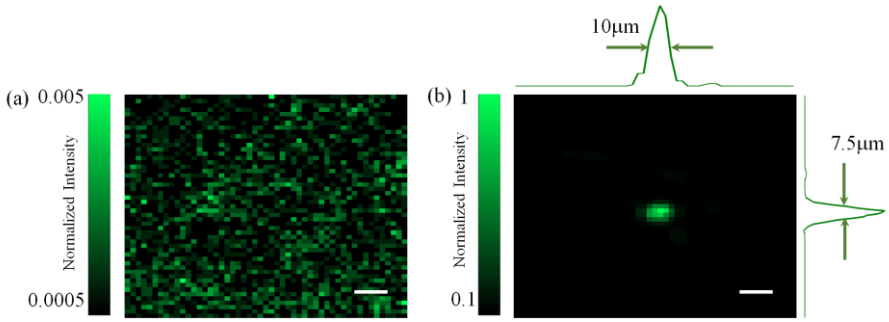

Fig. 3.4 (a) The optical pattern at the magnetic particle plane between two scattering layers recorded by the CMOS camera when the playback beam illuminates the SLM displayed with a random phase pattern. (b) When the SLM is loaded with the optimized phase pattern, a bright focus is formed with a PBR of 9000. The scalebar represnets 25μm.

To successfully perform TRMCP focusing, the quality of the DOPC system must be ensured. For example, the pixels between the sCMOS camera and the SLM must be precisely aligned and matched. In experiment, a specific pattern is displayed on the SLM, then the SLM and the sCMOS camera are aligned carefully to ensure the pixel

mismatch to be within one pixel. Moreover, a four-phase method is used to compensate for the SLM curvature-induced modulation error. As shown in Fig. 3.1, the SLM and the mirror M after FS_3 is adjusted to be perfectly perpendicular to the reference beam by using a retroflector, and the sCMOS camera is used to obtain the interference pattern of lights reflected by the SLM and mirror. The inter-distance between L_2 and S_2 (S_1 removed in advance) are adjusted carefully, as well as between L_2 and the sCMOS camera, so that a fully developed speckle patterns with appropriate speckle grain size are obtained in experiment. With the aforementioned optimization, an optical focus with a PBR up to 9,000 is obtained when the computed phase modulation pattern is displayed on the SLM (Fig. 3.4b). The FWHM of the focus is 10mm and 7.5mm, respectively, along the lateral directions. In contrast, a random speckle pattern is obtained when a uniform or random phase pattern is displayed on the SLM (Fig. 3.3a). theoretically the PBR is $\frac{\pi}{4}N$ for a phase-only SLM[111]. Here, N is the number of speckle grains (controlled modes) on the SLM plane. In the experiment, each speckle grain occupies about 6×6 pixels on the SLM. So, the theoretical PBR is ~45,000. Therefore, the focusing efficiency (η) defined by the ratio between the measured and theoretical PBR values is ~0.2. This is well below unity yet considered experimentally reasonable, if the influence due to the imperfection in the alignment, curvature compensation as well as system stability is taken into account.

3.3 Results and Discussion

With a characterized and optimized DOPC system, experiments are performed to demonstrate the feasibility and performance of TRMCP optical focusing. As shown in Fig. 3.5a, magnetic particles sized from 20-50 μm are enveloped with opaque levorotatory polylactic acid (PLLA) to form a magnetic-organic compound[119].

The procedure is as follows: First, the magnetic microspheres and PLLA solution are mixed sufficiently and then emulsified. Second, the mixtures are poured (at a suitable speed) into a polyving akohol solution that has been put on a rotating centrifuges stage in advance. As a result, the magnetic microspheres are enveloped with PLLA films, and compound microspheres with different sizes are formed. At last, microspheres of specific size are obtained through filtering the solution using appropriate meshes. A camera is used to record the resultant speckle pattern at the microsphere plane in advance, as shown in Fig. 3.5b and Fig. 3.5c. One speckle grain occupies ~25 pixels on the camera, and the camera pixel size is 2.5×2.5 μm^2. The diameter of the microsphere range is ~200 μm (5000 pixels), encompassing ~200 speckle grains.

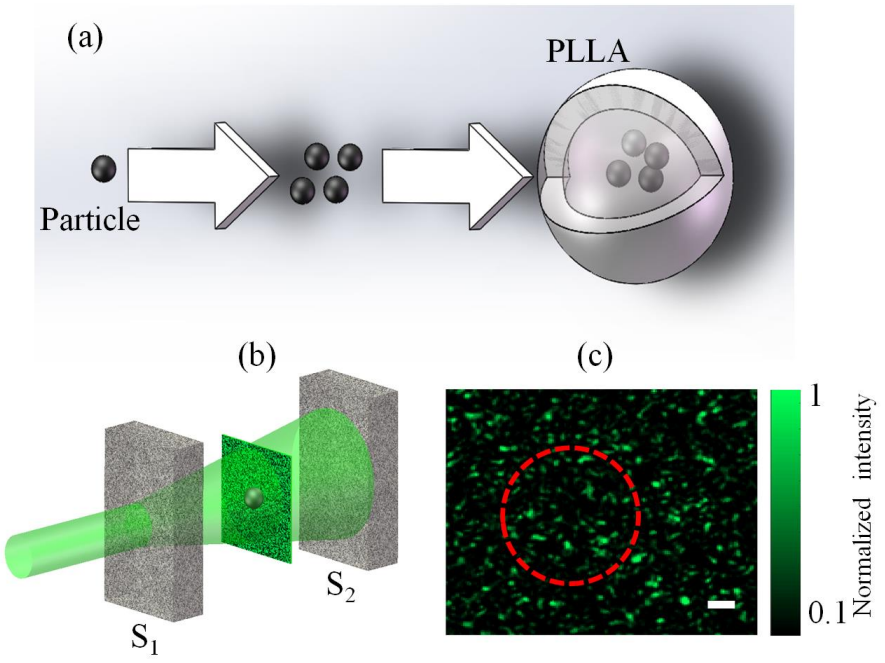

Fig. 3.5 (a) The enveloping process from magnetic microspheres into a microsphere. (b) The positioning of the magnetic microsphere with respect to the two scattering layers S_1 and S_2. (c) The resultant random speckle pattern when light illuminates the front surface of S_1; the magnetic microsphere is not seen, although a dashed circle is used to indicate its presence. The scalar bar represents 40 μm.

To mimic practical vessel application scenario, a square capillary with an inner cross-section of 0.30×0.30 mm^2 is used as the flowing channel for the magnetic microsphere. The distance between S_1 and S_2 is 5.5 cm, and the tube is positioned 3 cm away from S_2 (Fig. 3.1). In the experiment, the magnetic microsphere at first is away from the field of view, then is controlled to move step by step across the probed region. At each position, one hologram is recorded and the TRMCP is executed sequentially. Fig. 3.6a shows an example of focusing light to three adjacent positions by using TRMCP, where the magnetic microsphere is first placed at Location 1, then is controlled to move to Location 2, then to Location 3. Through light reflected by BS_4 in Fig. 3.1, the position

variation of the microsphere is also monitored in real time by a digital microscope, as shown in Figs. 3.6 b-d. As seen, the microscopic microsphere images are consistent with the three time-reversed optical focal spots in terms of position and dimension. It is evident that the phase conjugated beam has successfully converged back to the perturbation origins, which confirms the feasibility of TRMCP focusing. However, it should be noted that intensities of the multiple speckle grains within each focus are not evenly distributed, which is probably due to the imperfection in the sample beam illumination, the compensated phase pattern retrieval, and the system stability.

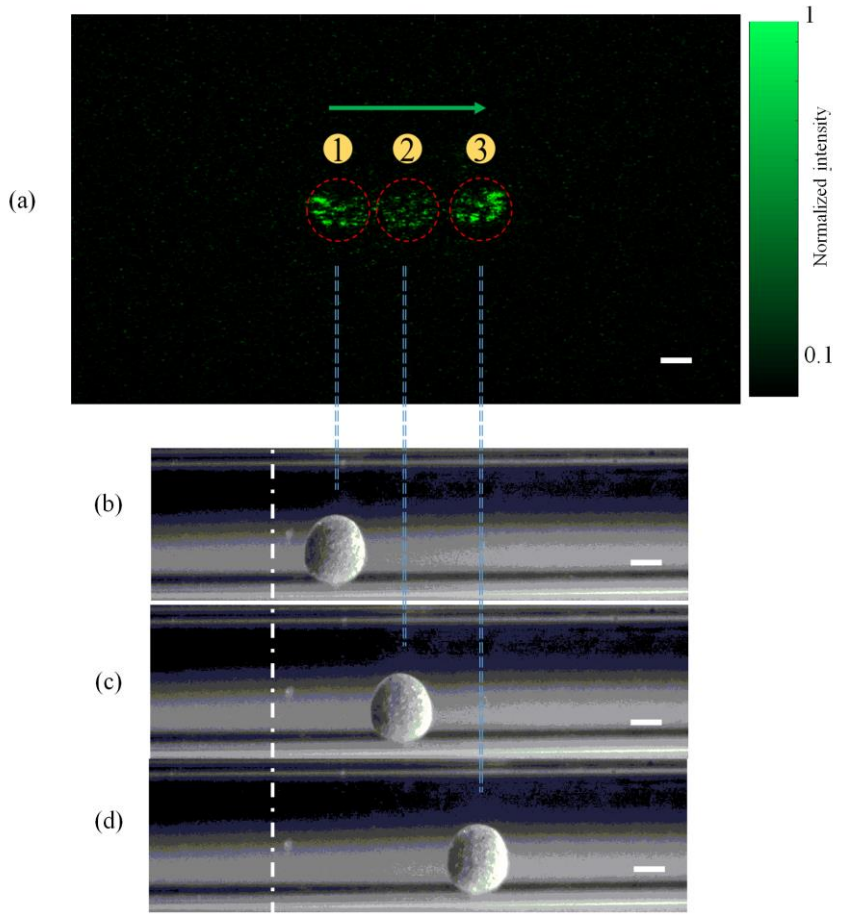

Fig. 3.6 (a) An illustration of three optical focal spots by using TRMCP, when the magnetic microsphere is externally controlled to move from Location 1 to Location 2, and from Location

2 to Location 3. The dashed circles contour the microsphere region. (b-d) White light images of the microspheres via side detection reveal the microsphere position variation and confirm the performance of TRMCP optical focusing, the scalar bars represent 100μm.

A whole focusing cycle, from the onset of recording the first hologram to the playback of the time-reversed light, took about 4 seconds, which is sufficiently fast for *ex vivo* and phantom-based studies. For *in vivo* applications, the speed of the focusing process must be considerably reduced since seconds is usually longer than the optical decorrelation time (on the order of milliseconds) associated with physiological motions such as blood flow and aspiration in living biological tissue. The slow process in the current system is largely due to the use of a personal computer as the controller for data transfer and processing, the lagged response of the SLM, the mechanical scanning of the magnetic field (~1 s), the move in/out of magnetic needle (~1s total), and the response time of electromagnet (0.4 s). To accelerate the focusing and make it suitable for living tissue applications where optical field decorrelates on the order of milliseconds due to physiological activities such as blood flow and respiration[40,120], further development will apply strategies to both the DOPC module and the magnetic controlling module. To build a faster DOPC system, a field programmable gate array (FPGA) combining with DMD, a micro-electro-mechanical system (MEMS)-based SLM or a ferroelectric liquid crystal-based SLM will be considered[65,99,100].

Three more aspects also need to be addressed. First, the PBR of the optical focusing with magnetic microsphere in experiment was 32, while theoretically it can reach 112.5

according to $PBR_{TRMCP} = \frac{\pi}{4}\frac{N}{K}$ for a phase-only SLM[91], where K is the number of the speckle grain on the microsphere plane of the sample beam. The above estimation contains a π/4 factor because the SLM used in experiment is a phase-only modulator. The efficiency, defined by the ratio between the measured and theoretical PBRs is only 28.4%, possibly due to factors such as (1) the boundary or mismatch between the tube and the phantom medium, as well as the rectangular shape of the tube (that introduce extra deflection to the sample beam; (2) the thickness of the tube, and (3) the alignment imperfection of the DOPC system. Second, in experiment the magnetic microsphere was only 0.1 mm above the tip, which is a close distance to ensure the movement resolution of the particle. To translate the system towards real applications, a customized high-speed mechanical scanning system and quickly responding electromagnet will be applied. Last but not the least, the medium flow within the tube may induce position variation to the magnetic microsphere, especially when the magnetic binding force is not sufficiently large. Such influence cannot be ignored in applications in vessel-like environment. A fast system discussed above can help to overcome the challenge, and furtherly, one may be able to temporarily block or slow down the flow (e.g. blood flow) by using clamps or rubber bands[92,121]. With the aforementioned improvement, TRMCP can potentially be useful for many applications in vessel-like aquatic environment, such as lymph vessels and blood vessels.

3.4 Conclusion

Optical focusing beyond the diffusion limit inside biological tissue has been long

desired yet considered challenging. Aiming towards this goal, a magnetically controlled microsphere movement that generates optical perturbation as internal guidestar for optical phase conjugation is proposed. The feasibility of this approach, referred to as time-reversed magnetically controlled perturbation (TRMCP) optical focusing, has been demonstrated experimentally herein and recently by Ruan *et al*. in an another independent study[122]. Compared to previous schemes in the field, this new approach has advantages in the playback efficiency and the guidestar scanning controllability, making it a promising solution to focus light into vessel-like medium at depths in tissue. Moreover, the magnetic microsphere can be packaged with an organic membrane, using biological or chemical means, and serve as a carrier. Therefore, this approach, once further engineered, may potentially find some applications for precisely targeted drug delivery, tumor angiogenic vessel imaging and photoablation.

Chapter 4: Digital optical phase conjugation-enabled edge enhancement through scattering media

This chapter is reproduced with some adaptations from the manuscript "Zihao Li, Zhipeng Yu, Hui Hui, Huanhao Li, Tianting Zhong, Honglin Liu, and Puxiang Lai, "Edge enhancement through scattering media enabled by optical wavefront shaping", Photonics Research 8(6), 954 (2020)". The contributions of authors are as follows: Z. Yu and Puxiang Lai conceived the idea. Z. Yu designed the system. Z. Li., Zhipeng Yu and H. Hui ran the experiments. Z. Li, Z. Yu and P. Lai prepared the manuscript. All authors were involved in the analysis of the results and manuscript revision.

In Chapter 3, one application from the perspective of optical focusing inside scattering media by combining DOPC system with a magnetic control module is demonstrated. In that scheme, the wavefront modulator, as a whole, only contributes to one output channel, which indicates a simple mapping relationship between the input and output. In this chapter, the application of DOPC for image edge enhancement through scattering media with a relatively more complex mapping relationship (a larger information capacity) will be demonstrated, in which the wavefront modulator contributes to all output channels. The implementation of DOPC to achieve efficient edge enhancement through scattering media is completed by a two-step operation. The

first step is to acquire a hologram after the scattering medium, where information of the edge region is accurately encoded, while that of non-edge region is intentionally encoded with inadequate accuracy. The second step is to decode the edge information by time-reversing the scattered light.

4.1 Introduction

Edge enhancement is uniquely important as perception of edge is a key factor for human visual system to identify or comprehend the contents of an image. It has vital roles in broad applications, such as increasing discrimination capacity in pattern recognition [123], detecting dislocation of crystal in biological cells [124], identifying lesion boundaries of cancer [125-128]. The realization of edge enhancement can be traced back to Zernike's seminal work [129], where phase or intensity gradient of an object is enhanced for conspicuity strengthening and tiny-feature detection. Nowadays, edge enhancement can be accomplished digitally through signal processing methods, such as spatial differentiation [130], wavelet transform [131], and Hilbert transform [132], or through physical settings. One well-known example is spiral phase contrast (SPC) imaging, where a spiral phase plate with a topological charge $l = 1$ is placed in the Fourier plane of a 4f system [133-135]. Due to the peculiar symmetry of spiral phase, gradients of phase and intensity profile can be isotropically enhanced. SPC method was later extended for microscopy to make image brightness and contrast be significantly better than conventional versions [136]. Another strategy is to employ photorefractive effect to highlight the edge information of an intensity pattern [137-139]. Responding to

interferogram, photorefractive materials, governed by the four-wave-mixing mechanism [137], form volumetric optical grating with different local diffraction efficiencies. Manipulating such grating may maximize the diffraction efficiency for edges only while minimize that for other parts; consequentially boundaries of the pattern are enhanced [137]. In addition, some physical filters, such as Laguerre–Gaussian spatial filter [140] and Airy spiral phase filter [141], are also developed to achieve high contrast edge enhancement.

Whilst promising, all filters mentioned above, no matter digital or physical, can only perform edge detection in free space or process signals obtained with ballistic or quasi-ballistic light. These approaches are not able or have not been verified to be compatible with strong scattering media (e.g., ~1 mm beneath human skin [43]), when photons are multiply scattered and optical information is completely disordered [38]. Therefore, existing edge enhancement methods encounter the same trade-off between penetration depth and resolution as all other biomedical optical techniques [142]. High-resolution edge information processing and retrieval at depths in scattering media has been desired in many optical applications yet remains unexplored.

This study aims to tackle this challenge from the perspective of optical wavefront engineering, a relatively new field conceived to manipulate scattered light beyond the diffusion limit [55,58,92,109,143]. As talked in Chapter 1, optical phase conjugation [55-57,92] is an example of wavefront engineering that exploits the bilateral nature of light trajectory

to “time-reverse” scattered light [144]. The execution of optical phase conjugation requires an analog [55,145] or digital [56,57,146,147] phase conjugation mirror that firstly holographically records the phase profile of scattered light and secondly projects its phase-conjugated copy back to the medium. As a result, intensity profile of the original incident light field before being scattered can be reconstructed. The whole procedure can be accomplished with two or three steps [147], achieving light manipulation through turbidity as rapidly as a few milliseconds [99,100]. While related, such a capability thus far has not yet been extended for edge enhancement through scattering media. In this study, we take inspiration from the classic photorefractive approach for edge enhancement in free space [137], and develop a digital optical phase conjugation setup to achieve robust and tunable time-reversed speckle suppression and edge enhancement through thick scattering media by a two-step procedure. First, a hologram that accurately encodes the information of edge only is recorded. Secondly, the edge pattern is selectively decoded by phase conjugating the scattered light. The proposed method is demonstrated experimentally with scalable edge enhancement performance out of seemingly random speckle patterns. Although a lot need to be furthered, this work potentially can be of instructive significance to the processing, comprehension, and analysis of optical images with the presence of scattering.

4.2 Methods

4.2.1 Experimental setup

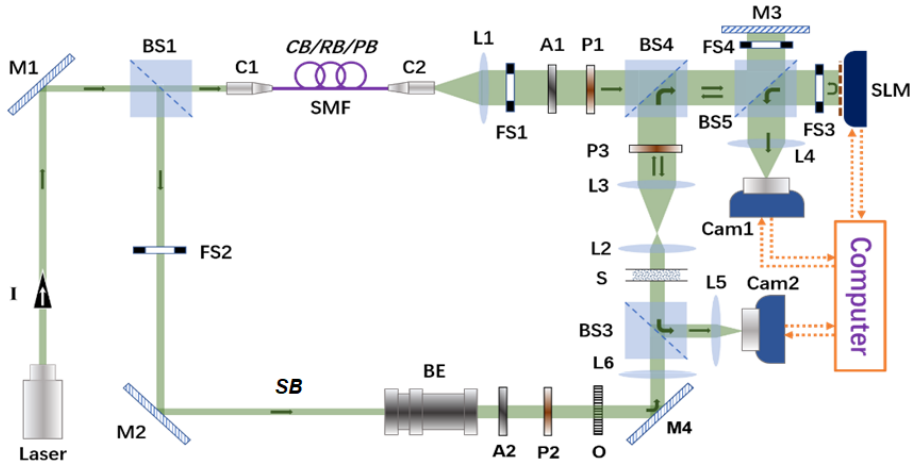

Fig. 4.1 System setup of DOPC. $A_{1\text{-}2}$: Neutral-density attenuator; BE: Collimated beam expander; $BS_{1\text{-}5}$: Beam splitter cube; $C_{1\text{-}2}$: Optical fiber collimator; Cam_1: Scientific complementary metal–oxide–semiconductor (sCMOS) camera; Cam_2: CMOS camera; $FS_{1\text{-}4}$: Fast shutter; I: Isolator; $L_{1\text{-}3,\,5,\,6}$: Best-form lens; L_4: Camera lens; Laser: CW laser, λ = 532 nm;. $M_{1\text{-}4}$: Mirror; O: Object, a 1951 USAF resolution test chart; $P_{1\text{-}3}$: Linear polarizer; S: Scattering medium; SLM: Phase-only spatial light modulator; SMF: Single-mode optical fiber; CB/RB/PB: Calibration/Reference/ Playback beam; SB: sample beam. Red dash line indicates the module of digital phase conjugation mirror (PCM). The system is modified from the DOPC platform in Chapter 2.

The configuration of DOPC system is presented in Fig. 4.1, which is modified from the DOPC system in Chapter 2. A CW laser source (EXLSR-532–200-CDRH, SPECTRA PHYSICS, coherence length = 300 m) emits a laser beam (λ = 532 nm) which is split by a beam splitter cube (BS_1) into two arms. One is sample beam, and the other is multi-

functional beam (calibration/reference/playback beam). The sample beam is expanded by a collimated beam expander and its intensity profile is shaped by a 1951 USAF resolution test chart (Edmund Optics Inc.). The image of the resolution test chart is relayed onto the interior surface of a diffuser (600 grit polished, Thorlabs Inc) by L_6. On the other side, the multi-functional beam is spatially shaped by a single-mode fiber (HP-532, Thorlabs, 1 meter long) to mimic a quasi-ideal point source at the exit of the collimator (C_2). The beam is expanded by a best-form lens (L_1) before entering the digital PCM module. At the beam splitter cube (BS_4), the sample beam and the multipurpose beam merge and are relayed together to the digital PCM, which is configurated by the combination of a scientific CMOS camera (sCMOS, pco.edge 5.5, PCO, pixel size: 6.5×6.5 μm) and a phase-only SLM (PLUTO-VIS-056, HOLOEYE). The SLM and the sCMOS camera are pixel-to-pixel conjugated to each other, with a misalignment error less than one pixel. The diffused light pattern right after the diffuser is imaged on the plane of SLM through a 4*f* system configured by L_2 and L_3, where the diffuser and the plane of SLM is spatially quasi-conjugated with each other. The digital PCM has two main purposes, hologram recording and playback, which are respectively accomplished by the sCMOS camera and the phase-only SLM. To observe the playback wavefront, another CMOS camera (Cam_2, pixel size: 2.5×2.5 μm) and L_5 are employed to image the reconstructed intensity distribution of the playback beam after transmitting through the turbid sample. Polarizations and intensities of the sample beam and the multipurpose beam are adjusted by two linear polarizers (P_1 and P_2) and neutral-density attenuators (A_1 and A_2), respectively. Four fast shutters ($FS_{1\text{-}4}$) are equipped to control

the ON or OFF state of light beams. Detailed procedures of DOPC operation can be referred to [146,147].

4.2.2 Phase retrieval accuracy influenced by the beam intensity ratio

The edge enhancement effect is achieved by adjusting the intensity ratio between the reference beam and the sample beam. The phase retrieval accuracy is influenced by this ratio because of the finite bit depth of the camera used in DOPC system. Here how the intensity ratio of two interfering optical beams affects the accuracy of retrieved phase difference between them is discussed. As shown in Fig. 4.2a, green vector (E_0) represents the electric field of one optical beam, and blue (E_1) and red (E_2) vectors stand for the electric field of other beams, with distinct magnitudes in two cases (equal and unequal cases). The sample beam (E_{sample}) and reference beam (E_{ref}) (described in the manuscript) can correspond to any one of these three vectors depending on their values. In the first case, E_1 has the same magnitude to that of E_0, suggesting that the intensities of these two beams (I_a and I_b) are the same, i.e. $r = \frac{I_a}{I_b} = \frac{|E_0|}{|E_1|} = 1$; in the second case, E_2 has smaller magnitude than that of E_1.The resultant optical field can be obtained by vector addition. Within a given intensity resolution interval of digital camera, all intensity values within this interval yield the same digital output at the photosensor. In other word, the digital records of interferograms that lie in a single intensity resolution interval are identical. Therefore, phase difference between two optical beams cannot be resolved, unless the intensity of interferogram differs by at least one intensity resolution interval of the camera. For a given intensity resolution

interval, i.e. $\left[I_{low}, I_{high}\right]$, whose lower and upper intensity limit are corresponding to two electric field vectors that have small difference in magnitude, i.e. E_{low} and E_{high}, where $\left|E_{low}\right|^2 = 2I_{low}/c\varepsilon_0$ and $\left|E_{high}\right|^2 = 2I_{high}/c\varepsilon_0$ (c: the speed of light; ε_0: permittivity of free space). E_{low} and E_{high} for the abovementioned two different cases are accordingly signified by the two pairs of magenta and yellow vectors ($\left|E_{low}\right|\hat{e}_1$ & $\left|E_{high}\right|\hat{e}_1^{'}$ and $\left|E_{low}\right|\hat{e}_2$ & $\left|E_{high}\right|\hat{e}_2^{'}$, where $\hat{e}_1, \hat{e}_1^{'}, \hat{e}_2$, and $\hat{e}_2^{'}$ are unit vectors). For the first case ($r = 1$), i.e. the upper semi-circle in Fig. 4.2a, $E_1^{'}$ will yield the same digital record of the interferogram as E_1, since the their resultant intensity values lie in a single intensity resolution interval, $\left[I_{low}, I_{high}\right]$. Therefore, the smallest resolvable phase change (precision) by the interferogram is $\Delta\emptyset_1$. For the second case ($r > 1$), i.e. the lower semi-circle in Fig. 4.2a, $E_2^{'}$ will produce the same digital record of the interferogram as that of E_2, being similar to the first case. As a result, the smallest resolvable phase range (precision) by the interferogram for the second case is $\Delta\phi_2$. As seen qualitatively, $\Delta\phi_2 > \Delta\phi_1$, which means the resolvability (precision) of phase change by interferogram is under-optimized when one beam is more intense than the other. Moreover, it can be inferred that when $r >> 1$, i.e. one light beam is far more intensive than the other, the resolvability (precision) of the phase change by the interferogram becomes even worse.

In experiment, a four-step phase-shift method [37] is applied to retrieve the phase difference φ between the two optical beams. The interferograms projected to Cam_1 (as in Fig. 4.1) can be written as

$$I_{h,i} = I_{a,i} + I_{b,i} + 2\cos(\varphi + i * \pi / 2) * \sqrt{I_{a,i} I_{b,i}}, i = 0,1,2,3. \quad (4.1)$$

However, all these four digital records of interferogram suffer from the "round-off" effect due to the nature of digital cameras, as discussed above. When one light beam has larger intensity than the other, the "round-off" effect compromises the fidelity of phase retrieval. The exact digital records of four interferograms, denoted by $[I_h]_i$ $(i = 0,1,2,3)$, are utilized to calculate phase value through

$$\varphi_{cal} = \arg\{([I_h]_0 - [I_h]_2) + j * ([I_h]_1 - [I_h]_3)\}, \quad (4.2)$$

where arg { } denotes taking the phase angle of a complex number. Based on equations. 4.1 and 4.2, the phase retrieval by the four-step phase-shift approach under the "round-off" effect is simulated, as shown in Fig. 4.2b. As seen, $r = 1$ gives the best approximation to the true value; when r increases, however, the calculated phase values deviate more from the true curve. The phase value even cannot be retrieved when r approaches to a large value, say $r = 50$, which may lead to a completely invalid measurement over the entire range of phase (0 to 2π). In brief summary, the retrieved phase profile is most accurate when the two beams of interference are equally intense *in situ*, and the accuracy is reduced with increased imbalance in beam ratio.

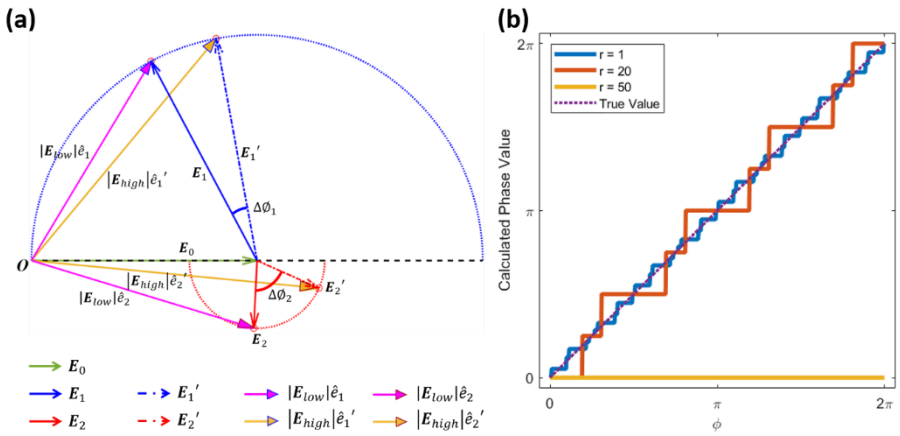

Fig. 4.2 (a) Schematic diagram illustrating how intensity ratio between two optical beams

affects the resolvability of phase by interferogram. Different types of vector represent electric field of different beams, as presented by the legend. $\Delta\phi_{1,2}$: The smallest resolvable interval of phase. (b) Retrieved phase value by the four-step phase-shift method, under the "round-off" effect of digital camera. r is the intensity ratio between the two optical beams that are interfering, i.e., $r = \frac{I_a}{I_b}$.

4.2.3 Principles of DOPC-based edge enhancement through scattering media

A former study has demonstrated how edges of a binary pattern can be enhanced in free space via photorefractive effect with a piece of $BaTiO_3$ photorefractive crystal [137]. The method proposed in this work is actually a digital analogue of the aforementioned photorefractive edge enhancer. Functions of the photorefractive crystal are provided by a digital PCM, a spatially conjugated camera-SLM module, as enclosed by the red dash line in Fig. 4.1. On one hand, holographic information is recorded digitally using a digital camera (Cam_1, Fig. 4.1); on the other hand, a SLM is able to create variable phase profiles, mimicking the effect of grating with variable diffraction efficiency in the crystal.

Starting with hologram recording, the working principles of DOPC-based edge enhancement can be explained as below. The hologram recorded by Cam_1 can be written as

$$I_h = I_{ref} + I_{sample} + 2\cos(\varphi)\sqrt{I_{ref} + I_{sample}}\,, \tag{4.3}$$

where φ denote the intensity of hologram, the reference beam, and the sample beam, respectively; is the phase difference between the reference beam and the sample beam. The local modulation efficiency ($M.E.$) of PCM, determined by contrast of the hologram recorded by Cam_1, can be expressed as

$$M.E. = \frac{I_h}{I_{ref} + I_{sample}} = 1 + MD * \cos(\varphi) . \tag{4.4}$$

It can be seen that local $M.E.$ of PCM is dominated by the modulation depth ($MD = \frac{2\sqrt{I_{ref} * I_{sample}}}{I_{ref} + I_{sample}}$) [137]. This term can be expressed as a function of the intensity ratio of the sample and reference beams, i.e. $r = \frac{I_{sample}}{I_{ref}}$. So that, $MD = \frac{2\sqrt{r}}{1+r}$. As a result, $M.E.$ can be written as $M.E. = 1 + MD(r) * \cos(\varphi)$. Considering the one-dimensional situation as following without scattering media

$$I_{ref}(x) = a\left(\text{for all } x\right); I_{sample}(x) = \begin{cases} 0 & x \le -m/2 \\ b & -m/2 < x < m/2 \\ 0 & x \ge m/2 \end{cases}, \tag{4.5}$$

where a, b and m are three finite constants. It represents a simple case of hologram written to Cam_1, where the reference beam is of uniform intensity while the sample beam is of a binary intensity profile, i.e. a box function with a width of m, symmetrical with respect to the origin. But there is an extreme condition for this situation, that is the intensity of the sample beam is considerably larger than that of the reference beam i.e. $a << b$. For the dark region of the sample beam ($x < -\frac{m}{2}$ or $x > \frac{m}{2}$), $r = 0$, which leads to $MD(r) = 0$. For the bright region of sample beam ($-\frac{m}{2} < x < \frac{m}{2}$), $r = \frac{b}{a}$, being considerably large, which also yields $MD(r) \approx 0$. The

situation is different, however, for the edges ($x = -\frac{m}{2}$ or $x = \frac{m}{2}$). It is considered to exist a transition status where $I_{ref} \approx I_{sample}$, making the *in situ* $MD(r)$ maximum that equals to unity [137].

In the existence of the scattering media, the scattering light field recorded by Cam_1 can be expressed by:

$$E_{out} = TE_{in}, \tag{4.6}$$

where E_{in} is the light field of sample beam before the scattering medium, and T is the transmission matrix of the scattering medium. Due to the scattering, the spatial pattern gets completely chaotic and, as a result, edge profile cannot be seen in the disordered optical field. Specifically, the spatial pattern evolves as random speckle pattern when light propagates through the scattering medium in the hologram recording stage. Thus, the original spatial information is encoded in the recorded random speckle pattern; the recorded speckle pattern carries information of the original incident spatial pattern and the scattering medium. Therefore, signal input to the PCM is the fused information of TE_{in} . Due to the phase-conjugated nature, the PCM turns the input into its phase-conjugated copy, $\left[TE_{in}\right]^*$ .In the hologram playback stage, the light filed (E_{PB}) out of the scattering medium is recorded by Cam_2, which can be written as

$$E_{PB} = (T)^t \left[TE_{in}\right]^* = \left[T^\dagger TE_{in}\right]^*, \tag{4.7}$$

where * denotes complex conjugate while ^{t} and $\dagger$ respectively signify transpose and conjugate transpose.

A further justification why the time reversal identity of DOPC is able to overcome the scattering and achieve edge enhancement simultaneously is briefed below. In the phase recording stage, Cam_1 records an interferogram formed by the reference beam (E_{ref}) and the scattered sample beam (TE_{in}). After the scattering medium, the sample beam is scrambled. In the playback section, the output light field ($T^{\dagger}TE_{in}$) from the scattering medium appears even more scrambled. But, within a time-invariant system, one can assume that $T^{\dagger}T = I$, where I denotes an identity matrix. That is, the output light is exactly conjugated to the sample beam. Therefore, the time-reversal playback essentially decodes the original pattern from a seemingly random speckle pattern by reciprocating the transmission matrix, enabling scattering suppression at the front side of the scattering medium.

For DOPC systems, a Camera-SLM module is employed to record the sample-reference interference pattern and retrieve a phase profile to mimic the effect of grating in analogue OPC. Thus, the precision of the retrieved phase (to be loaded on the SLM) matters. In the system, the primary phase retrieval precision is determined by the smallest bit depth of the digital devices (Cam_1: 16 bits; SLM: 8 bits) Through simulation (please refer to section 4.2.2), it is found that the calculated phase is most accurate when the two beams of interference are equally intense, and the accuracy is reduced with increased imbalance in beam ratio (Fig. 4.2). Therefore, in the system, when the beam ratio r=1, the whole object can be recovered with fair fidelity due to the minimum phase error. With increased beam ratio *r*, for non-edge regions the

phase retrieval accuracy drops due to imbalance of interfering beam ratio. But for edges, the precision of calculated phase remains optimum due the existence of transition status where $I_{ref} \approx I_{sample}$. Under this condition ($I_{obj} >> I_{ref}$), when the SLM is illuminated by the reference beam in the playback stage, the generated conjugated light corresponding to the non-edge regions may deviate from its ideal optical paths. As a result, the non-edge regions are harder to be recovered; more and more photons contribute to the background noise when they propagate through the scattering medium. In comparison, the edge areas are reinforced from the background.

4.2.4 Quantification of edge enhancement effect

For a characteristic unenhanced edge (Fig. 4.3a) in an intensity pattern, it can be divided into three portions, ground level (G), brink (B), and upper level (U). In the experiment, the lengths of G and U are both set to be 30 pixels. For an enhanced edge (Fig. 4.3b), two additional parameters are defined, the summit (S) (maximum pixel intensity) and the valley (V) (minimum pixel intensity) in the regime of brink. To quantify the absolute edge enhancement effect, the concept of edge enhancement-index (*EI*) is introduced [148,149]: $EI = \frac{(S-V)/(S+V)}{(\mu_U - \mu_G)/(\mu_U + \mu_G)}$, where μ_U and μ_G are the mean of intensity values of U and G, respectively. For a non-enhanced typical edge, $\mu_U \approx S$, $\mu_G \approx V$ and therefore the edge enhancement index $EI = 1$. Larger *EI* indicates greater absolute edge enhancement effect. However, only EI is not sufficient for quantifying the visual conspicuity of the edge, as the noise level also influences the visual effect (Fig. 4.3c). Thus, the concept of edge enhancement-to-

noise ratio (ENR) is also defined to quantify the edge enhancement effect relative to the noise level [148]: $ENR = \frac{S - V}{\sqrt{\sigma_U^2 + \sigma_G^2}}$, where σ_U and σ_G are the standard deviation of intensity values of U and G, respectively. Less noise in U and G and greater difference in S and V will lead to larger value of ENR, indicating better visual edge enhancement effect relative to the noise level.

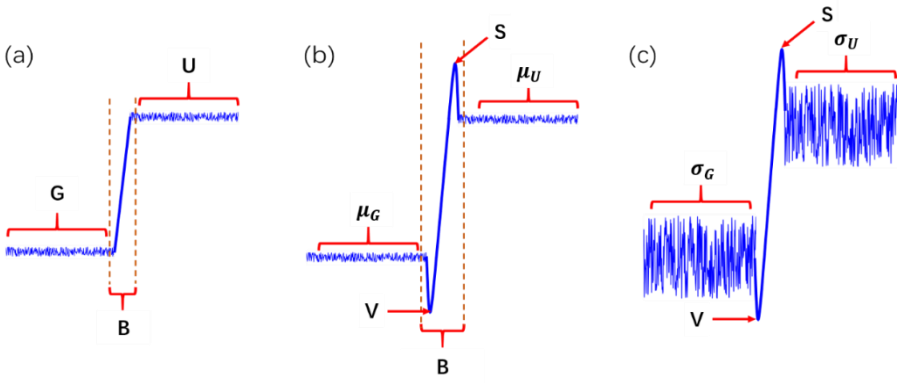

Fig. 4.3 Anatomy and metrics of an edge. (a) A regular unenhanced edge can be divided into three portions, including ground level (G), brink (B), and upper level (U). The lengths of G and U occupy 30 pixels in the experiment. (b) For an enhanced edge, the maximum and minimum pixel intensity of the portion B are termed as summit (S) and valley (V). To quantify the absolute edge enhancement effect, the concept of edge enhancement-index $EI = \frac{(S - V)/(S + V)}{(\mu_U - \mu_G)/(\mu_U + \mu_G)}$ is introduced, where μ_U and μ_G are mean of intensity values of U and G, respectively. (c) The noise level of an edge influences the visual enhancement effect and thus the concept of edge enhancement-to-noise ratio $ENR = \frac{S - V}{\sqrt{\sigma_U^2 + \sigma_G^2}}$ is defined, where σ_U and σ_G are standard deviation of the intensity values of U and G, respectively.

4.3 Results and Discussion

With a fine-tuned DOPC system, experiments are conducted to enhance edge of an intensity pattern through strong scattering media. Transmitting through the resolution test chart, the intensity profile of the sample beam is shaped into a pattern “0”, carrying the spatial information. This original pattern of interest is recorded by Cam_1, as shown in Fig. 4.4(a). Three horizontal dashed primitive lines with the length of 280 pixels are created in the Fig. 4.4(a) and the line charts (b)-(d) correspondingly show the horizontal intensity distributions along these lines. A and B denote the inner and outer rim of the pattern “0”, respectively. For edge B, the mean *EI* and *ENR* are calculated as 0.91 and 42.77, respectively. Then, a highly scattering medium (600-grit ground glass diffuser) is positioned into the DOPC system. As shown in Fig. 4.4(e), captured by Cam_1, the intensity profile of the sample beam becomes a random speckle pattern right after penetrating through the ground glass and no edge profile can be found, indicating that the spatial information of object was completely disordered due to scattering.

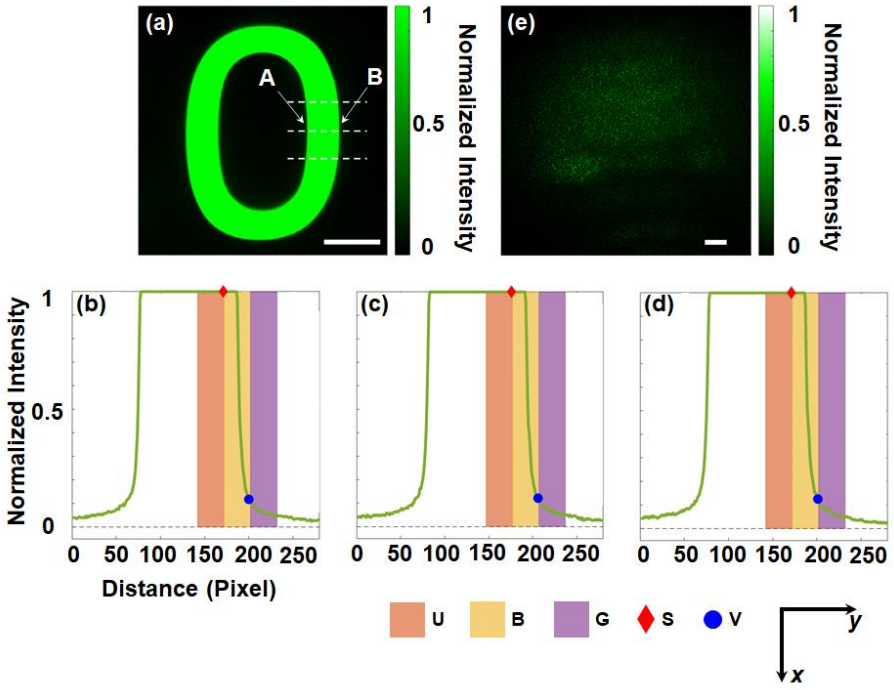

Fig. 4.4 Intensity profile of the sample beam before and after transmitting through the scattering medium. (a): Intensity profile of the incident sample beam, a quasi-binary pattern of number "0", shaped by the resolution test chart. Three horizontal white dashed primitive lines (1-3) with the length of 280 pixels are created. The intensity distribution along the line 1-3 are respectively shown in (b)-(d). A and B denote the inner and outer rim of the pattern "0", respectively. For edge B, the mean *EI* and *ENR* are calculated as 0.91 and 42.77, correspondingly. U: Upper level; B: Brink; G: Ground level; S: Summit; V: Valley. (e) Intensity profile of the sample beam after penetrating a ground glass diffuser, which is a seemingly random speckle pattern with no obvious edge profile can be found. Scale bar: 500 μm.

To demonstrate the progressive formation of DOPC-based edge enhancement through scattering media, the intensity ratio (r) between the sample and reference beams was carefully adjusted to be 0.02, 0.10, 1.0, 10 and 50, respectively, during

the hologram writing. The intensity of the sample beam was measured as the mean intensity of the speckle patterns in the region of interest (ROI), i.e. Fig. 4.4e, while the intensity of the reference beam was measured as the mean intensity within the same ROI. The intensity patterns of the conjugated light field are shown in Fig. 4.5 (the first row). As seen, the edge information can be retrieved well from random speckle patterns through DOPC. That said, there are still quite some residual speckle grains even with the DOPC compensation. Especially in Fig. 4.5a and 4.5e, speckle grains are not sufficiently suppressed because of inefficient hologram writing due to the small value of *r*. With increased *r* value, intensities of the retrieved images are suppressed, but the edges are now highlighted (Fig. 4.5i, m, and q). To quantify the transition, similar to Fig. 4.4a, three 280-pixel horizontal dashed lines (1-3) are created for the first row of Fig. 4.5. The intensity distributions along these lines are respectively plotted in the subfigures in the second, third and fourth rows of Fig. 4.5, as indicated by the green lines. For example, (b)-(d) are the intensity profiles corresponding to Lines 1-3 in (a), while (f)-(h) correspond to Lines 1-3 in (e). As seen, when *r* is increased, the degree of edge enhancement is boosted due to the robust speckle elimination. When $r = 50$, as shown in Fig. 4.5r, s and t, the ratio of the noise (speckle grains) to the signal (edges) is strongly suppressed yet the image boundaries are greatly highlighted. It should be pointed out that because of the uneven spatial distribution of the optical beams in the system and the system calibration imperfection, some parts (especially for the bottom) of the recovered patterns are lost in Fig. 4.5. It is also very important to note that whist related, DOPC-

based image and edge enhancement edge enhancement through scattering media are essentially two different directions: for regular imaging through scattering media (not aimed for edge enhancement), the optimal performance is usually acquired around r = 1, as confirmed in Fig. 4.5i; if the purpose is to enhance the edge profile only while the other parts of the image are suppressed, a large value of r is preferred, i.e., the sample beam should be sufficiently stronger than the reference beam (as in Fig. 4.5q). Such difference also highlights the motivation of the study as existing knowledges or experiences on optical focusing and imaging through scattering media cannot be directly applied for edge enhancement.

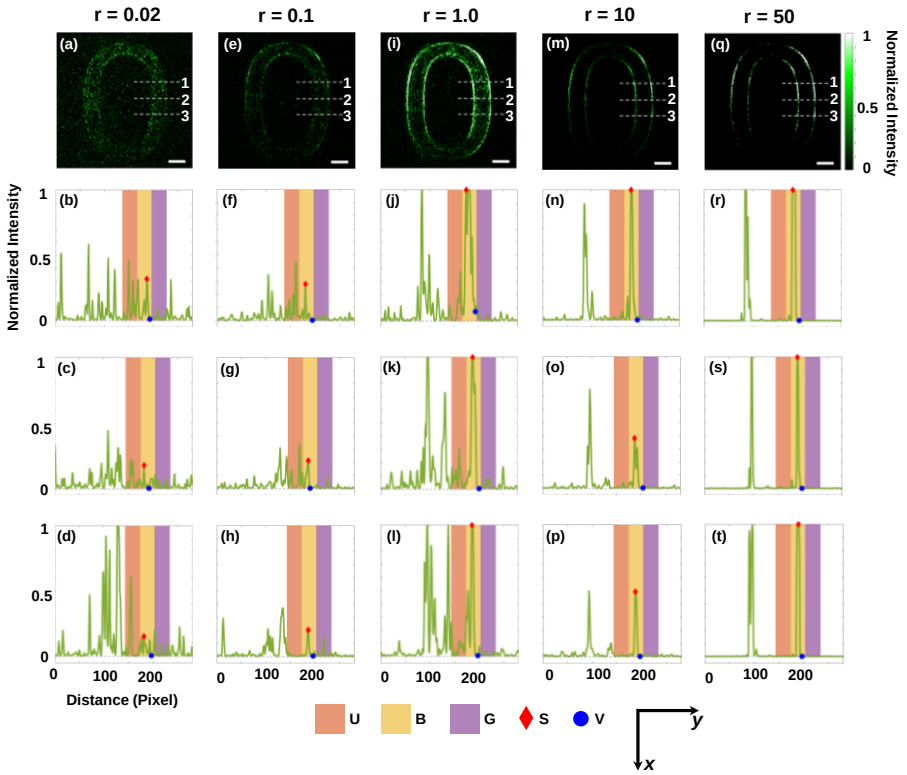

Fig. 4.5 DOPC-based edge enhancement through scattering media. Five images, (a), (e), (i), (m), (q) are recorded by the CMOS camera (Cam_2 in Fig. 4.1) in the playback stage. The intensity ratio (r) between the sample and the reference beams is tuned to different values (0.02, 0.10, 1.0, 10, 50) during the hologram writing. Three 280-pixel horizontal dashed lines

(1-3) are created for the figures in the first row. The intensity distributions along Lines 1-3 are respectively shown in the figures in the second, third and fourth row, as indicated by the green lines. For example, (b)-(d) are the intensity profiles corresponding to Lines 1-3 in (a), while (f)-(h) correspond to the lines in (e). U: Upper level; B: Brink; G: Ground level; S: Summit; V: Valley. Scale bar: 250 μm.

To further quantify the performance of DOPC-based edge enhancement through turbidity, in Fig. 4.6 *EI* and *ENR* versus different beam intensity ratios are plotted. Each data point represents the mean value of *EI* or *ENR* from calculations from Lines 1-3. The *x*-axis represents the common logarithmic scale of the intensity ratio of between the sample and reference beams, i.e. $\lg(r)$. As seen, the mean *EI* (to the left axis) increases from 2.18 (r=0.02) to 18.52 (r=50), and the mean *ENR* (to the right axis) increases from 2.00 (r=0.02) to 525.94 (r=50). Even compared to the direct image of the object in free space (Fig. 4.4a), whose mean *EI* and mean *ENR* are respectively 0.91 and 42.77, the effect of edge enhancement as measured by these two parameters are quite significant, even though a strong scattering medium is penetrated.

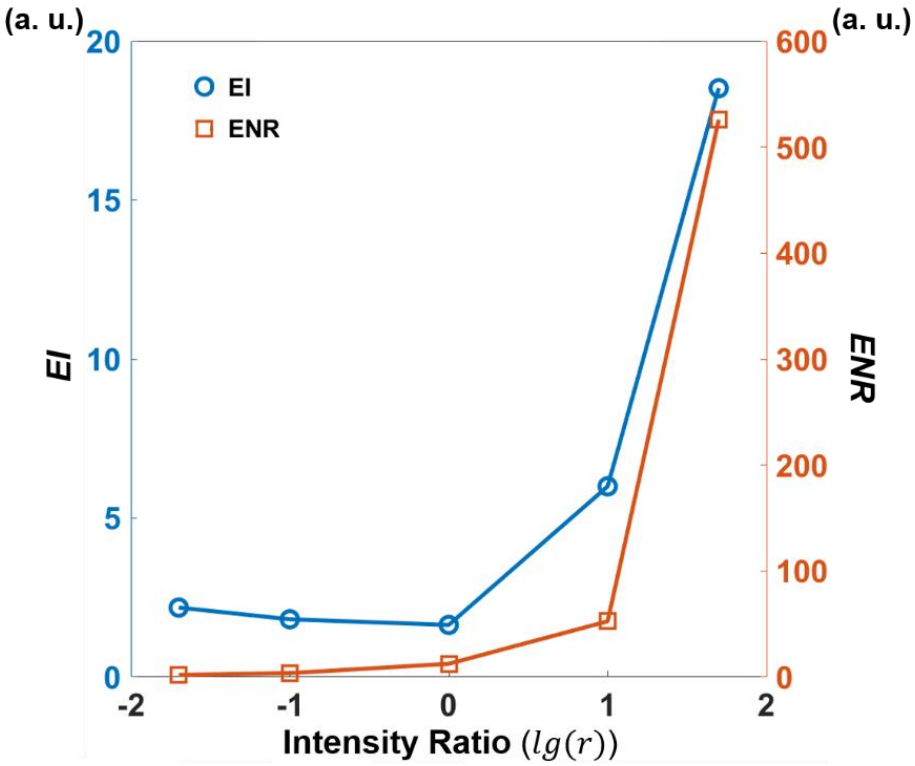

Fig. 4.6 Edge enhancement-index (*EI*) and edge enhancement-to-noise ratio (*ENR*) of edge B for different values of r (0.02, 0.10, 1.0, 10, 50). The *x*-axis represents the common logarithmic scale of the intensity ratio of between the sample and reference beams, i.e. $lg(r)$. *EI* increases from 2.18 to 18.52, and *ENR* increases from 2.00 to 525.94.

The aforementioned results once again confirm the rationality of the proposed method to enhance object boundary through scattering media. Without wavefront manipulation, optical signals, which is an intensity spatial pattern in this study, are thoroughly disordered when transmitting through scattering media and become seemingly random speckle patterns. In this work, DOPC serves as an effective turbidity suppressor and is able to manipulate the optical wavefronts even through complex media. By tuning the sample-reference beam intensity ratio and hence the local modulation efficiency of the PCM as well as calculated phase precision, DOPC is capable to generate modulated wavefronts so that edge profile can be significantly

reinforced from massive speckle noise. That said, we should note the limitation of the performance. Even with a perfect DOPC system, the recovery efficiency is still limited due to the finite control elements of the SLM and other factors such as the uneven spatial distribution of the optical beams and the system calibration imperfection. As a result, only a fraction of speckles is collected and only a fraction of the transmission matrix of the scattering medium is utilized to time reverse the scattered sample beam. Therefore, in practice DOPC is not able to totally overcome scattering, and the recovered edges are still influenced by scattering, as can be observed in Fig. 4.5.

4.4 Conclusion

Edge enhancement plays an important role in many aspects of optical imaging and imaging processing. Recent developments in optical wavefront engineering have paved the way to achieve high quality optical focusing and imaging within or through scattering media; edge enhancement through strong turbidity, however, remains unexplored. While related, existing knowledges or experiences cannot be directly applied for edge enhancement through scattering media. In this section, an effective two-step digital optical phase conjugation (DOPC) approach is proposed. First, a digital hologram is obtained, where information of the object and the edge is encoded with distinct accuracy (high for edges but low for non-edge regions); second, the edge profile is reinforced by phase conjugating the scattered light while the non-edge regions are significantly suppressed. In experiment, with a 600-grit ground glass

diffuser as the scattering medium, the proposed method allows for significant visual enhancement of the edges from noisy speckle patterns. As measured by the enhancement index (*EI*) and enhancement to noise ratio (*ENR*), the edges can be reinforced by ~8.5 and ~263 times, respectively, benefiting from the robust speckle suppression capability. To the best of our knowledge, this is the first time that edge information of a spatial pattern can be extracted clearly through strong turbidity. Moreover, the performance of the edge extraction and enhancement is controllable through tuning the efficiency of the phase conjugation mirror. With further development, this approach may potentially find broad applications or inspire new methods to enrich the comprehension of optical images in the scenario of scattering, such as at depths in biological tissue.

Chapter 5: Wavefront shaping-empowered multifunctional and reconfigurable optical logic gates with diffused light

This chapter is reproduced with some adaptations from the manuscript "Zhipeng Yu, Yuchen Song, Tianting Zhong, Huanhao Li, Wei Zheng, and Puxiang Lai, "Diffusive Optical Logic (DOL): Achieving multifunctional and reconfigurable optical logic operations with wavefront shaping" (*under review*)*". The contributions of authors are as follows: Z.Y. and P. L. conceived the idea. Y.S. and Z.Y. conducted the numerical computation and experiment, and prepared the figures; T.Z., H.L. and W.Z. helped build the optical setup. Z.Y., Y. S. and P. L. wrote the manuscript. P. L. supervised the project.*

In the last two chapters, two essential applications of DOPC from perspectives of optical focusing and image edge enhancement are demonstrated, both of which involve in relatively uncomplicated procedures of wavefront manipulation. In this chapter, more advanced wavefront manipulation procedures will be explored to reconfigure a scattering medium to act as an optical logic operator assisted by wavefront shaping. In this scheme, light is firstly encoded by a digital micromirror device displayed with a precalculated wavefront and then the encoded light is diffused and decoded by a scattering medium to form logical states. As a proof of concept, five basic logic functions (AND, OR, NOT, NAND, NOR) are demonstrated through experiment, with

a ground glass as the scattering medium. As the transmission matrix of strong scattering media has huge ranks and provides enormous degrees of freedom, the concept of diffusive optical logic opens a new way towards easy-to-fabricate, scalable, reconfigurable, and multifunctional optical logic gate computation units.

5.1 Introduction

Optical computing, using photons instead of electrons, has attracted significant research interests in recent years because optics can accomplish the same goals as digital electronics, but in a more efficient or advantageous manner[150-155]. The benefits, such as large bandwidth, ultrahigh speed, low energy consumption, low heat generation, and low crosstalk, make it potential in many scenarios, particularly those involving high-throughput and on-the-fly data processing such as artificial intelligence[156-158]. Optical logic gates are the fundamental building blocks of optical computing; its exploration is thus particularly important. Existing optical logic components are mostly based on waveguide[159-165] or metasurfaces[166,167]. For the first category, logical states are achieved mainly due to constructive/destructive interference effects between input signals, and a precise control of the basic properties (phase, polarization, and intensity) of individual optical signals transmitting into the waveguide should be applied. Note that for the purpose of scalability, a many of small waveguides are needed and placed close to each other for a compact and miniature structure, which, however, introduces strong crosstalk, increases fabrication complexity and control difficulty. For the second category, a plane wave is usually used as the input signal, but the optical structure

requires complex and often tedious processes for accurate calculation, simulation, as well as fabrication. Furthermore, both two categories are built upon inverse design, inherently prohibiting reconfigurability[163,168,169] . Moreover, variation of environmental conditions affects the functioning, limiting the range of operation of the device. Optical logic components with simple fabrication, reconfigurability, and scalability are highly desired due to its importance for the development of novel architectures for all-optical devices and systems. Such a goal has been sought after for long yet considered challenging.

As discussed in Chapter 1, Vellekoop *et al.* showed that coherent light can be refocused through a highly scattering medium in 2007[58], which has spawned a new research field called wavefront shaping[49,144,170-173]. As known, when coherent light transmits within or through scattering-dominated media (with an assumption of no or weak absorption), such as a ground glass or biological tissue, the optical wavefront is scrambled due to scattering, forming visually random speckle patterns. This seemingly random process is actually deterministic within a specific time window[48], within which a TM model can be used to bridge the input and output optical fields[173]. For strong scattering media, the distribution inhomogeneity of refractive index is on a sub-wavelength scale, which can support a large number of optical modes and hence a TM of large dimension. Moreover, the random distribution of scatterers within the medium induces asymmetry, resulting in a TM of high rank. If the incident light is modulated by a SLM with a wavefront that is inverse to the TM or other well-chosen wavefronts, an optical scattering medium can

be used to perform a wide variety of functions that used to be impossible, such as optical focusing[81], image transmission[173], programmable quantum network[152], and reconfigurable linear operation[174].

Inspired by these exciting features of TM-based wavefront shaping, diffusive optical logic (DOL) is proposed by using a DMD to encode input signals and then using a ground glass to decode the information to form logical states. The DMD aperture is firstly divided into several subregions, as illustrated in Fig. 5.1, that correspond to binary input digits ("0" and "1"), logic types (AND, OR, NOT, NAND, NOR), and a common reference region, respectively. The sub-TM of the scattering medium corresponding to each subregion is determined by the TM-based wavefront shaping approach[61,175]. Two randomly picked small areas on the output plane (*i.e.* the camera sensor) serve as the output optical logic states "0" and "1"; light projected from each DMD subregion through the scattering medium can be refocused in these two areas (individually or both) with two different phase states ("0" indicates in phase and "π" indicates opposite phases) with respect to the speckled pattern projected from the common reference region on the DMD. Built upon constructive or destructive interference among the focuses, different combinations of subregions on the DMD loaded with precalculated wavefronts can perform different logical functions with the assist of a commercial ground glass. Note that ground glasses can be easily fabricated in bulk with standard protocols and can be replaced easily by other scattering media such as scattering chips and scattering metasurfaces. Such an option saves researchers

a lot of time and efforts compared with fabricating a well-designed component, making it compatible for extended applications. On the other hand, the TM of a ground glass has an infinite dimension and a high rank, empowering a small ground glass to support a large number of optical logic gates in a highly integrated computation system. An inverse design adopted in existing optical logic gates is usually incompatible with reconfigurability. But the method can bypass this annoyance: when the system condition is considerably changed, which causes large variations to the TM of the ground glass, another round of rapid TM-based wavefront shaping can be performed, recovering the states of the optical logic gates. Collectively, the proposed method empowers reconfigurability and scalability to the design and construction of optical logic gates, and in the meantime simplifies the manufacturing process. Moreover, it shows potentials in many other fields, such as optical encryption[176] and optical micro manipulation[177,178].

5.2 Methods

5.2.1 The principle of Diffusive Optical Logic

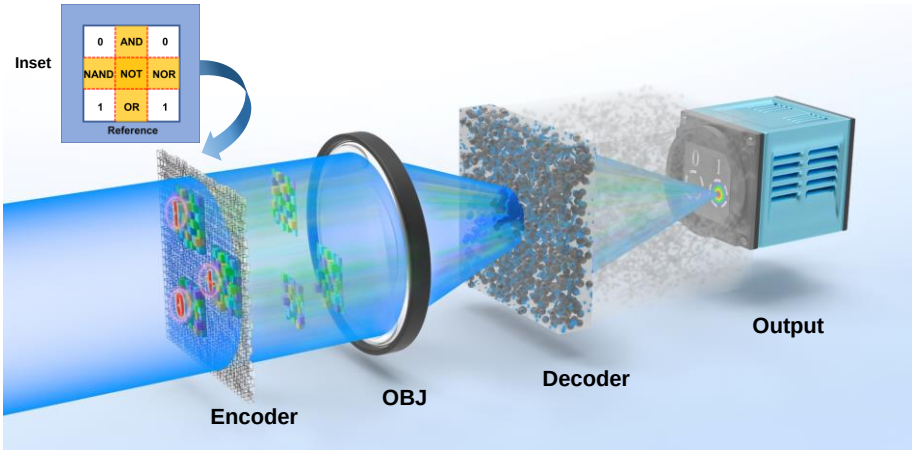

Fig. 5.1 Schematic diagram of diffusive optical logic. The encoder is a digital micromirror device (DMD) of reflection type. For simplicity, it is shown here in transmission mode. OBJ: objective lens; Decoder: a ground glass diffuser. The inset illustrates the arrangement of subregions on the DMD. Subregions marked in yellow represent the logic type control units, subregions marked in white represent the binary input digit control units, and the subregion marked in blue serves as the common reference region.

Fig. 5.1 illustrates the schematic of the proposed diffusive optical logic. The encoder (input layer) of the logic gates is a DMD, which is used in this experiment with two aims. Firstly, it serves as a spatial light modulator that provides binary amplitude modulation to the wavefront of the input light. Secondly, it functions as a fast optical (spatial) switch as the direction of the reflected light from the DMD is subject to change when the DMD pixels are at different states (“on” or “off”). As shown in the inset of Fig. 5.1, the DMD screen is divided into two parts: the central region consists of nine working subregions that control the binary digit or logic type of the input, and the

peripheral region (in blue) serves as the common reference region. Among the nine subregions, four are for input binary digits, marked as digit “0” or “1” (subregions of the same column belong to one set), and the rest represent logic types (AND, OR, NOT, NAND, NOR). These nine working subregions are equal in area and the ratio of the pixel number between the reference region and each working subregion is about 8. On the output plane, two regions are selected to represent the logical states “0” and “1”.

During the TM measurement process, all pixels in the reference region are switched “on” (light reflected from the reference region is illuminated onto the scattering medium, which generates a reference speckle pattern). These pixels are switched “off” when the TM measurement ends. Note that the sub-TMs of the nine working subregions are measured in sequence; the required intensity and phase of each focus is calculated in advance, which is used to inversely derive the wavefront to be displayed in each subregion on the DMD.

For any logic operation, only subregions involved remain “open”, and other subregions are “closed” with the corresponding pixels switched to “off”. The output images are recorded by a CMOS camera. Taking logic operation “0•1” as an example. As illustrated in Fig. 5.1, three subregions marked as “0” (from the leftmost column), “AND”, and “1” (from the rightmost column) are selected and displayed with pre-calculated wavefronts; these three subregions are set to be “open” while other subregions are “closed”. The output logical state is “0”, so on the output plane a bright

focus is formed at the region corresponding to logic state “0”. Other optical logic operations have similar procedures, except for logic operation “NOT”. For optical logic operations “ $\overline{\mathbf{O}}$ ” and “ $\overline{\mathbf{1}}$ ”, only two subregions are “open”: one corresponds to the input binary digit and the other represents logic type “NOT”.

5.2.2 Transmission matrix measurement

In this work, a transmission matrix method is used to relate the relationship of electric fields between the input and output channels. Let us denote $T = \begin{bmatrix} t_{1,1} & \cdots & t_{1,n} & \cdots & t_{1,N} \\ \vdots & & \vdots & & \vdots \\ t_{k,1} & \cdots & t_{k,n} & \cdots & t_{k,N} \\ \vdots & & \vdots & & \vdots \\ t_{K,1} & \cdots & t_{K,n} & \cdots & t_{K,N} \end{bmatrix}$ to be the transmission matrix (TM) of the scattering medium, and $T_k = [t_{k,1} \cdots t_{k,n} \cdots t_{k,N}]$ to be the k^{th} row vector of T, connecting the k^{th} input and output channels. Here, *N* is the number of control units on the DMD, and K is number of output channels. Let us further denote $E_{out} = \left[e_{out\_1} \cdots e_{out\_k} \cdots e_{out\_K} \right]$ as the electric field of focuses at all output channels, and e_{out_k} as the electric field of the focus at a desired output channel (k^{th}). e_{out_k} is the sum of contribution from all input channels and is given by

$$e_{out\_k} = T_k (D_k e_0)^{\dagger}, \tag{5.1}$$

where e_0 represents a plane wave which will be illuminated onto DMD. $D = \begin{bmatrix} d_{1,1} & \cdots & d_{1,n} & \cdots & d_{1,N} \\ \vdots & & \vdots & & \vdots \\ d_{k,1} & \cdots & d_{k,n} & \cdots & d_{k,N} \\ \vdots & & \vdots & & \vdots \\ d_{K,1} & \cdots & d_{K,n} & \cdots & d_{K,N} \end{bmatrix}$ is the binary modulation matrix, and symbol “ $\dagger$

" represents the transpose of the matrix, and $D_k = \left[d_{k,1} \cdots d_{k,n} \cdots d_{k,N} \right]$ is the k^{th} row vector of D and it is the pattern to be displayed on the DMD to produce a focus at the k^{th} output channel. Then the intensity of focus at the designated output channel can be calculated:

$$I_{out\_k} = \left| e_{out\_k} \right|^2 = \left| \sum_{n=1}^{N} t_{k,n} d_{k,n} e_0 \right|^2, \tag{5.2}$$

where $t_{k,n}$ follows a circular Gaussian distribution[58]. To maximize the intensity at the targeted output position (in phase with the common reference), control units on the DMD can be modulated to obtain constructive interferences with the reference at targeted positions by switching on constructive channels and blocking others. $d_{k,n}$ can be determined based on the value of $t_{k,n}$, following a criteria introduced in Ref. [179]:

$$d_{k,n} = \begin{cases} 1 & \mathrm{Re}(t_{k,n} e_0) \geq 0 \\ 0 & \mathrm{Re}(t_{k,n} e_0) < 0 \end{cases}. \tag{5.3}$$

The main goal of doing so is to determine the sign of every element of $\mathrm{Re}(T)$. If Hadamard basis is sed to represent the input, the output light field for different Hadamard modes on the DMD is

$$\left[E_{H1} ... E_{Hn} \cdots E_{HN} \right] = T \left[h_1 \cdots h_n \cdots h_N \right]^{\dagger} e_0, \tag{5.4}$$

where E_{Hn} is the output field for n^{th} Hadamard mode, which is a $K \times 1$ vector. h_n is the n^{th} Hadamard mode, which is a $N \times 1$ vector. As a Hadamard matrix has the inverse property of $\mathrm{HH^T} = \mathrm{NI}$, $\mathrm{Re}(Te_0)$ can be calculated by

$$\mathrm{Re}(Te_0) = \frac{1}{N} \left[\mathrm{Re}\left(\left[E_{H1} \cdots E_{Hn} \cdots E_{HN} \right] \right) \right] \left[h_1 \cdots h_n \cdots h_N \right]^{\dagger}. \tag{5.5}$$

It is challenging to directly measure $\mathrm{Re}(E_{Hn})$ as elements of the Hadamard matrix are either -1 or 1. To solve the issue, a same method as Ref. [61] is used by adding a

uniform reference input. Two binary DMD patterns ($r_n^{\pm}$) which only contain 0 and 1 are generated for each h_n added with a uniform reference:

$$r_n^{\pm} = \frac{1}{2}(h_1 \pm h_n). \tag{5.6}$$

The uniform reference input field is the first Hadamard basis vector, $h_1 = [1 \cdots 1]$. Note that in the proposed method, an extra reference region is introduced, as shown in Fig. 5.1, to bridge the phase relationship among focuses generated from different subregions. The intensity of the resultant output light field on the output plane can be expressed by

$$I_{total\_n}^{\pm} = \left|Tr_n^{\pm}e_0 + E_{ext}\right|^2 = \left|E_{ref} \pm \frac{1}{2}Th_n e_0\right|^2 = \left|E_{ref}\right|^2 + \frac{1}{4}\left|E_{Hn}\right|^2 \pm \mathrm{Re}(E_{ref}^* E_{Hn}), \tag{5.7}$$

where $E_{ref} = \frac{1}{2}Th_1 e_0 + E_{ext}$ is the electric field of the resultant output light field from the uniform reference input field ($\frac{1}{2}Th_1 e_0$) and the extra reference region (E_{ext}). E_{Hh} is the electric field for input of the n^{th} Hadamard basis vector, which can be derived from equation (5.7)

$$\mathrm{Re}(E_{Hn}) = \frac{\frac{1}{2}(I_{total\_n}^{+} - I_{total\_n}^{-})}{\sqrt{I_{ref}}} \cong \frac{\frac{1}{2}(I_{total\_n}^{+} - I_{total\_n}^{-})}{\sqrt{I_{\mathrm{ext}}}}, \tag{5.8}$$

where I_{ref} is the optical intensity of the resultant output light field from the uniform reference input and the extra reference region, and I_{ext} is the optical intensity of the output light field from the extra reference region. As the extra reference region is 8 times larger than the working region, I_{ext} is much larger than that from the working region, thus we have $I_{ref} \cong I_{ext}$ At last, the condition in equation (5.3) can be obtained from equations (5.5) and (5.8). By introducing a large reference region, after wavefront shaping, the phase of focuses generated from each DMD subregions can be precisely controlled: it can be either in phase or in opposite phase with reference speckle field

resultant from the reference region.

5.2.3 Optical setup

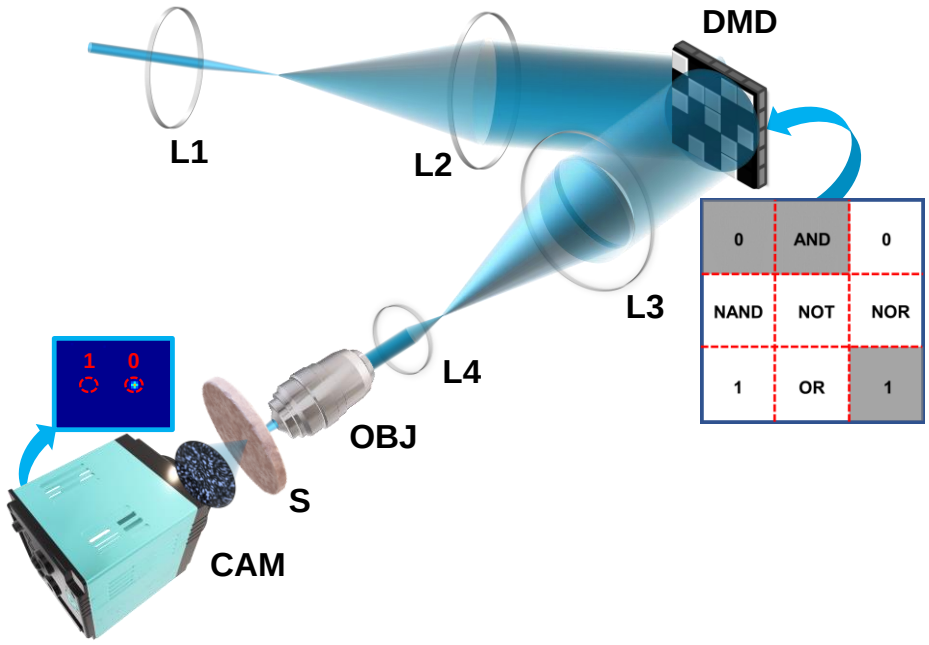

Fig. 5. 2 Optical setup of DOL. CAM: CMOS camera; DMD: digital micromirror device; L1-L4: lens; OBJ: objective lens; S: ground glass diffuser as the scattering medium. The figure presents a logic output state of "0" for logic operation "0·1" (with DMD Subregions 0, AND, and 1 activated).

A continuous wave laser source of 488 nm wavelength (OBIS LS, Coherent, USA) serves as the light source, and the maximum output power is 150 mw. Light is first expanded by a 4-f system (lens L_1 from Thorlabs, AC254-30-A, f = 30 mm and lens L_2 from Thorlabs, AC254-200-A, f = 200 mm) to illuminate the whole screen of the DMD (V-9501, Vialux GmbH, Germany). After being modulated and reflected by the DMD, light is shrunk by another 4-f system (lens L_3 from Thorlabs, AC254-200-A, f = 200 mm, and L_4 from Thorlabs, AC254-30-A, f = 30 mm), and then it is converged by an

objective lens (40×/0.65, Daheng Optics, China) onto a ground glass diffuser (DG10-120, Thorlabs, USA). At last, the output optical field is recorded by a CMOS camera (BFS-U3-04S2M-CS, FLIR Integrated Imaging Solutions Inc., Canada), which is triggered by the DMD. In experiment, once the DMD pattern is updated, the camera will record an optical pattern.

5.3 Results

5.3.1 Intensity and phase control for optical focuses through scattering media

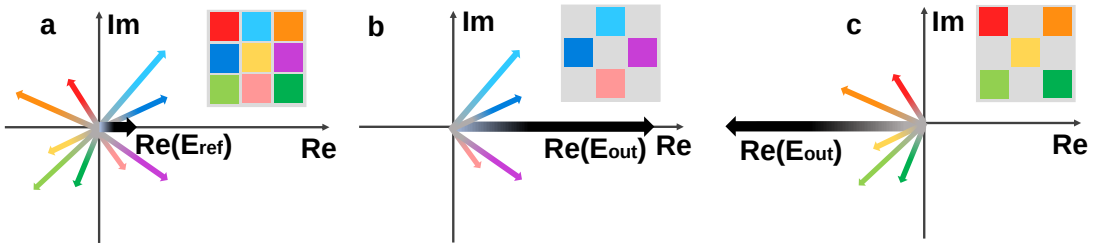

Fig. 5.3 (a) Optical transmission through a scattering medium without binary modulation. The optical field E_{Ref} at the target is the sum of electric fields coming from all optical channels, and it is used as the reference. (b) After measuring the binary transmission matrix (TM) of the medium, an enhanced focus at the target, which is in phase with the reference, is achieved by blocking the channels that interfere destructively with E_{Ref}. (c) An enhanced focus at the target, which is in opposite phase with the reference, is achieved by blocking the channels which have constructive interference with E_{Ref}.

The proposed concept is achieved based on constructive or destructive interference among focuses of different subregions, and hence the key is how to modulate the phase and intensity of each individual optical focus. In Ref. [175], the speckle field from the

scattering medium when all DMD pixels (channels) in the working region are switched "on" is used as the reference during the TM measurement process. For a fully scattering medium, the phase profiles of the resultant optical field are randomly distributed, suggesting that the phase and intensity of optical field resulting from different input channels are randomly distributed, as illustrated in Fig. 5.3a. To achieve constructive interference at the output plane, which is needed to obtain an optical focus, we need to block channels that lead to destructive interference with the reference E_{Ref}. That is to open the channels with output phase in the range of $(\varphi_{ref} - \pi/2, \varphi_{ref} + \pi/2)$ while block the other channels, where φ_{ref} is the phase of the reference[175]. As a result, the optical focus is in phase with the reference speckle field, as shown in Fig. 5.3b. On the contrary, if we block channels that have constructive interference with the reference, a bright focus with an opposite phase to the reference speckle field can be obtained, as shown in Fig. 5.3c. Optical focuses from different subregions in the same area on the output plane can be obtained, but there is no explicit phase difference among their phases as their reference speckle fields are different. As the logic states are achieved based on constructive or destructive interference between different focuses generated by different working regions at the same position on the output plane, furtherly bridging the phase relationship between different focuses is crucial.

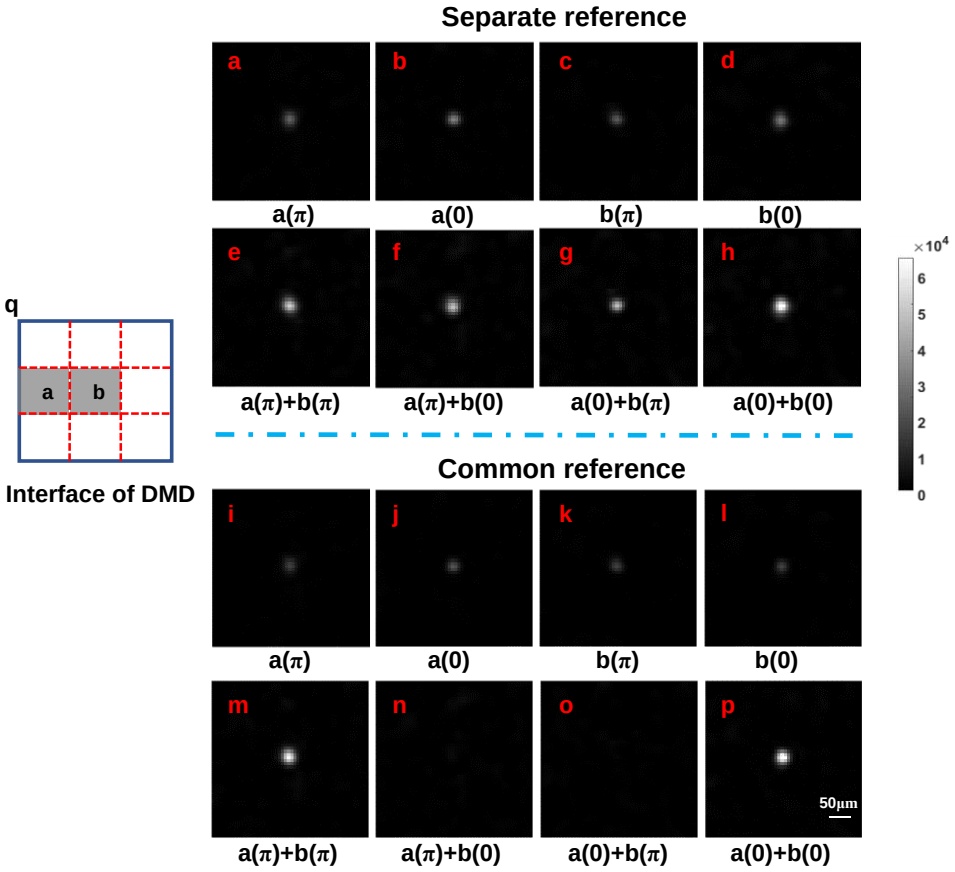

Fig. 5.4 Illustration of focuses generated from different subregions with separated or common reference as well as their interference. (a)-(d): Optical focus, which is in phase or opposite phase with the reference, is achieved with a separate reference for each subregion; (e)-(h): Results of interference between focuses generated from Subregions a and b shown in (a)-(d); (i)-(l): Optical focus, which is in phase or opposite phase with the reference, is achieved with a common reference for all subregions; (m)-(p): Results of interference between focuses generated from two subregions shown in (i)-(l); (q) The arrangement of the DMD screen. Two subregions marked in grey serve as the working regions, denoted as "a" and "b", respectively. "a(0)" indicates the focus is in phase with the reference; "a(0)+b(π)" represents the inference between one focus (in phase with the reference) generated from Region "a" and one focus (in opposite phase with the reference) generated from subregion "b".

Therefore, the aforementioned method is modified by introducing a common reference subregion on the DMD (the blue region in Fig. 5.1). All pixels in the reference subregion are switched "on" to project light into the scattering medium during the entire TM measurement process for all working subregions (control units). There are a lot more pixels in the reference region than each working region to ensure that the reference contribution dominates in the interfered speckled field. To illustrate the procedure, two subregions marked in grey on the DMD are used and renamed as Regions a and b, respectively, as shown in Fig. 5.4. Each sub-TM of the scattering medium corresponding to these two regions will be calculated in sequence. A Hadamard matrix of a size of $2^{10}\times2^{10}$ is used to calculate each the sub-TM for each subregion (128×128 pixels) with 4×4 DMD pixels merged as one mega pixel. The experimental verification can be found in Fig. 5.4. "0" in the bracket means the focus is in phase with the reference and "π" in the bracket means the focus is in opposite phase with the reference.

Two groups of experiments were performed. The first group adopted separate reference for each subregion (with all pixels in the corresponding subregion switched "on"). The resultant optical focuses as well as their interference with subregions in phase or opposite phase to the reference are shown in Figs. 5.4a-h. The second group adopted the aforementioned common reference for all subregions, and the corresponding results are shown Figs. 5.4i-p. As seen, with separate references, constructive and destructive interference cannot be observed at the same time for different combinations of phase

relationship between the two subregions. This indicates that there is no explicit phase difference (not in phase or in opposite phase) between the two focuses formed by different subregions. The results are chosen from 100 groups of experiment data. Statistics results suggest a state of complete disorder in different areas on the output plane. By contrast, with a common reference, these is constructive interference, as represented by enhanced focal intensity, when the two focuses are both in phase or opposite phase with the common reference, and these is destructive interference when one focus is in phase but the other is in opposite phase with the common reference, which is shown in Fig. 5.5. This shows the importance and necessity to regulate the phase of focuses formed by various subregions with respect to the common reference.

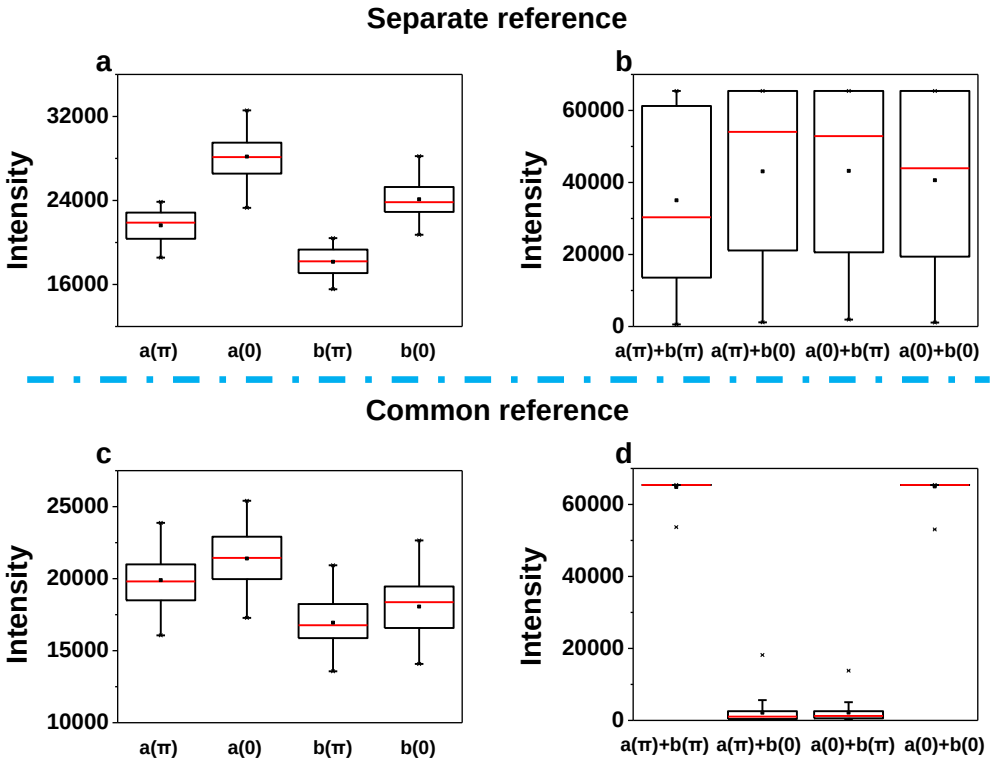

Fig. 5.5 Statistics of intensities of focuses in Figs. 5.4(a-p) in the main text. Results with separate reference are shown in (a) and (b), corresponding to before and after field

interference of two subregions, respectively. The intensities of focuses after interference distribute in a large range, indicating the lack of an explicit phase difference among focuses generated by two subregions. Results with a common reference are shown in (c) and (d), corresponding to before and after field interference of two subregions, respectively. The sharp contrast of focal intensities (interference between fields of same phase versus interference between fields of opposite phase) confirm that the desired phases of focuses generated by different subregions are accurate and hence suitable for constructive and destructive interference.

5.3.2 Interference of dual-focus optical fields formed by individual DMD subregions

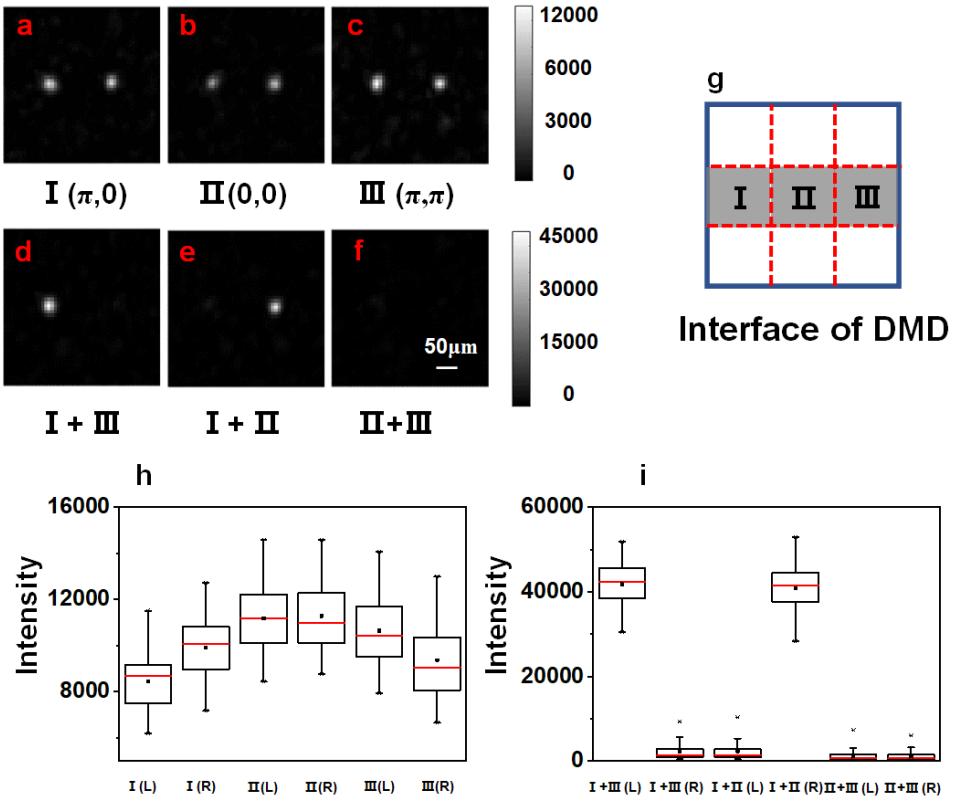

Fig. 5.6 Illustration of phase and intensity control before and after interference of optical fields

formed by individual DMD subregions. (a) Optical focus on the left of the output plane is in opposite phase and optical focus on the right is in phase with the common reference; generated from Region I. (b) Both optical focuses are in phase with the reference; generated from Region II. (c) Both optical focuses are in opposite phase with the reference; generated Region III. (d-f) Interference of optical fields generated by any two regions. For example, "I+II" represents the interference on the camera plane between optical fields from Regions I and II. Note that (a)-(c) share the same colorbar, (d)-(f) share the same colorbar, and (a)-(f) share the same scalebar. (g) The arrangement of the three subregions on the DMD. (h)-(i): Statistics of intensities of the dual focuses shown in (a)-(f) in the main text.

If only one focus is generated from one DMD subregion, the logic operations cannot be completed. For example, for operation "$\bar{0}$" with logic output of "1", there should be constructive interference between optical focuses formed by DMD subregions corresponding to control units "0" and "NOT" in the designated area on the output plane for logic state "1" but destructive interference in the designated area for logic state "0". Therefore, two focuses of specific intensity and phase in the designated areas on the output plane should be generated synchronously by one DMD subregion. To achieve that performance, binary patterns to be displayed on individual subregion that can lead to a focus in any designated area on the output plane can be calculated after the TM is determined. Two patterns, represented by row vectors $X=\left[x_1\cdots x_n\cdots x_N\right]$ and $Y=\left[y_1\cdots y_n\cdots y_N\right]$ (N is the pixel number), are selected to generate an optical focus respectively in designated areas on the output plane. In order to generate two focuses synchronously, a new pattern $Z=\left[z_1\cdots z_n\cdots z_N\right]$ can be calculated based on an

intersection operation between these two DMD patterns, that is $z_n = \begin{cases} 1, \text{ when } x_n \times y_n = 1 \\ 0, \text{ when } x_n \times y_n = 0 \end{cases}$. As demonstrated earlier, channels that interfere destructively with the reference field should be blocked to highlight the constructive interferences and hence to make the focus in phase with the reference. In this experiment, even though the intersection operation will weaken the intensity of each of the two focuses, there are still a large portion of channels that interfere constructively with each other, forming focuses that are in phase or opposite phase with the reference. Also, it should be noted that there might be crosstalk between the resultant two focuses as they originate from the same DMD subregion. But how this effect influences the phase and intensity of the two focuses needs further exploration.

The experimental verification is given in Fig. 5.6. Three subregions on the DMD screen, marked in grey in Fig. 5.6g, are used and referred as Regions I, II, and III (distinctive from Regions a and b in Fig. 5.4q). They are selected from the nine subregions; each subregion can generate two optical focuses in the designated areas on the output plane with desired phases, as exampled in Figs. 5.6a-c. The desired phases of the focuses formed by Region I are π (left) and 0 (right), those by Region II are 0 (left) and 0 (right), and those by Region III are π (left) and π (right). Interference of different combinations of these three optical fields (*i.e.,* I+III, I+II, and II+III) are shown in Figs. 5.6d-f. As seen, in Fig. 5.6d, a brighter focus is observed on the left but the focus on the right is suppressed, indicating that there is constructive interference (π and π) for the left focus but destructive interference (0 and π) for the right focus. In Figs. 5.6e and f, consistent

results are obtained. These results confirm that desired phases are correctly designated, and the intersection operation does not affect the phase of the optical focuses. Statistics about the intensity of different focuses in Figs. 5.6a-f can be referred to Figs. 5.6h and i. Fig 5.6h shows the intensity distribution of the dual focuses from the three DMD subregions as shown in Fig. 5.6g in the main text after the intersection operation. As seen, no significant imbalance of focal intensity is found among all these focuses; the moderate difference may attribute to the variations of enhancement efficiency for different DMD subregions and different output plane positions. Fig 5.6i shows the intensity distribution of interfered fields between any two of the dual-focus patterns as shown in Figs. 5.6(a-c) in the main text. As seen, when the desired phases of focuses are the same, such as I+III (L) and I+II (R), the focus intensity can be increased by ~4 times, confirming the left focuses formed by I and III are accurately in phase (both have phase of π), and so are the right focuses formed by II and II (both have phase of 0). On the contrast, when the desired phases of focuses are opposite, the focal intensities after interference are almost zero, confirming these focuses are in opposite phase (*i.e.,* one is π and the other is 0). These results confirm that desired phases are correctly designated, and the intersection operation does not affect the phase of the optical focuses.

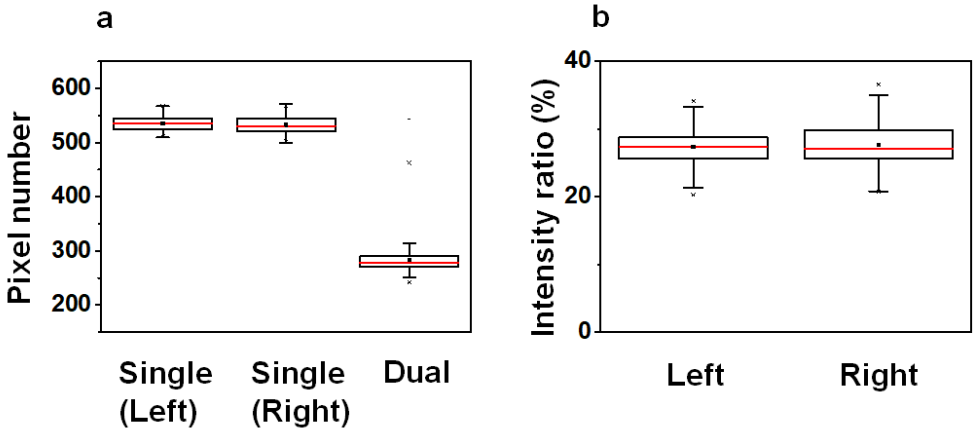

Fig. 5.7 (a) Number of pixels in Region II shown in Fig.5.6(g) that should be switched "on" in order to generate a single focus on the left, a single focus on the right and dual focuses, respectively, after the intersection operation. (b) Ratios of intensity of the two focuses with respect to that of the focus before the intersection operation. Red lines indicate the median values.

Next, let us examine how the intersection operation affects the intensity of optical focuses. Region II was selected as the working subregion, and 100 pairs of areas on the output plane were picked randomly. As seen, almost half of the pixels in Region II will be switched "off" (active pixels reduced from around 520 down to around 260) after the interference operation, as shown in Fig. 5.7a. As the focal intensity is linearly correlated with the effective pixel number[58], the resultant focal intensity is expected to decrease by half. As the remaining pixels are used to contribute to two focuses, intuitively intensities of each focus will be decreased by another half. Note that, however, there might be competition of energy between the two focuses during the whole transmitting process as photons are from the same DMD subregion. To check that, the statistics of experimental focal intensities before and after the intersection

operation were obtained. As shown in Fig. 5.7b, no significant imbalance of focal intensity is found between the two focuses, and the intensity of each of the two focuses is approximately one quarter of that of the focus before the intersection operation (amplitude of the electric field of the focus almost halves), agreeing quite well with the deductions above.

These results confirm that the intersection operation, although simple, is an effective and reliable method to control the phases and intensities of the focuses formed by individual DMD subregions, which is the foundation of achieving the proposed optical logic operations.

5.3.3 Arrangement of focuses formed by individual DMD subregions and the experimental verification

a

Focus area \ Active unit	0 (left)	1 (left)	0 (right)	1 (right)	AND	OR	NOT	NAND	NOR
"0"	0.5|u|	−0.5|u|	0.5|u|	−0.5|u|	|u|	×	−0.5|u|	×	−|u|
"1"	0.5|u|	−0.5|u|	0.5|u|	−0.5|u|	×	−|u|	0.5|u|	|u|	×

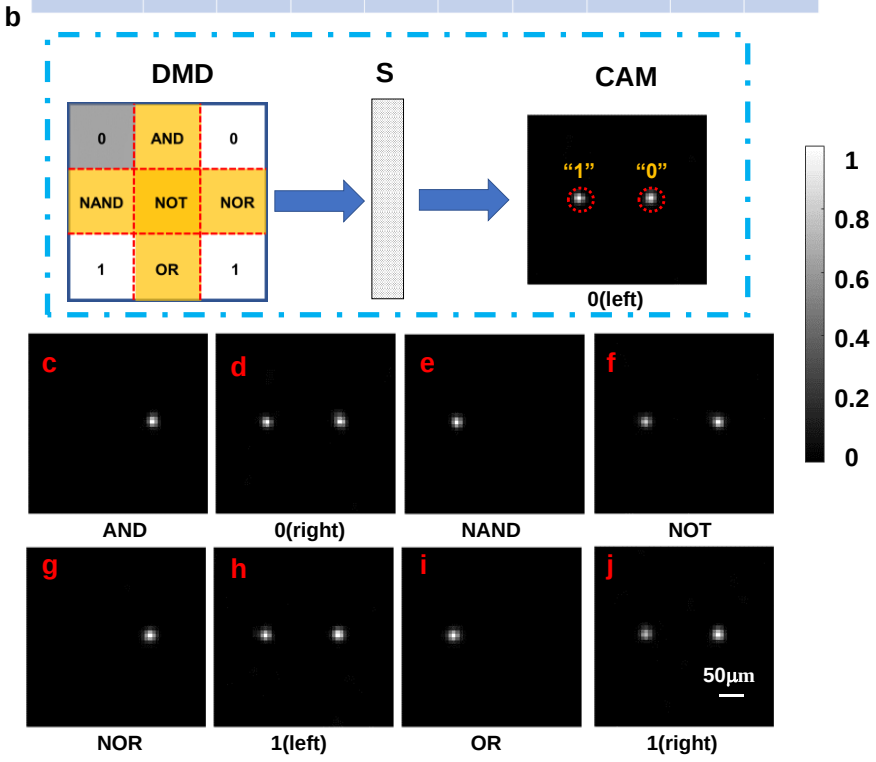

Fig. 5.8 (a) Design arrangement of focuses formed by the nine DMD subregions via numerical computation. The interpretation of the table is exampled as follows: When the "zero" subregion on the left column of the DMD is selected as the working/active region, on the output plane, a focus with a field amplitude of 0.5|u| is formed at the "0" area (on the right of the camera screen), and another focus with the same field amplitude of 0.5|u| is simultaneously formed at the "1" area; when the "AND" subregion on the DMD is selected, only a focus with

a field amplitude of |u| is formed at the "0" regime on the output plane. Symbol "|u|" represents the absolute amplitude value of the electric field of single focus generated from individual DMD subregions, and "0.5|u|" means there is an intersection operation on the corresponding subregions, leading to dual focuses, whose absolute amplitude value of the electric field is reduced by half. "×" indicates there is no focus formed at the designated area. "-" means that focus is in opposite phase with the common reference; without "-" means the focus is in phase with the reference. (b-j) Experimental verification of the desired focus arrangement. As an example, in (b), a binary digit control unit ("0" on the left column of the DMD, marked in grey), is selected. Two focuses are formed in the designated areas at the output plane behind the scattering medium, producing logic states "0" and "1" (marked in yellow on the output plane). Blue arrows indicate the transmission of light. Results with other control units are shown in (c-j). Abbreviations: DMD, digital micromirror device; S, ground glass; CAM, camera. Intensities are normalized to the maximum intensity in each figure.

An inverse design approach was taken. First, the desired intensity and phase (0 or π) of each focus for a set of basic logic functions (AND, OR, NOT, NAND, NOR) were calculated and the calculation process can be referred to Table 1 in the supplementary material of this chapter. The solution is given in Fig. 5.8a and explained in detail in the figure caption. These results were used to calculate the wavefront of each DMD subregion in reverse. Note that two randomly picked areas on the output plane serve as logic states "0" and "1". The experimental verification of the design arraignment was shown in Figs. 5.8b-j.

As an example (Fig. 5.8b), when only the subregion corresponding to “0” on the left column of the DMD (marked in grey) is switched “open” and loaded with the precalculated wavefront, two optical focuses can be observed in both picked areas. Figs. 5c-j display the output images when other subregions are “on” (one active subregion at one time) and loaded with the corresponding precalculated wavefront. As seen, all experimental results agree well with the simulated sets in Fig. 5.8a. The enhancement ratio defined as the ratio between the optimized intensity and the average intensity before optimization[58] for cases with one focus (Figs. 5.8c, e, g, and i) is about 70 (43% of the theoretical value predicted by 164); for cases with two focuses (Figs. 5.8d, f, h, and j), the enhancement ratio is about 30. The difference is reasonable as the number of effective channels contributing to the focuses are reduced by half due to the intersection operation, which is has been discussed earlier.

5.3.4 Experimental demonstration of basic logic functions

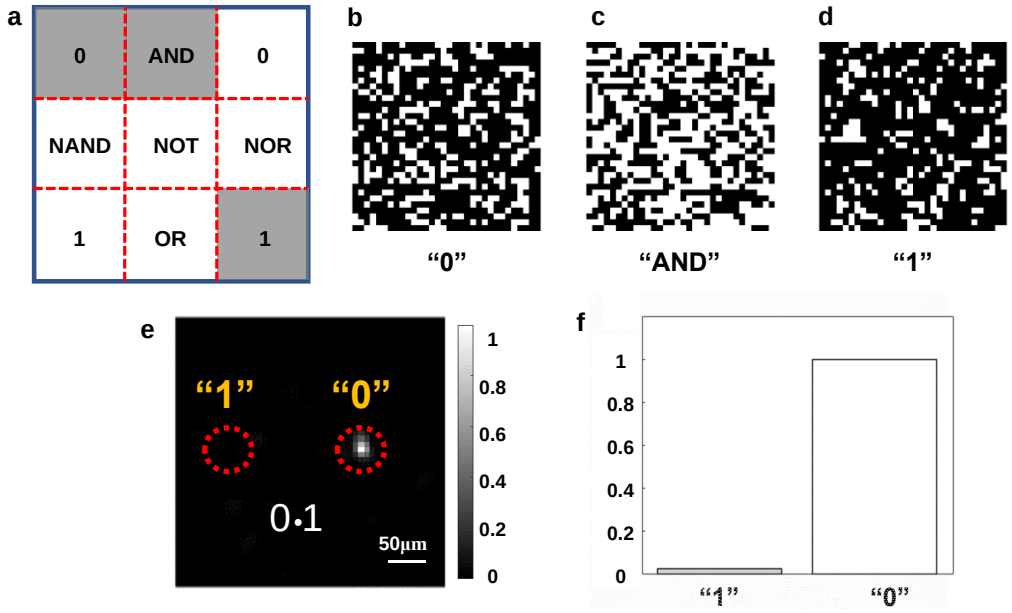

Fig. 5.9 DMD subregion arrangement and experimental demonstration of a logic AND operation. (a)States of different subregions on the DMD for logic operation “0•1”. Subregions marked in grey are “on” and the others are “off”. (b-d) The calculated binary wavefronts (pixels in white are switched “on”) are displayed on DMD Subregions “0”, “1”, and “AND, respectively. Each generates a corresponding optical field as shown in Fig. 5.8. (e) Interference of the three optical fields yields the output field, which is recorded by a camera. The intensity profile of “0” and “1” within the red circle represents the logic output states. For example, the current pattern means an output logic state of 0 as the “0” focus/signal remains but the “1” focus/signal vanishes. (f) Normalized intensity profile of the “1” area and “0” area in (e).

Now, let us move onto the demonstration of the proposed optical logic gates. The DMD subregions will display the corresponding calculated wavefronts after the sub-TMs are measured for logic operations. In this process, the DMD serves as a wavefront modulator and a fast spatial switch (with a switching speed of up to 23 kHz). For a

given logic operation, the corresponding subregions are set to be “on” while the others are “off”, in which the DMD is used as a spatial switch. Fig. 5.9 shows the DMD deployment and the experimental results of logic operation “0•1”. States of different subregions of the DMD for this logic operation are given in Fig. 5.9a, where subregions marked in grey correspond to binary digit control units “0” (left column) and “1” (right column) as well as the logic type control unit “AND”. These three subregions are activated and loaded with the corresponding wavefronts that are precalculated based on the transmission matrix method discussed earlier; the other subregions remain “off” in operation. The optical output behind the ground glass is recorded by a camera, as shown in Fig. 5.9e. A bright focus can be observed at the area of logic state “0” (the circle on the right), meaning that the current logic output is “0”, which is consistent with the actual value of logic operation “0•1”. Normalized intensity profile of these two areas is shown in Fig. 5.9f, which can be furtherly used to analyze the intensity contrast of this logic operation. Quantitatively, an intensity contrast ratio of 15.8 dB is obtained for the exampled “0•1” logic operation.

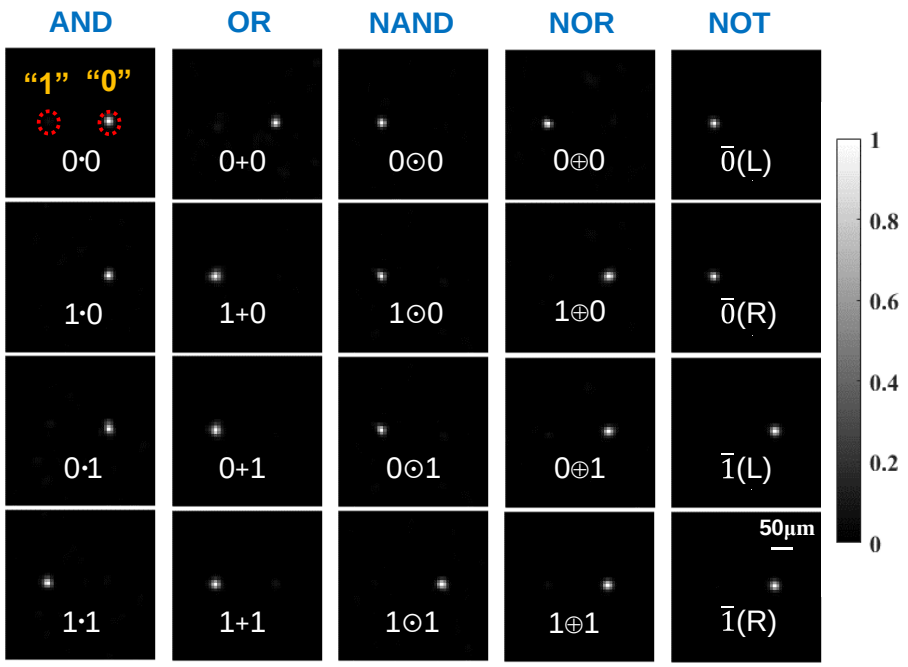

Fig. 5.10 Experimental results of different logic operations. Digits “0” and “1” marked in yellow in the first figure represent the logic states. Intensities are normalized to the maximum of each figure. “L” and “R” in the bracket mean the selected binary unit (0 or 1) is from the left column or on the right column, respectively, of the DMD. Please see Fig. 5.9a as an example, where 0(L) and 1(R) are chosen.

To further verify the feasibility and robustness of the proposed scheme, 20 sets of experiments based on the five basic logic functions (AND, OR, NOT, NAND, NOR) are performed and shown in Fig. 5.10. According to the inverse design, the desired focus intensity contrast ratios of logic operations 0•0, 1+1, 0⊙0, and 1⊕1 are 6dB. For other logic operations, the contrast ratios shall be infinity as long as the focal peak to background ratios are sufficiently large to suppress the speckle background and most of diffusive photons are focused onto designated regions. In experiment, the intensity contrast ratios are 7.5 dB, 7.3 dB, 8.2 dB, and 8.2 dB, respectively, for logic operations

0•0, 1+1, 0⊙0, and 1⊕1. These are slightly better than the designed contrast ratios, which may attribute to two aspects. First, the focal peak enhancement ratio is not uniform on the whole output plane for light from one subregion[175] and the wavefront intersection affects the intensity of two focuses with different efficiencies. As a result, two focuses originating from the same subregion have different focal intensities. Second, the focal peak enhancement ratios are also not the same at the same area on the output plane for different DMD subregions. As a consequence, other logic operations have decreased contrast ratios, which are merely more than 9.5 dB rather than infinity in the experiment. For example, for all "NOT" operations (the last column of Fig. 5.10), contrast ratios are larger than 13.9 dB. To further demonstrate the reliability of the proposed method, 200 pairs of areas on the output plane were chosen in experiment as the focuses formed by light from individual DMD subregions and to represent the binary "1" and "0" outputs. Statistics can be referred to Fig. 5.11.

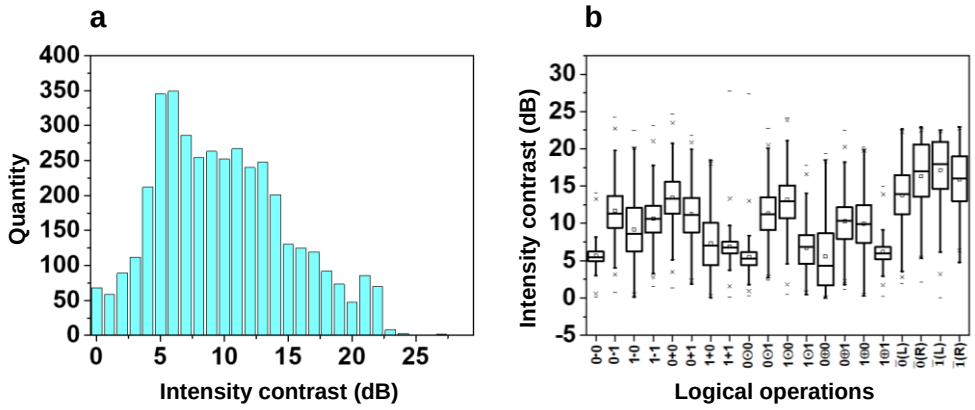

Fig. 5.11 200 pairs of areas on the output plane were chosen in experiment as the focuses formed by light from individual DMD subregions and to represent the logic "1" and "0" outputs. (a) Statistical distribution of intensity contrast of all logical operations (the total number is 200*20). The logic operation is invalid when the intensity contrast is zero. Intensity

contrasts are rounded down along the horizontal axis. (b) Distribution of intensity contrasts of certain type of logical operation from the 200 groups of data.

In order to further demonstrate the reliability of the proposed method, 200 pairs of areas on the output plane were chosen in experiment as the focuses formed by light from individual DMD subregions and to represent the logic "1" and "0" outputs (It contains 200 groups of data and each group contains 20 different logic operations). As shown in Fig. 5.11a, the number of logical operations with intensity contrast values below 3 dB are 216 (including the invalid sets), which is about 5.4% of the total operations (4,000). From Fig. 5.11b, the average intensity contrast values of all types of logical operations are over 5 dB except $0 \oplus 0$, which has an average value slightly below 5 dB.

5.4 Discussions and Conclusion

Thus far, the concept and the principle of diffusive optical logic have been described to achieve five basic logic operations with wavefront shaping. Experimental results have demonstrated the feasibility and robustness of the proposed method. A few more things need to be discussed herein.

It is emphasized that the proposed scheme can, in principle, directly construct all seven basic logic functions (including XOR and XAND that are not explored in this study). This can be done by changing the intensity of focus with a finer resolution; the focal intensity can be adjusted in a large range by blocking certain portion of the constructive channels, while the phase value maintains largely unchanged, as long as the remaining

channels are sufficient enough to make the focus to be in phase or opposite phase with the common reference. This method can also be used to improve the intensity contrast ratio as discussed in Fig. 5.10. Note that, however, it requires more accurate computation to determine the desired intensity and phase of each focus.

The current scheme can be extended for more functions, such as achieving multi-bit logic operations. It can be achieved by, for example, cascading multiple current logic gates in a design shown in Fig. 5.12. The DMD screen can be divided into a large number of subregions or control units to represent various logic gates and connection buttons. One logic gate is the basic block to achieve a group of basic logic operations as demonstrated in this study. Connection buttons contain three logic types “AND”, “OR” and “NOT” to connect adjacent logic gates to achieve cascaded function. For example, for logic operation “（0⊕0）+（1+0）“, there will be two logic gates, with one functioning as “0⊕0“ and the other as “1+0“, and one connection button to provide function “OR”. In operation, the corresponding control units on the DMD will display the pre-calculated wavefronts obtained with the proposed TM-based wavefront shaping method using an inverse design. A typical DMD has 1080×1920 pixels, allowing for extension towards complicated (including more functions and more bits) logic operations.

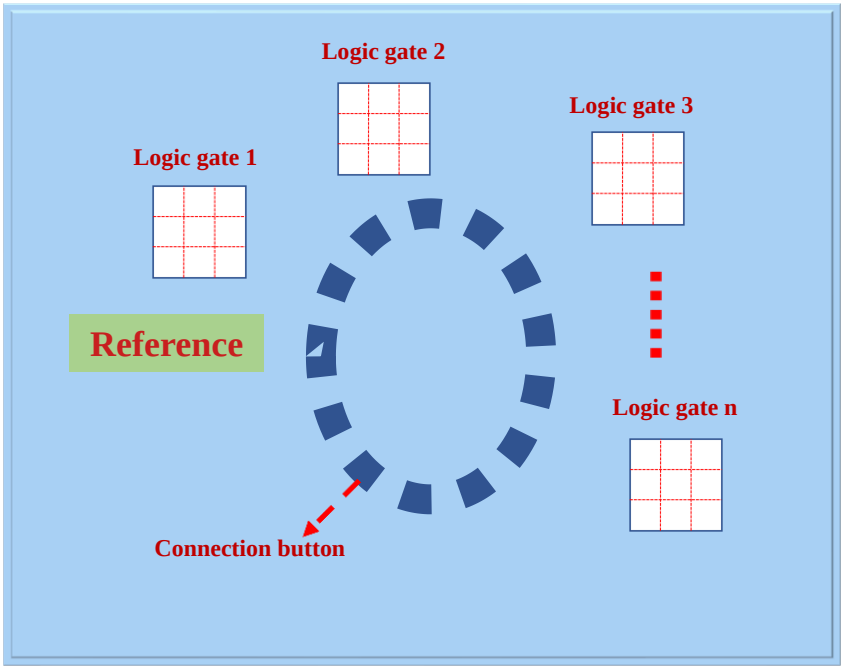

Fig. 5.12 Arrangement of the DMD for cascaded optical logic gates

In this work, the scattering medium is a ground glass diffuser. It has a TM of infinite dimension. In experiment, nine sub-TMs with dimension of 1024×40000 were used to realize the five basic optical logic gates (AND, OR, NOT, NAND, NOR) with all light from the DMD being shedding onto the ground glass. Therefore, the ground glass, in theory, can support many groups of such optical logic gates. Moreover, the extension will not considerably increase the complexity for TM measurement thanks to the inverse design approach. The other factor that needs to be consider is the pixel number of the DMD used in the study, which is 1080×1920. Thus, it can support up to 10 logic gates with the current experiment conditions. Or, if no pixels are binned to form mega pixels, this DMD, in principle, can support up to 220 logic gates. That said, multiple DMDs in combination or a DMD with more pixels can be used to achieve the mentioned large-scale cascaded optical logic gates. The dimension of the DMD, however, will not be a major bottleneck to the extension potential of this work, especially when the rapid

development of DMD or other spatial light modulators in the past two decades and in the near future is considered.

The inverse approach is a common strategy for the design of existing optical logic components, but it will encounter some limitations because of fabrication inaccuracy and environmental disturbance; packaging the whole system in a black box to be less sensitive or immune to perturbations is usually required. When the scene of application varies, new design and/or fabrication of components as well as system packaging might be necessary. For the proposed approach, when the system or the environment is altered, the issue can be solved by measuring the TM again, which currently costs 37 seconds in experiment and can be considerably shortened to less than 1 second. Such a reconfiguration capability is unmatched by any of existing optical logic schemes. Moreover, depending on applications, the ground glass diffuser can be replaced by other scattering media, such as a customized scattering chip, which provides a scenario to achieve chip-scale integration of multiple optical logic gates.

As just mentioned, currently the measurement of transmission matrix costs 37 seconds, which is mainly restricted by the working frame rate (500 Hz) of the camera used in the system. One of effective ways to shorten the duration of TM measurement is to adopt a faster detector, such as a photoelectric detector[61]. The significantly increased speed can also make it compatible for using a large size Hadamard matrix to improve the performance. To further improve the speed, a programmable laser may be used. In the

first solution, the laser consists of many point light sources that can be fast switched on or off independently. There is one-to-one correspondence between the subregions and the point light sources. In the other solution, there is a much faster programmable spatial switch which can be embedded into the laser to let the laser illuminate different groups of subregions independently.

The selection of areas on the output plane to present the logic states also matters. As known, the focal enhancement ratio pattern on the output plane is highly correlated with the intensity distribution profile of the speckle grains formed by the reference light[175]: at the dark grain spots, the focal enhancement ratio is low; at the bright grain spots, the focal enhancement ratio is high. This effect leads large variations among intensities of focuses formed in different areas on the output plane, which further affects the viability of the proposed logic operations. Therefore, cautiously selecting two bright grains as the spots of focuses can assure the robustness of the proposed logic operations. On other hand, several methods can be used to improve the success rate. For example, a super-pixel method can be adopted to achieve more uniform distribution of intensity of the resultant optical focuses by using the DMD as a phase modulation device[180]. Another method is to scan the incident laser beam so as to achieve maximum optical transmission through the scattering medium before the TM measurement[175].

To conclude, a diffusive optical logic (DOL) method based on transmission matrix wavefront shaping is proposed and demonstrated in this section. Light is first encoded

by a DMD with pre-calculated patterns and then it is decoded by a ground glass diffuser to output logical states. Choosing a common reference speckle field for light from nine DMD subregions, the feasibility and robustness of five basic logic functions (AND, OR, NOT, NAND, NOR) have been experimentally demonstrated. Whilst a lot can be further improved, the proposed method achieves multiple logic functions on a single unit and simplifies the manufacturing process. More importantly it empowers reconfigurability and scalability to the design and construction of optical logic gates, which is unmatched by any of existing implementations in the field. Last but not the least, the method can be further engineered and inspire many exciting applications, such as intelligent and reconfigurable all-optical or opto–electronic large-scale computing.

Supplementary material of the calculation process in Fig. 5.8a

Table 1: Desired phases and intensities of focuses from each DMD subregion in an inverse design. Characters "a" to "r" are the required electric field amplitudes of focuses at the focus areas representing logic states "0" and "1". If the character is negative, the focus is in opposite phase with the reference; otherwise, the focus is in phase with the reference.

Active unit / Focus area	0 (left)	1 (left)	0 (right)	1 (right)	AND	OR	NOT	NAND	NOR
"0"	a	b	c	d	e	f	g	h	i
"1"	j	k	l	m	n	o	p	q	r

Characters "a" to "r" represent the electric field amplitude of focuses generated by the

nine DMD subregions/control units. The combination of different groups can act as different logic operations. And their relationship should obey the below inequations:

$$
\begin{array}{ll}
|a+c+e| \geq 2*|j+l+n| & |a+c+f| \geq 2*|j+l+o| \\
|a+d+e| \geq 2*|j+m+n| & 2*|a+d+f| \leq |j+m+o| \\
|b+c+e| \geq 2*|k+l+n| & 2*|b+c+f| \leq |k+l+o| \\
2*|b+d+e| \leq |k+m+n| & 2*|b+d+f| \leq |k+m+o|
\end{array}
$$

$$
\begin{array}{lll}
2*|a+c+h| \leq |j+l+q| & 2*|a+c+i| \leq |j+l+r| & 2*|a+g| \leq |j+p| \\
2*|a+d+h| \leq |j+m+q| & |a+d+i| \geq 2*|j+m+r| & |b+g| \geq 2*|k+p| \\
2*|b+c+h| \leq |k+l+q| & |b+c+i| \geq 2*|k+l+r| & 2*|c+g| \leq |l+p| \\
|b+d+h| \geq 2*|k+m+q| & |b+d+i| \geq 2*|k+m+r| & |d+g| \geq 2*|m+p|
\end{array}
\tag{5.9}
$$

If a character is negative, the phase of the corresponding focus is π (in opposite phase with the reference); if a character is positive, the phase of the corresponding focus is 0 (in phase with the reference). Threshold setting: if logic output is “0”, the absolute amplitude value of the synthetic field in the area of logical state “0” should be twice larger than that in the area of logical state “1” and vice versa.

Chapter 6: Summary and future work

In this thesis, the capability of wavefront engineering was demonstrated and optimized to achieve optical focusing in the existence of scattering. Its potentials were also explored towards more complex functions, such as image transmission with edge enhancement and diffusive optical logic gates, which are otherwise challenging or even impossible to achieve. Herein, let us summarize the major achievements in this thesis.

In Chapter 2, the system of DOPC was simplified with phase rectification method and further improved the focusing efficiency with an embedded Michelson interferometer to calibrate the SLM curvature and the misalignment of SLM-camera phase conjugation module. Based on this plain yet robust DOPC set up, two promising applications were proposed and discussed in Chapters 3 and 4.

In Chapter 3, optical focusing inside scattering media was achieved by combining the DOPC system and a magnetically controlled module. Opto-magnetic microspheres packaged with organic membranes were controlled to move inside scattering media by an external magnetic field, serving as internal guidestars to perturbate the diffusive light field. It has advantages in two aspects. Firstly, the perturbation induced by the microspheres and hence optical focusing in a relatively large field-of-view can be achieved by scanning the magnetic field externally. Secondly, the opto-magnetic

microspheres packaged with organic membranes can be combined with biological or chemical means to serve as a carrier, showing potentials for enhanced targeted drug delivery as well as imaging and photoablation of angiogenic vessels in tumors.

In Chapter 4, tunable edge enhancement of optical objects through scattering media was achieved with this DOPC system simply by adjusting the intensity ratio between the reference and sample beams. To the best of our knowledge, it is the first time that an edge enhancement effect was demonstrated in the existence of strong scattering. Quantitatively, the enhancement index (*EI*) and enhancement to noise ratio (*ENR*) of the edges can be enhanced by ~8.5 and ~263 times, respectively. Edge enhancement has wide applications in optical imaging and medical image processing, such as tumor boundary detection and cell morphology identification, as perception of edge is one of the keys to identify and comprehend the contents of an image.

In Chapter 5, the scope of wavefront shaping was extended in optical computation. Diffusive optical logic (DOL) empowered by transmission matrix-based wavefront shaping was proposed to achieve reconfigurable and multifunctional logic operations on one platform: light was firstly encoded by a DMD displayed with a precalculated wavefront and then the encoded light was diffused and decoded by a scattering medium to form different logical states. The output logic states were recognized by the intensity contrast between two pre-selected areas representing the logical states “0” and “1” on the output plane. This is achieved by interference among light fields generated by

different subregions on the DMD. As a proof of concept, five basic logic functions (AND, OR, NOT, NAND, NOR) were demonstrated through experiment, with a ground glass as the scattering medium. As the transmission matrix of strong scattering media has huge ranks and provides enormous degrees of freedom, the proposed method empowers reconfigurability and scalability to the design and construction of optical logic gates, and in the meantime simplifies the manufacturing process.

Last but not the least, let me take the opportunity to discuss the understanding of wavefront engineering and put forward my points of the potential development in this field. Wavefront engineering was used in three aspects from optical focusing, image transmission, to optical logic gate in this thesis, and hence the limitations and future development of the work proposed in this thesis are also included in the following discussion. Wavefront shaping and optical phase conjugation are both relatively new (both were proposed or introduced in the context of biomedical optics around 2007-2008), but they have witnessed rapid and encouraging development in the last decade. As discussed in Chapter 1, researchers have made intense efforts to enable wavefront shaping and optical phase conjugation for real applications especially from the aspects of optimization speed and modulation efficiency. That said, their widespread use is still limited due to different reasons. For wavefront shaping, it requires a large number of iterative measurements in order to find the optimum phase compensation, which shall be completed within the decorrelation time of the medium. It is thus very challenging with living biological tissue, whose optical decorrelation time is on the order of

milliseconds or even less due to physiological motions like breathing and heart beating. The updating speeds of commercial spatial light modulators available on the market are not fast enough to finish all these measurements within such a short time window. Most recently, however, researchers have developed an ultrafast home-made SLM with an update speed of 350 kHz and achieved an unprecedented optimization speed of 2.4 ms, as discussed in Chapter 1. This indicates the feasibility of fast wavefront shaping towards real applications, and we believe in the near future new modulation schemes with a satisfactory updating speed will be manufactured. By then, wavefront shaping will undergo ever-increasing development, which may inspire a lot more revolutionary high-resolution optical applications in deep biological tissue.

The situation is quite different for optical phase conjugation, where the optimization speed is not the major obstacle towards biomedical applications. The real challenge is associated with the inherent feature of time-reversal: the phase conjugated light is time-reversed and transmit along the opposite direction of the sample beam. That means, diffusive light can only be focused onto where it is not diffusive yet (e.g., before it enters the scattering medium) or a virtual point source created by internal guide stars that generates the portions of light being time-reversed. This limits the location and/or the strength of the optical focusing, no matter the optical phase conjugation setup is in transmission or reflection configuration (if the light incidence and the PCM are on the same side the scattering medium, it is in reflection mode; otherwise, it is in transmission mode). Therefore, in the past few years, applications of optical phase conjugation

beyond optical focusing and imaging are rarely seen.

It also should be noted that in wavefront shaping, wavefronts of diffusive light can be modulated with much less constraints than they are in optical phase conjugation. Therefore, in the past decade researchers have extended wavefront shaping in many other fields beyond biomedicine, which are summarized herein into two categories. In the first category, photons are only scattered when they transmit inside scattering media (assuming no or weak optical absorption). Researchers can use wavefront shaping to modulate some inherent properties (excluding wavelength) of light, such as polarization, phase, and intensity, and furtherly reconfigure the scattering medium to implement specific functions. For all these, the transmission matrix of the scattering medium needs to be deciphered as it always requires an accurate modulation of the input field to obtain a desired output field. For example, Xiong *et al.* demonstrated to obtain an arbitrary polarization state of individual output channel in a multimode fiber (MMF)[181], and Matthès *et al.* shaped a scattering medium into universal linear operators[174]. In Chapter 5, a ground glass was reconfigured to support multiple logic operations. In the second category, when diffusive light travels inside scattering media, some photons are converted into new photons of a different wavelength rather than being scattered. Wavefront shaping, in this scene, can be used to modulate the integrated conversion efficiency. For example, Raman scattering is part of the innate quality of matter: the wavelength of photons will shift when they interact with vibratory molecules inside media. Tzang *et al.* presented stimulated Raman scattering enhancement and

suppression in a GRIN fiber with iterative wavefront shaping[182]. It is shown when the medium is doped with rare-earth elements, these elements absorb photons and emit new photons of a distinctive wavelength. Wei *et al.* proposed to optimize the output power, mode profile, and optical spectrum of the fiber laser in a ytterbium-doped MMF assisted by iterative wavefront shaping[183]. These explorations demonstrate that wavefront shaping is a versatile tool to modulate different dimensions of the diffused light for information manipulation.

In summary, the advance of industrial technology and in-depth exploration will enable wavefront shaping and digital optical phase conjugation to be promising and powerful tools in many research fields, especially for some interdisciplinary fields, in the near future.

References

1 Denk, W., Strickler, J. H. & Webb, W. W. Two-photon laser scanning fluorescence microscopy. *Science* **248**, 73-76 (1990).

2 Huang, X., Qian, W., El-Sayed, I. H. & El-Sayed, M. A. The potential use of the enhanced nonlinear properties of gold nanospheres in photothermal cancer therapy. *Lasers in Surgery and Medicine: The Official Journal of the American Society for Laser Medicine and Surgery* **39**, 747-753 (2007).

3 Booth, M. J., Neil, M. A., Juškaitis, R. & Wilson, T. Adaptive aberration correction in a confocal microscope. *Proceedings of the National Academy of Sciences* **99**, 5788-5792 (2002).

4 Nwaneshiudu, A. *et al.* Introduction to confocal microscopy. *Journal of Investigative Dermatology* **132**, 1-5 (2012).

5 Tearney, G. J., Webb, R. H. & Bouma, B. E. Spectrally encoded confocal microscopy. *Opt. Lett.* **23**, 1152-1154 (1998).

6 Chen, B. *et al.* Rapid volumetric imaging with Bessel-Beam three-photon microscopy. *Biomed Opt Express* **9**, 1992-2000 (2018).

7 Helmchen, F. & Denk, W. Deep tissue two-photon microscopy. *Nature methods* **2**, 932-940 (2005).

8 Dunn, K. W., Sandoval, R. M., Kelly, K. J., Dagher, P. C. & Molitoris, B. A. J. A. J. o. P. C. P. Functional studies of the kidney of living animals using multicolor two-photon microscopy. **283**, C905-916 (2002).

9 Rice, W. L., Kaplan, D. L. & Georgakoudi, I. Two-photon microscopy for non-invasive, quantitative monitoring of stem cell differentiation. *PloS one* **5**, e10075 (2010).

10 Heine, J. *et al.* Adaptive-illumination STED nanoscopy. *Proceedings of the National Academy of Sciences* **114**, 9797-9802 (2017).

11 Hell, S. W. & Wichmann, J. Breaking the diffraction resolution limit by stimulated emission: stimulated-emission-depletion fluorescence microscopy. *Opt. Lett.* **19**, 780-782 (1994).

12 Dyba, M., Jakobs, S. & Hell, S. W. Immunofluorescence stimulated emission depletion microscopy. *Nature biotechnology* **21**, 1303-1304 (2003).

13 Kellner, R. R., Baier, C. J., Willig, K. I., Hell, S. W. & Barrantes, F. J. Nanoscale organization of nicotinic acetylcholine receptors revealed by stimulated emission depletion microscopy. *Neuroscience* **144**, 135-143 (2007).

14 Willig, K. I., Rizzoli, S. O., Westphal, V., Jahn, R. & Hell, S. W. STED microscopy reveals that synaptotagmin remains clustered after synaptic vesicle exocytosis. *Nature* **440**, 935-939 (2006).

15 Ji, C.-k. *et al.* Micrometer-resolution in-fiber OCT probe with tunable working distance. *Optics express* **24**, 19814-19823 (2016).

16 Huang, D. *et al.* Optical coherence tomography. *science* **254**, 1178-1181 (1991).

17 Fercher, A. F. Optical coherence tomography. *Journal of Biomedical Optics* **1**, 157-173

(1996).
18 Fercher, A. F., Drexler, W., Hitzenberger, C. K. & Lasser, T. Optical coherence tomography-principles and applications. *Reports on progress in physics* **66**, 239 (2003).
19 Hee, M. R. *et al.* Optical coherence tomography of the human retina. *Archives of ophthalmology* **113**, 325-332 (1995).
20 Morgner, U. *et al.* Spectroscopic optical coherence tomography. *Opt. Lett.* **25**, 111-113 (2000).
21 Liu, T.-I. *et al.* Observing the cell in its native state: Imaging subcellular dynamics in multicellular organisms. **360**, 1392 (2018).
22 Weber, M., Mickoleit, M. & Huisken, J. Light sheet microscopy. *Methods in cell biology* **123**, 193-215 (2014).
23 Pitrone, P. G. *et al.* OpenSPIM: an open-access light-sheet microscopy platform. *nature methods* **10**, 598-599 (2013).
24 Keller, P. J. & Dodt, H.-U. Light sheet microscopy of living or cleared specimens. *Current opinion in neurobiology* **22**, 138-143 (2012).
25 Horton, N. G. *et al.* In vivo three-photon microscopy of subcortical structures within an intact mouse brain. *Nature photonics* **7**, 205-209 (2013).
26 Ouzounov, D. G. *et al.* In vivo three-photon imaging of activity of GCaMP6-labeled neurons deep in intact mouse brain. *Nat Methods* **14**, 388-390, doi:10.1038/nmeth.4183 (2017).
27 Wang, T. *et al.* Three-photon imaging of mouse brain structure and function through the intact skull. *Nat Methods* **15**, 789-792 (2018).
28 Wang, T. & Xu, C. Three-photon neuronal imaging in deep mouse brain. *Optica* **7**, 947-960 (2020).
29 Booth, M. J. Wavefront sensorless adaptive optics for large aberrations. *Opt. Lett.* **32**, 5-7 (2007).
30 Liu, R., Li, Z., Marvin, J. S. & Kleinfeld, D. Direct wavefront sensing enables functional imaging of infragranular axons and spines. *Nat Methods* **16**, 615-618 (2019).
31 Park, J. H., Kong, L., Zhou, Y. & Cui, M. Large-field-of-view imaging by multi-pupil adaptive optics. *Nat Methods* **14**, 581-583 (2017).
32 Zurauskas, M. *et al.* IsoSense: frequency enhanced sensorless adaptive optics through structured illumination. *Optica* **6**, 370-379 (2019).
33 Ji, N., Milkie, D. E. & Betzig, E. Adaptive optics via pupil segmentation for high-resolution imaging in biological tissues. *Nature methods* **7**, 141-147 (2010).
34 Booth, M. J. Adaptive optics in microscopy. *Philosophical Transactions of the Royal Society of London A: Mathematical, Physical and Engineering Sciences* **365**, 2829-2843 (2007).
35 Débarre, D., Botcherby, E. J., Booth, M. J. & Wilson, T. Adaptive optics for structured illumination microscopy. *Optics Express* **16**, 9290-9305, doi:10.1364/OE.16.009290 (2008).
36 Wang, C. *et al.* Multiplexed aberration measurement for deep tissue imaging in vivo. *Nat Methods* **11**, 1037-1040, doi:10.1038/nmeth.3068 (2014).
37 Park, J.-H., Kong, L., Zhou, Y. & Cui, M. Large-field-of-view imaging by multi-pupil adaptive optics. *Nature Methods* **14**, 581-583 (2017).
38 Goodman, J. W. *Speckle phenomena in optics: theory and applications*. (Roberts and Company Publishers, 2007).

39 Denk, W., Strickler, J. & Webb, W. J. S. Two-photon laser scanning fluorescence microscopy. **248**, 73-76.
40 Qureshi, M. M. *et al.* In vivo study of optical speckle decorrelation time across depths in the mouse brain. *Biomedical optics express* **8**, 4855-4864 (2017).
41 McDowell, E. J. *Low optical signal detection in biological materials: SNR considerations and novel techniques*. (California Institute of Technology, 2010).
42 Raulin, C. & Karsai, S. *Laser and IPL technology in dermatology and aesthetic medicine*. (Springer Science & Business Media, 2011).
43 Wang, L. V. & Wu, H.-i. *Biomedical optics: principles and imaging*. (John Wiley & Sons, 2012).
44 Hulst, H. C. & van de Hulst, H. C. *Light scattering by small particles*. (Courier Corporation, 1981).
45 Diaspro, A. *Confocal and two-photon microscopy: foundations, applications, and advances*. Vol. 1 (Wiley-Liss New York, 2002).
46 Tuchin, V. V. & Tuchin, V. *Tissue optics: light scattering methods and instruments for medical diagnosis*. Vol. 13 (SPIE press Bellingham, 2007).
47 Freund, I., Rosenbluh, M. & Feng, S. Memory effects in propagation of optical waves through disordered media. *Physical review letters* **61**, 2328 (1988).
48 Feng, S., Kane, C., Lee, P. A. & Stone, A. D. Correlations and fluctuations of coherent wave transmission through disordered media. *Phys. Rev. Lett.* **61**, 834 (1988).
49 Lai, P., Wang, L., Tay, J. W. & Wang, L. V. Photoacoustically guided wavefront shaping for enhanced optical focusing in scattering media. *Nature Photon.* **9**, 126-132 (2015).
50 Conkey, D. B., Brown, A. N., Caravaca-Aguirre, A. M. & Piestun, R. Genetic algorithm optimization for focusing through turbid media in noisy environments. *Optics express* **20**, 4840-4849 (2012).
51 Yu, Z., Li, H. & Lai, P. Wavefront Shaping and Its Application to Enhance Photoacoustic Imaging. *Applied Sciences* **7**, 1320 (2017).
52 Yu, H. *et al.* Recent advances in wavefront shaping techniques for biomedical applications. *Current Applied Physics* **15**, 632-641 (2015).
53 Chaigne, T. *et al.* Controlling light in scattering media non-invasively using the photoacoustic transmission matrix. *Nature Photonics* **8**, 58-64 (2014).
54 Bossy, E. & Gigan, S. Photoacoustics with coherent light. *Photoacoustics* **4**, 22-35 (2016).
55 Yaqoob, Z., Psaltis, D., Feld, M. S. & Yang, C. Optical phase conjugation for turbidity suppression in biological samples. *Nature photonics* **2**, 110-115 (2008).
56 Si, K., Fiolka, R. & Cui, M. Fluorescence imaging beyond the ballistic regime by ultrasound-pulse-guided digital phase conjugation. *Nature photonics* **6**, 657-661 (2012).
57 Vellekoop, I. M., Cui, M. & Yang, C. Digital optical phase conjugation of fluorescence in turbid tissue. *Applied physics letters* **101**, 081108 (2012).
58 Vellekoop, I. M. & Mosk, A. Focusing coherent light through opaque strongly scattering media. *Opt. Lett.* **32**, 2309-2311 (2007).
59 Choi, W., Mosk, A. P., Park, Q.-H. & Choi, W. Transmission eigenchannels in a disordered medium. *Physical Review B* **83**, 134207 (2011).
60 Popoff, S. *et al.* Measuring the transmission matrix in optics: an approach to the study and control of light propagation in disordered media. *Physical review letters* **104**, 100601

(2010).
61 Yu, H., Lee, K. & Park, Y. Ultrahigh enhancement of light focusing through disordered media controlled by mega-pixel modes. *Opt. Express* **25**, 8036-8047 (2017).
62 Zahra, F. *et al.* Simulated annealing optimization in wavefront shaping controlled transmission. *Applied Optics* **57**, 6233 (2018).
63 Biqi Li *et al.* Shaping the Wavefront of Incident Light with a Strong Robustness Particle Swarm Optimization Algorithm. *Chinese Physics Letters* **35**, 15-18 (2018).
64 Wang, Z.-Q. *et al.* Bat algorithm-enabled binary optimization for scattered light focusing. *Applied Physics Express* **12**, 102002 (2019).
65 Blochet, B., Bourdieu, L. & Gigan, S. Focusing light through dynamical samples using fast continuous wavefront optimization. *Opt. Lett.* **42**, 4994-4997 (2017).
66 Caravaca-Aguirre, A. M., Niv, E., Conkey, D. B. & Piestun, R. Real-time resilient focusing through a bending multimode fiber. *Optics express* **21**, 12881-12887 (2013).
67 Tzang, O. *et al.* Wavefront shaping in complex media with a 350 kHz modulator via a 1D-to-2D transform. *Nature Photonics* **13**, 788-793 (2019).
68 Katz, O., Small, E., Bromberg, Y. & Silberberg, Y. Focusing and compression of ultrashort pulses through scattering media. *Nature photonics* **5**, 372-377 (2011).
69 Tay, J. W., Lai, P., Suzuki, Y. & Wang, L. V. Ultrasonically encoded wavefront shaping for focusing into random media. *Scientific reports* **4**, 3918 (2014).
70 Ntziachristos, V. & Razansky, D. Molecular imaging by means of multispectral optoacoustic tomography (MSOT). *Chemical reviews* **110**, 2783-2794 (2010).
71 Wang, L. V. & Hu, S. Photoacoustic tomography: in vivo imaging from organelles to organs. *Science* **335**, 1458-1462 (2012).
72 Beard, P. Biomedical photoacoustic imaging. *Interface focus* **1**, 602-631 (2011).
73 Kruger, R. A. Photoacoustic ultrasound. *Medical physics* **21**, 127-131 (1994).
74 Karabutov, A., Podymova, N. & Letokhov, V. Time-resolved laser optoacoustic tomography of inhomogeneous media. *Applied Physics B* **63**, 545-563 (1996).
75 Oraevsky, A. A., Jacques, S. L. & Tittel, F. K. Measurement of tissue optical properties by time-resolved detection of laser-induced transient stress. *Appl. Optics* **36**, 402-415 (1997).
76 Mosk, A. P., Lagendijk, A., Lerosey, G. & Fink, M. Controlling waves in space and time for imaging and focusing in complex media. *Nature photonics* **6**, 283-292 (2012).
77 Conkey, D. B., Caravaca-Aguirre, A. M. & Piestun, R. High-speed scattering medium characterization with application to focusing light through turbid media. *Optics express* **20**, 1733-1740 (2012).
78 Conkey, D. B. *et al.* Super-resolution photoacoustic imaging through a scattering wall. *Nature communications* **6**, 1-7 (2015).
79 Caravaca-Aguirre, A. M. *et al.* High contrast three-dimensional photoacoustic imaging through scattering media by localized optical fluence enhancement. *Optics express* **21**, 26671-26676 (2013).
80 Kong, F. *et al.* Photoacoustic-guided convergence of light through optically diffusive media. *Optics letters* **36**, 2053-2055 (2011).
81 Chaigne, T., Gateau, J., Katz, O., Bossy, E. & Gigan, S. Light focusing and two-dimensional imaging through scattering media using the photoacoustic transmission matrix with an ultrasound array. *Opt. Lett.* **39**, 2664-2667 (2014).

82 Conkey, D. B. *et al.* Super-resolution photoacoustic imaging through a scattering wall. *Nat Commun* **6**, 7902 (2015).
83 Yariv, A. Phase conjugate optics and real-time holography. *IEEE Journal of Quantum Electronics* **14**, 650-660 (1978).
84 Pepper, D. M. & Yariv, A. Compensation for phase distortions in nonlinear media by phase conjugation. *Opt. Lett.* **5**, 59-60 (1980).
85 Kwong, S. K., Rakuljic, G. A. & Yariv, A. Real time image subtraction and ''exclusive or'' operation using a self-pumped phase conjugate mirror. *Applied physics letters* **48**, 201-203 (1986).
86 Yariv, A. Three-dimensional pictorial transmission in optical fibers. *Applied Physics Letters* **28**, 88-89 (1976).
87 Yariv, A. On transmission and recovery of three-dimensional image information in optical waveguides. *JOSA* **66**, 301-306 (1976).
88 Yariv, A. & Pepper, D. M. Amplified reflection, phase conjugation, and oscillation in degenerate four-wave mixing. *Opt. Lett.* **1**, 16-18 (1977).
89 Jensen, S. M. & Hellwarth, R. W. Observation of the time - reversed replica of a monochromatic optical wave. *Applied Physics Letters* **32**, 166-168 (1978).
90 Bloom, D. M. & Bjorklund, G. C. Conjugate wave - front generation and image reconstruction by four-wave mixing. *Applied Physics Letters* **31**, 592-594 (1977).
91 Ma, C., Xu, X., Liu, Y. & Wang, L. V. Time-reversed adapted-perturbation (TRAP) optical focusing onto dynamic objects inside scattering media. *Nature photonics* **8**, 931-936 (2014).
92 Liu, Y. *et al.* Optical focusing deep inside dynamic scattering media with near-infrared time-reversed ultrasonically encoded (TRUE) light. *Nature communications* **6**, 5904 (2015).
93 Xu, X., Liu, H. & Wang, L. V. Time-reversed ultrasonically encoded optical focusing into scattering media. *Nature photonics* **5**, 154-157 (2011).
94 Judkewitz, B., Wang, Y. M., Horstmeyer, R., Mathy, A. & Yang, C. Speckle-scale focusing in the diffusive regime with time reversal of variance-encoded light (TROVE). *Nature Photonics* **7**, 300-305 (2013).
95 Tseng, S. H. & Yang, C. 2-D PSTD simulation of optical phase conjugation for turbidity suppression. *Optics express* **15**, 16005-16016 (2007).
96 Wang, Y. M., Judkewitz, B., DiMarzio, C. A. & Yang, C. Deep-tissue focal fluorescence imaging with digitally time-reversed ultrasound-encoded light. *Nature communications* **3**, 928 (2012).
97 Shen, Y., Liu, Y., Ma, C. & Wang, L. V. Sub-Nyquist sampling boosts targeted light transport through opaque scattering media. *Optica* **4**, 97-102 (2017).
98 Wang, Y. M., Judkewitz, B., Dimarzio, C. A. & Yang, C. Deep-tissue focal fluorescence imaging with digitally time-reversed ultrasound-encoded light. *Nat Commun* **3**, 928 (2012).
99 Wang, D. *et al.* Focusing through dynamic tissue with millisecond digital optical phase conjugation. *Optica* **2**, 728-735 (2015).
100 Liu, Y., Ma, C., Shen, Y., Shi, J. & Wang, L. V. Focusing light inside dynamic scattering media with millisecond digital optical phase conjugation. *Optica* **4**, 280-288 (2017).
101 Cheng, Z., Yang, J. & Wang, L. V. Single-shot time-reversed optical focusing into and

through scattering media. *ACS Photonics* **7**, 2871-2877 (2020).

102 Lai, P., Suzuki, Y., Xu, X. & Wang, L. V. Focused fluorescence excitation with time-reversed ultrasonically encoded light and imaging in thick scattering media. *Laser physics letters* **10**, 075604 (2013).

103 Hsieh, C.-L., Pu, Y., Grange, R., Laporte, G. & Psaltis, D. Imaging through turbid layers by scanning the phase conjugated second harmonic radiation from a nanoparticle. *Optics express* **18**, 20723-20731 (2010).

104 Torras-Rosell, A., Barrera-Figueroa, S. & Jacobsen, F. Sound field reconstruction using acousto-optic tomography. *The Journal of the Acoustical Society of America* **131**, 3786-3793 (2012).

105 Lai, P., Xu, X., Liu, H. & Wang, L. V. Time-reversed ultrasonically encoded optical focusing in biological tissue. *Journal of Biomedical Optics* **17**, 0305061-0305063 (2012).

106 Zhou, E. H., Ruan, H., Yang, C. & Judkewitz, B. Focusing on moving targets through scattering samples. *Optica* **1**, 227-232 (2014).

107 Ruan, H., Jang, M. & Yang, C. Optical focusing inside scattering media with time-reversed ultrasound microbubble encoded light. *Nat Commun* **6**, 8968 (2015).

108 Ruan, H. *et al.* Deep tissue optical focusing and optogenetic modulation with time-reversed ultrasonically encoded light. *Science advances* **3**, eaao5520 (2017).

109 Ma, C., Zhou, F., Liu, Y. & Wang, L. V. Single-exposure optical focusing inside scattering media using binarized time-reversed adapted perturbation. *Optica* **2**, 869-876 (2015).

110 Shen, Y., Liu, Y., Ma, C. & Wang, L. V. Focusing light through scattering media by full-polarization digital optical phase conjugation. *Opt. Lett.* **41**, 1130-1133 (2016).

111 Shen, Y., Liu, Y., Ma, C. & Wang, L. V. Focusing light through biological tissue and tissue-mimicking phantoms up to 9.6 cm in thickness with digital optical phase conjugation. *Journal of biomedical optics* **21**, 085001 (2016).

112 Cui, M. & Yang, C. Implementation of a digital optical phase conjugation system and its application to study the robustness of turbidity suppression by phase conjugation. *Optics express* **18**, 3444-3455 (2010).

113 Yang, J., Shen, Y., Liu, Y., Hemphill, A. S. & Wang, L. V. Focusing light through scattering media by polarization modulation based generalized digital optical phase conjugation. *Applied physics letters* **111**, 201108 (2017).

114 Jang, M., Ruan, H., Zhou, H., Judkewitz, B. & Yang, C. Method for auto-alignment of digital optical phase conjugation systems based on digital propagation. *Optics express* **22**, 14054-14071 (2014).

115 Azimipour, M., Atry, F. & Pashaie, R. Calibration of digital optical phase conjugation setups based on orthonormal rectangular polynomials. *Applied optics* **55**, 2873-2880 (2016).

116 Hillman, T. *et al.* in *Asia Communications and Photonics Conference.* AF1J. 2 (Optical Society of America).

117 Fournel, T. & Javidi, B. *Information optics and photonics: algorithms, systems, and applications*. (Springer Science & Business Media, 2010).

118 Yang, J., Qiu, L., Zhao, W., Shao, R. & Li, Z. Measuring the lens focal length by laser reflection-confocal technology. *Applied Optics* **52**, 3812-3817, doi:10.1364/AO.52.003812 (2013).

119 Shikinami, Y. & Okuno, M. Bioresorbable devices made of forged composites of

hydroxyapatite (HA) particles and poly-L-lactide (PLLA): Part I. Basic characteristics. *Biomaterials* **20**, 859-877 (1999).

120 Jang, M. *et al.* Relation between speckle decorrelation and optical phase conjugation (OPC)-based turbidity suppression through dynamic scattering media: a study on in vivo mouse skin. *Biomedical optics express* **6**, 72-85 (2015).

121 Cui, M., McDowell, E. J. & Yang, C. An in vivo study of turbidity suppression by optical phase conjugation (TSOPC) on rabbit ear. *Optics Express* **18**, 25-30 (2010).

122 Ruan, H. *et al.* Focusing light inside scattering media with magnetic-particle-guided wavefront shaping. *Optica* **4**, 1337-1343 (2017).

123 Ge, H. *et al.* in *Asia-Pacific Optical and Wireless Communications* Vol. 5280 777-784 (SPIE, 2004).

124 Jesacher, A., Furhapter, S., Bernet, S. & Ritsch-Marte, M. Shadow effects in spiral phase contrast microscopy. *Phys Rev Lett* **94**, 233902 (2005).

125 Nisthula, P. & Yadhu, R. A novel method to detect bone cancer using image fusion and edge detection. *International Journal of Engineering and Computer Science* **2**, 2012-2018 (2013).

126 Qadir, F., Peer, M. & Khan, K. Efficient edge detection methods for diagnosis of lung cancer based on two-dimensional cellular automata. *Advances in Applied Science Research* **3**, 2050-2058 (2012).

127 Diwakar, M., Patel, P. K. & Gupta, K. in *2013 International Conference on Advances in Computing, Communications and Informatics.* 53-59 (IEEE).

128 Lu, D. *et al.* in *2011 IEEE International Conference on Information and Automation.* 343-348 (IEEE).

129 Zernike, F. Phase contrast, a new method for the microscopic observation of transparent objects. *Physica* **9**, 686-698 (1942).

130 Zhu, T. *et al.* Plasmonic computing of spatial differentiation. *Nature communications* **8**, 15391 (2017).

131 Grossmann, A. in *Stochastic processes in physics and engineering* 149-157 (Springer, 1988).

132 Kohlmann, K. Corner detection in natural images based on the 2-D Hilbert transform. *Signal Processing* **48**, 225-234 (1996).

133 Ritsch-Marte, M. Orbital angular momentum light in microscopy. *Philosophical Transactions of the Royal Society A: Mathematical, Physical and Engineering Sciences* **375**, 20150437 (2017).

134 Qiu, X. D., Li, F. S., Zhang, W. H., Zhu, Z. H. & Chen, L. X. Spiral phase contrast imaging in nonlinear optics: seeing phase objects using invisible illumination. *Optica* **5**, 208-212 (2018).

135 Liu, S.-K. *et al.* Up-conversion imaging processing with field-of-view and edge enhancement. *Physical Review Applied* **11**, 044013 (2019).

136 Fürhapter, S., Jesacher, A., Bernet, S. & Ritsch-Marte, M. Spiral phase contrast imaging in microscopy. *Optics Express* **13**, 689-694 (2005).

137 Feinberg, J. Real-time edge enhancement using the photorefractive effect. *Opt. Lett.* **5**, 330-332 (1980).

138 Huignard, J. & Herriau, J. Real-time coherent object edge reconstruction with Bi 12 SiO

20 crystals. *Applied optics* **17**, 2671-2672 (1978).
139 White, J. O. & Yariv, A. in *Landmark Papers On Photorefractive Nonlinear Optics* 455-457 (World Scientific, 1995).
140 Guo, C.-S., Han, Y.-J., Xu, J.-B. & Ding, J. Radial Hilbert transform with Laguerre-Gaussian spatial filters. *Opt. Lett.* **31**, 1394-1396 (2006).
141 Zhou, Y., Feng, S., Nie, S., Ma, J. & Yuan, C. Image edge enhancement using Airy spiral phase filter. *Optics express* **24**, 25258-25268 (2016).
142 Ding, Z., Ren, H., Zhao, Y., Nelson, J. S. & Chen, Z. High-resolution optical coherence tomography over a large depth range with an axicon lens. *Opt. Lett.* **27**, 243-245 (2002).
143 Lai, P., Xu, X., Liu, H., Suzuki, Y. & Wang, L. V. Reflection-mode time-reversed ultrasonically encoded optical focusing into turbid media. *Journal of Biomedical Optics* **16**, 080505 (2011).
144 Park, J.-H., Yu, Z., Lee, K., Lai, P. & Park, Y. Perspective: Wavefront shaping techniques for controlling multiple light scattering in biological tissues: Toward in vivo applications. *APL Photonics* **3**, 100901 (2018).
145 Liu, H., Xu, X., Lai, P. & Wang, L. V. Time-reversed ultrasonically encoded optical focusing into tissue-mimicking media with thickness up to 70 mean free paths. *Journal of Biomedical Optics* **16**, 086009 (2011).
146 Yu, Z. *et al.* Implementation of digital optical phase conjugation with embedded calibration and phase rectification. *Scientific reports* **9**, 1537 (2019).
147 Yu, Z. *et al.* Time-reversed magnetically controlled perturbation (TRMCP) optical focusing inside scattering media. *Scientific reports* **8**, 2927 (2018).
148 Donnelly, E. F., Price, R. R. & Pickens, D. R. Quantification of the effect of system and object parameters on edge enhancement in phase-contrast radiography. *Medical physics* **30**, 2888-2896 (2003).
149 Donnelly, E. F. & Price, R. R. Quantification of the effect of kVp on edge-enhancement index in phase-contrast radiography. *Medical Physics* **29**, 999-1002 (2002).
150 Caulfield, H. J. & Dolev, S. Why future supercomputing requires optics. *Nature Photon.* **4**, 261-263 (2010).
151 Silva, A. *et al.* Performing mathematical operations with metamaterials. *Science* **343**, 160-163 (2014).
152 Leedumrongwatthanakun, S. *et al.* Programmable linear quantum networks with a multimode fibre. *Nature Photon.* **14**, 139-142 (2020).
153 Zhong, H.-S. *et al.* Quantum computational advantage using photons. *Science* **370**, 1460-1463 (2020).
154 Xu, X. *et al.* 11 TOPS photonic convolutional accelerator for optical neural networks. *Nature* **589**, 44-51 (2021).
155 Feldmann, J. *et al.* Parallel convolutional processing using an integrated photonic tensor core. *Nature* **589**, 52-58 (2021).
156 Shen, Y. *et al.* Deep learning with coherent nanophotonic circuits. *Nature Photon.* **11**, 441 (2017).
157 Lin, X. *et al.* All-optical machine learning using diffractive deep neural networks. *Science* **361**, 1004-1008 (2018).
158 LeCun, Y., Bengio, Y. & Hinton, G. Deep learning. *Nature* **521**, 436-444 (2015).

159 Wei, H. *et al.* Quantum dot-based local field imaging reveals plasmon-based interferometric logic in silver nanowire networks. *Nano Lett.* **11**, 471-475 (2011).
160 Xu, Q. & Lipson, M. All-optical logic based on silicon micro-ring resonators. *Opt. Express* **15**, 924-929 (2007).
161 Zhou, P., Zhang, L., Tian, Y. & Yang, L. 10 GHz electro-optical OR/NOR directed logic device based on silicon micro-ring resonators. *Opt. Lett.* **39**, 1937-1940 (2014).
162 Tian, Y. *et al.* Electro-optic directed XOR logic circuits based on parallel-cascaded micro-ring resonators. *Opt. Express* **23**, 26342-26355 (2015).
163 Yao, C., Kotb, A., Wang, B., Singh, S. C. & Guo, C. All-optical logic gates using dielectric-loaded waveguides with quasi-rhombus metasurfaces. *Opt. Lett.* **45**, 3769-3772 (2020).
164 Sang, Y. *et al.* Broadband Multifunctional Plasmonic Logic Gates. *Adv. Opt. Mater.* **6**, 1701368 (2018).
165 Sadeghi, T., Golmohammadi, S., Farmani, A. & Baghban, H. Improving the performance of nanostructure multifunctional graphene plasmonic logic gates utilizing coupled-mode theory. *Appl. Phys. B* **125**, 189 (2019).
166 Qian, C. *et al.* Performing optical logic operations by a diffractive neural network. *Light: Sci. Appl.* **9**, 59 (2020).
167 Manjappa, M. *et al.* Reconfigurable MEMS Fano metasurfaces with multiple-input–output states for logic operations at terahertz frequencies. *Nature Commun.* **9**, 1-10 (2018).
168 Koirala, M., Sarma, R., Cao, H. & Yamilov, A. Inverse design of perfectly transmitting eigenchannels in scattering media. *Phys. Rev. B* **96**, 054209 (2017).
169 Molesky, S. *et al.* Inverse design in nanophotonics. *Nature Photon.* **12**, 659-670 (2018).
170 Katz, O., Small, E., Bromberg, Y. & Silberberg, Y. Focusing and compression of ultrashort pulses through scattering media. *Nature Photon.* **5**, 372-377 (2011).
171 Katz, O., Small, E., Guan, Y. & Silberberg, Y. Noninvasive nonlinear focusing and imaging through strongly scattering turbid layers. *Optica* **1**, 170-174 (2014).
172 Li, Z. *et al.* Edge enhancement through scattering media enabled by optical wavefront shaping. *Photonics Res.* **8**, 954-962 (2020).
173 Popoff, S., Lerosey, G., Fink, M., Boccara, A. C. & Gigan, S. Image transmission through an opaque material. *Nature Commun.* **1**, 81 (2010).
174 Matthès, M. W., del Hougne, P., de Rosny, J., Lerosey, G. & Popoff, S. M. Optical complex media as universal reconfigurable linear operators. *Optica* **6**, 465-472 (2019).
175 Tao, X., Bodington, D., Reinig, M. & Kubby, J. High-speed scanning interferometric focusing by fast measurement of binary transmission matrix for channel demixing. *Opt. Express* **23**, 14168-14187 (2015).
176 Qu, G. *et al.* Reprogrammable meta-hologram for optical encryption. *Nature Commun.* **11**, 1-5 (2020).
177 Dholakia, K. & Čižmár, T. Shaping the future of manipulation. *Nature Photon.* **5**, 335-342 (2011).
178 Leite, I. T. *et al.* Three-dimensional holographic optical manipulation through a high-numerical-aperture soft-glass multimode fibre. *Nature Photon.* **12**, 33 (2018).
179 Akbulut, D., Huisman, T. J., van Putten, E. G., Vos, W. L. & Mosk, A. P. Focusing light through random photonic media by binary amplitude modulation. *Opt. Express* **19**, 4017-4029 (2011).

180 Goorden, S. A., Bertolotti, J. & Mosk, A. P. Superpixel-based spatial amplitude and phase modulation using a digital micromirror device. *Opt. Express* **22**, 17999-18009 (2014).

181 Xiong, W. *et al.* Complete polarization control in multimode fibers with polarization and mode coupling. *Light Sci Appl* **7**, 54, doi:10.1038/s41377-018-0047-4 (2018).

182 Tzang, O., Caravaca-Aguirre, A. M., Wagner, K. & Piestun, R. Adaptive wavefront shaping for controlling nonlinear multimode interactions in optical fibres. *Nature Photonics* **12**, 368-374, doi:10.1038/s41566-018-0167-7 (2018).

183 Wei, X., Jing, J. C., Shen, Y. & Wang, L. V. Harnessing a multi-dimensional fibre laser using genetic wavefront shaping. *Light: Science & Applications* **9**, 1-10 (2020).